



Journal of Engineering Science & Computing

Vol : 1

Issue : 2

Year : 2019

بِسْمِ اللَّهِ الرَّحْمَنِ الرَّحِيمِ

Paper version

Filed at the King Fahd National Library No. 8742/1439 and the date of
17/09/1439 AH

International serial number of periodicals (ISSN) 1658-7936

Online version

Filed at the King Fahd National Library No. 8742/1439 and
the date of 17/09/1439 AH

International Serial Number of Periodicals (e-ISSN) 1658-7944

the journal's website

<https://journals.iu.edu.sa/JESC/index.html>

The papers are sent in the name of the Editor-in –Chief of the
Journal to this E-mail address

jesc@iu.edu.sa

(The views expressed in the published papers reflect the views of the
researchers only, and do not necessarily reflect the opinion of the journal)

Publication Rules at the Journal^(*)

❖ General rules:

- Report original scientific research (the main results and conclusions must not have been published or submitted elsewhere).
- Fit with the topics of the journal.
- Report novel results, innovative work and show a new scientific contribution.
- Not to bear similarity of more than 25% of a previously published work of the same author(s).
- Follow the rules, regulation and authentic research methodologies.
- Fulfill the required items and the format of the journal provided in appendix below related to the guide for author.
- Opinions expressed in published articles commit the authors themselves only and not necessarily the opinion of the journal.

❖ For all articles:

- The exclusive right to publish and distribute an article, and to grant rights to others, including commercial purposes.
- For open access articles, IU will apply the relevant third-party user license where IU publishes the article on its online platforms.
- The right to provide the article in all forms and media so the article can be used on the latest technology even after publication.
- The authority to enforce the rights in the article, on behalf of an author, against third parties, for example in the case of plagiarism or copyright infringement.

(*) These general rules are explained in details along with other rules for Author's guide in the journal's website: <https://journals.iu.edu.sa/JESC/index.html>

The Editorial Board

Dr. Mohammad A. R. Abdeen

Editor-in-Chief

Associate Professor, Computer Science, Islamic
University of Madinah, Saudi Arabia.

Prof. Shamsuddin Ahmed

Managing Editor

Professor, Industrial Engineering, Islamic
University of Madinah. Saudi Arabia

Prof. M. C.E. Yagoub

Professor, Electrical Engineering, University of
Ottawa, Ottawa, ON, Canada

Prof. Fayez Gebali

Professor, Electrical and Computer Engineering,
University of Victoria, Victoria, B.C., Canada

Prof. Mohammad Qari

Professor, Geology, Islamic University of
Madinah. Saudi Arabia

Prof. Ahmed AlOmary

Professor, Chemistry, Islamic University of
Madinah. Saudi Arabia

Prof. Ibrahim Albedewi

Professor, Computer Science, King Abdel-Aziz
University, Jeddah, Saudi Arabia

Prof. Mohamed Ouzzane

Professor, Mechanical Engineering, Islamic
University of Madinah. Saudi Arabia

Prof. Ahmed B. Al-khodre

Associate Professor, Information Technology,
Islamic University of Madinah. Saudi Arabia

Editorial Secretary: **Asim Mahmoud Amin**

Publishing department: **Omar Hasan Al-abdali**

The Advisory Board

Prof. Hussein T. Mouftah

Professor, Electrical Engineering and Computer
Science, University of Ottawa, Ottawa, ON, Canada
Canada Research Chair in Wireless Sensor Networks
Distinguished University Professor, University of
Ottawa

Prof. Diaan Khalil

Professor, Electrical Engineering, and Vice-Dean, Ain-
Shams University, Cairo, Egypt

Prof. Sultan T. Abu-Orabi Aladwan

Secretary General, Association of Arab Universities,
Amman, Jordan

Professor, Organic Chemistry, USA

Prof. Claus Haetinger

University of Taquari Valley - Univates

Professor, Mathematics, Rio de Janeiro, Brazil

Prof. Kamal Mansour Jambi

Professor, Computer and Information Systems, King
Abdel-Aziz University, Jeddah, Saudi Arabia

Prof. Ameen Farouq Fahmy

Professor of Chemistry, Ain Shams University, Cairo,
Egypt.

Prof. Abdel Ghafoor

Professor, Mechanical Engineering, National
University of Science and Technology, Pakistan

Prof. Mahmoud Abdel-Aty

Dean of Scientific Research and Graduate Studies,
Appl Sci Uni. Bahrain

President of Natural Sciences Publishing, USA
Prof. of Math & Inf Sci at Zewail City of Science and
Technology, Egypt

Vice-President of African Academy of Sciences,
Kenya

(JESC)

The Journal of Engineering, Science and Computing

Issued By

The Islamic University of Almadinah-Almunawarah

Almadinah-Almunawarah, Saudi Arabia

With great pleasure, the editorial board of the Journal of Engineering, Science and Computing (JESC) presents to you the second issue, on-line, the December 2019.

The Islamic University of Madinah launched in 2018, its scientific Journal, JESC, a new international, peer-reviewed, open-access, online and print version of the Journal. It publishes scholarly articles in the areas of Engineering, Sciences, and Computing.

JESC has endured its early stage, and now with the second issue, it has entered its childhood. The JESC is thriving hard to satisfy all the stakeholders of the Journal, locally and internationally.

The JESC's core purpose is scientific communication in the disciplines of science engineering and computing. It is served by contributing authors, invaluable anonymous reviewers, and the international editorial board. The JESC is satisfied with the impartiality, rigor, and timeliness of its review process. The journal follows a blind and peer-reviewed process at least by two experts from the discipline.

This issue attracted quite a significant number of articles and due to limitations of space, only seven articles are accommodated, namely four in engineering, one in computing and two in the discipline of science.

We invite you to browse through the articles in the second issue of the JESC and request you to submit your research outcome in the forthcoming issue of the JESC.

Mohammad Abdeen, Ph.D., P.Eng.

Editor-in-Chief

The Journal of Engineering, Science and Computing
(JESC)

A handwritten signature in black ink, appearing to read 'M. Abdeen', with a long horizontal flourish extending to the right.

Table of Content

Article 1.	
A Topic-based Forensic Analysis and Visualization of an Email network: Application to the Enron Dataset	1
Article 2.	
A Hybrid Particle Swarm Optimization and Simulate Annealing (PSO-SA) Algorithm for Scheduling a Flowshop Manufacturing cell with Sequence Dependent Setup Times.....	23
Article 3.	
A Comprehensive Review on NO _x & DPM Diesel Engine Emissions and Its Control Techniques	43
Article 4.	
Modified Compact Central Finite Difference Schemes For The Simulations Of Wave Equation At Any Wave Number.....	67
Article 5.	
A Theoretical Analysis of Air Cooling System Using Thermal Ejector Adapted to Operation Conditions for Control Strategy	86
Article 6.	
Freundlich Isotherm Model of Adsorption of Fe ²⁺ , Co ²⁺ and Cr ³⁺ Ions from Aqueous Solution Using Activated Carbon Prepared from Corn Maize (<i>Zea mays .ssp</i>) Waste.....	108
Article 7.	
Fundamentals to Detect Tensor Product Bézier Patches in Euclidean 3-Space.....	129

A Topic-based Forensic Analysis and Visualization of an Email network: Application to the Enron Dataset

Casey Kalinowski

University of Lynchburg, VA, USA

Kalinowski_c@lynchburg.edu

M. Zakaria KURDI

University of Lynchburg, VA, USA

kurdi_m@lynchburg.edu

Abstract

This work is about visualizing an email network with graphs. This visualization is based on the email's topics. So, the first part of this work is about exploring three rule-based methods and an unsupervised method of topic detection applied to a large dataset. Keyword or Term Frequency (TF) method is used as a baseline for comparison. Latent Dirichlet Allocation (LDA) combined with WordNet as well as two versions of conceptual topic detection, both involving a version of keyword extraction combined with WordNet, are also compared. Our results show that LDA combined with wordnet has the highest precision but a comparable F-measure to the conceptual approaches. Through a series of examples, we then demonstrate how annotating the emails with topics is a good way to shed light on the underlying professional and social relationships within the email network, which can provide substantial help within application contexts such as forensic investigations. This annotation is also showed to help in providing quantitative feedback about the performance of the topic detection algorithms.

Keywords

topic modeling, Social Network Analysis (SNA), Social Network Visualization, Term Frequency (TF), Latent Dirichlet Allocation (LDA).

التحليل الشرعي المرتكز على الموضوع والتصور لشبكة البريد الإلكتروني: التطبيق على مجموعة بيانات Enrom

هذا العمل يدور حول تصور شبكة البريد الإلكتروني مع الرسوم البيانية. يعتمد هذا التصور على موضوعات البريد الإلكتروني. الجزء الأول من هذا العمل يدور حول استكشاف ثلاث طرق تستند إلى قواعد وغير خاضعة للرقابة للكشف عن الموضوع يتم تطبيقها على مجموعة بيانات كبيرة. يتم استخدام طريقة تردد الكلمة أو المصطلح (TF) كخط أساسي للمقارنة. يتم النظر أيضاً في مقارنة تخصيص Latent Dirichlet Allocation (LDA) مع WordNet بالإضافة إلى إصدارين من اكتشاف الموضوع المفاهيمي، وكلاهما يتضمن إصداراً من استخراج الكلمة الأساسية المدججة مع WordNet وتعتبر أيضاً بالمقارنة. تظهر نتائجنا أن LDA مدججة مع wordnet لديها أعلى دقة ولكن مقياس F قابل للمقارنة للنهج المفاهيمية. من خلال سلسلة من الأمثلة، نوضح بعد ذلك كيف يكون التعليق على رسائل البريد الإلكتروني مع الموضوعات وسيلة جيدة لتسليط الضوء على العلاقات المهنية والاجتماعية الأساسية الكامنة داخل شبكة البريد الإلكتروني، والتي يمكن أن توفر مساعدة جوهرية في سياقات التطبيق مثل التحقيقات الجنائية. يتم عرض هذا التعليق التوضيحي أيضاً للمساعدة في توفير ملاحظات كمية حول مدى أداء خوارزميات اكتشاف الموضوع.

1. Introduction

Different approaches were proposed in the literature to identify communities or groups of users within social networks. These approaches rely mostly on the connectivity of the users, which are represented as edges within a graph. The purpose of this research is to develop a program that will analyze the Enron email dataset to find patterns of networking between the employees of the Enron Corporation involved in the fraudulent acts of the company leading up to the 2001 bankruptcy. More specifically, it is designed to help identify and rank the actors involved in a given process such as accounting, stocks, IT, and management. Although it is possible to find some information from the organization's documents or employees about who is involved in a given process, it is hard to trust this information as some people hesitate to provide the real information during a criminal investigation. The second goal of this work is to group the actors involved in a process and understand the nature of their relationship that can be strictly professional or sometimes personal.

The approach proposed here consists of annotating the emails of a large dataset set using different approaches. The main technical challenge with the task of topic detection consists of the large size of the data that cannot be annotated by hand to train a supervised machine learning algorithm.

Several previous works in the literature viewed the relationships between the members of a social network from a quantitative angle [1], [2], [3]. For example, if two persons exchange 100 emails, 100 would be the weight of the connection between these two persons. However, this weight does not give any idea about the nature of the relation between the involved persons. In this paper, these relations are viewed from a qualitative angle, where the topic or subject of the connection is considered. Combined with the frequency that can help build a weighted graph that shed light on the true relationships within an organization. For example, if two persons exchanged 100 emails out of which 56 are about accounting and 44 are about IT that gives a much better idea about the nature of these persons. In many contexts, such as criminal investigation, learning about the actual hierarchy of actors involved in a process such as accounting or management can be hard to find.

The work presented in this paper contributes in two main areas. First, it proposes an approach based on the integration of keywords with two methods based on conceptual information from WordNet as well as an LDA combined with wordNet. After a comparison of these methods with a simple Term Frequency (TF) approach, it demonstrates how topic detection of emails can greatly

reduce the time of criminal investigations, where a large dataset must be searched. This is done by effectively visualizing the data using a topic graph that gives a precise idea about the interactions between the involved persons within the network.

This paper is showing how topic graphs can be used on real data collected from a real criminal investigation. It is also significant in that the technique can be applied to other social networks besides email, thus making it very useful in many application fields.

2. Topic Detection and Modelling

Topic modeling is based on three fundamental assumptions. First, every document has its internal (latent) topical structure. Second, this structure can be inferred from the document algorithmically based on the vocabulary used in each document. More formally, a collection of documents $D=\{d_1, d_2, \dots, d_n\}$ may cover a set of topics $T=\{t_1, t_2, \dots, t_m\}$. In a normally constituted data, we usually have $m < n$. Third, since words are the main indicators of topics, it is easy to imagine a mapping between topics and words such that $t_i=\{w_1, w_2, \dots, w_k\}$. Topic detection in document d consists of algorithmically assigning a set of one or more topics (T_d) to every document using a function such that $F(D) \rightarrow T_d$ where $T_d \subseteq T$.

Information Retrieval (IR) and topic identification are tightly related. Given the size of the documents collection to deal with in IR, unsupervised techniques such as document clustering were used since the early stages of this field's investigation [4]. In such approaches, documents dealing with similar topics are supposed to fall within the same cluster. For example, [5] used Self Organizing Maps (SOM), while [6] used a combination of Latent Semantic Analysis (LSA) and K-means. A major disadvantage with clustering is that the machine-built clusters are not easy to interpret by human users, which limits the application of these techniques. Many works have used LDA for identifying the topics at the level of sentences in written texts [7]. Later many other applications to topic identification started to emerge like opinion mining [8], text summarization [9], analysis of open-ended survey questions [10] and machine translation [11].

3. Social Network Analysis (SNA) and Link Mining (LM)

Social networks are becoming a central part of modern society. Therefore, it is essential for a wide number of applications to extract information from these networks effectively. Link Mining (LM)

is concerned about exploring social networks from the angle of the relationship patterns between the entities. Hence, LM focuses on discovering explicit links between the social network's entities represented as a graph [12]. So, for each user of the social network (in our case the email set), the connections of this user are analyzed usually from two angles: volumetric and temporal. Volumetric concerns the number of emails sent or received by a given user. The temporal analysis concerns the response time of such interaction, which is about the time lapse between sending an email to an email address and getting the response to the same email address. These analyses are used to calculate different statistical scores that can help rank and group users. Such links usually exhibit patterns of relationships. Several key indicators were proposed in the literature such as the degree of centrality of a node, clustering coefficient, betweenness centrality, and the social score [1], [2]. Graphs are a natural tool to visualize social media, as it is easy to represent a person or an entity as a node and a connection as an edge.

Unlike previous works, the relations will not be explored here from a binary point of view (there is a relation or not). Rather, they will be explored from a continuous topical point of view, where the nature of the relationship between the involved entities is taken into consideration.

4. The Enron emails set

The Enron email set is a large dataset that is publicly available. It was obtained by the Federal Energy Regulatory Commission during its investigation of Enron's scandal. It is made of about 500.000 emails (1.32 GB of raw data) from 158 users, exchanged by the Enron's corporation employees during the period of 1998-2002. Given its importance, this corpus has been explored by a wide number of works from disciplines such as SNA, text mining and authorship attribution [13], [1], [14], [15]. This corpus is the right dataset for this study for different reasons. First, it is a realistic dataset about a real forensic investigation case. Second, this dataset is large enough and comes from a representative number of adult users from different age ranges and genders (almost half of the emails are written by males).

An analysis of the email lengths shows that shorter emails are more frequent than longer ones (figure 1). The lengths of about 44% of the emails are within the range 1-30 and the lengths of about 60% of the emails are within the range 1-50. On the other hand, only about 24% of the emails are within the range 100+. These numbers are coherent with the fact that email exchanges within a professional context such as Enron are usually concise. Hence, given this variation in lengths, a

good method for topic classification should be able to process texts with different lengths ranges and to be especially good with short texts.

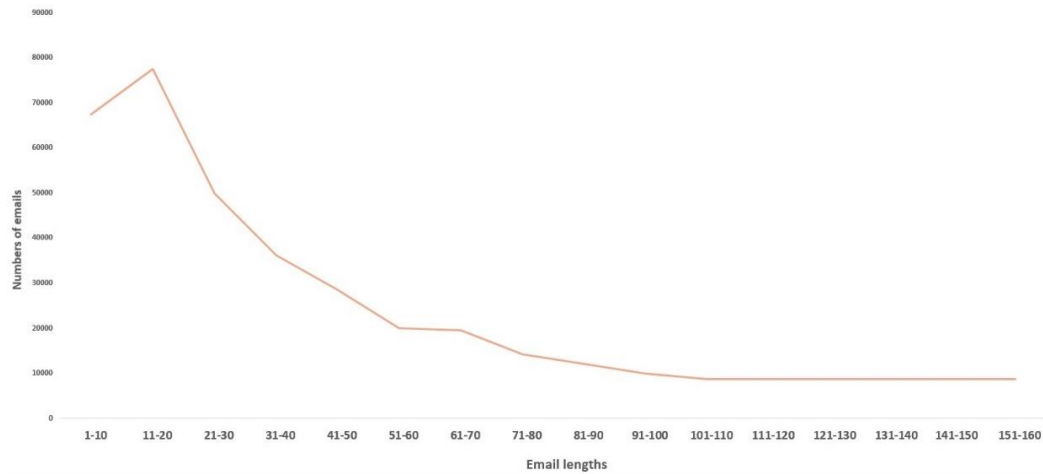


Figure 1. Number of emails by length range within the Enron corpus

The emails are pre-processed as follows. Since the emails contain information in various formats, all emails are reformatted into one uniform JSON file. All the history of previous emails is removed. The removal of everything but the latest response helps reduce the noise related to previous emails from the same exchange. Also, the subject and the author of the email are not used. The body of the emails is cleaned from any non-ASCII characters.

To evaluate the system, the authors with the help of two CS students manually annotated a set of 1999 emails. A schema of eight topics was proposed: meeting, management, IT, leisure, stock, accounting, law, and miscellaneous. The corpus was annotated by four different annotators using the same program that was written specifically for this task.

5. Experimental setup

The data is analyzed in four different approaches and then compared to measure their effectiveness and processing runtime. The first approach is a simple keyword search, which will serve as the basis for comparison for the other three methods. The second and third approaches utilize NLTK's WordNet in a modified and more complex versions of the keyword search, while the fourth version uses a hybrid of LDA and WordNet.

WordNet is a thesaurus-like and psycholinguistically motivated lexical database that was developed at Princeton University [16], [17] (see [18] for an introduction). Within this database,

the synset is the smallest unit and represents a meaning of a word (possibly among others). In addition to a word's explanation and usage examples, WordNet also covers semantic relations such as synonyms, antonyms, hyponyms (a word that has a more specific meaning than another. For example, *lion* is a hyponym of *animal*) and hypernyms (*animal* is the hypernym of *lion*). In the three approaches proposed here, WordNet plays a key role in the mapping between the words, that are too specific, and the concepts that are generic by nature and can be expressed by multiple words.

5.1 Term Frequency (TF)

Words and concepts are tightly interrelated. Hence, it is possible to use keywords as an indication of a topic in a text. This method is usually referred to as Term Frequency (TF) and it was one of the first used methods in Information retrieval [19]. It consists of finding the most frequent word(s) in a document and mapping it into the list of topics. It is widely used in text processing software for keyword search. This method has well-known limitations in the literature [20]. However, given its simplicity and popularity, it is used here as a baseline for our comparison. Some examples of mappings between topics and keywords are provided in table 1.

Table 1. Example of keywords mapping into topics

Topic	Keywords
Management	Management, Guidance, Supervision
Accounting	Accounting, Finances, Balance of Payment
Meeting	Meeting, Board Meeting, Conference, Convention
Stock	Stock, Shares, Growth Stock
Leisure	Leisure, Free Time, Vacation
Legal	Law, Tax Law
Other	No keywords

5.2 Concept based search

The main limitation of keyword-based information retrieval is that only the texts that contain words that match the searched keyword will return positive results. There is a great potential to improperly assign a topic or fail to assign one altogether. To go beyond simple pattern matching, semantic relationships can help widen the spectrum of relevant words found in the text. Hence, a generalization of the extracted keywords is carried out with a list of the keyword hyponyms that is obtained from WordNet.

The searched concepts are defined in two ways. First, the **semi-automatic synset** selection consists of getting every synset for every keyword using WordNet. Then, using WordNet again, every synset for every direct hyponym of each of the original synsets is found and mapped to the keyword. The intention of creating such a large list of synsets is that the increased range of words increases the chances of properly assigning a topic. The second approach, the **manual synset selection**, is a stripped-down version of the first. One specific synset is chosen for each topic and then WordNet is used to make a list of all the direct hyponyms for those specific synsets of the topic keywords. In both versions, when needed, additional synsets can be added by hand to enrich the concept. For example, the topic “accounting” can have the synsets “transaction.n.01” and “value.n.02” added onto the hyponym list in addition to the ones WordNet automatically added. Both of these methods provide us with the final list of target synsets to search in the text.

After defining the searched concepts, the search is carried out as a binary decision process. For every searched concept, the program decides if the text is relevant for this concept or not. WordNet is again used to match the word against a defined concept. The program will read each email once for every topic keyword. As each word in the email is read by the program, the same WordNet function as before is called to find each synset associated with that word. Since the program cannot determine the context of the current word being analyzed, all the synsets of that word are used to match against the current target keyword synset (table 2). It then compares each of those new synsets of the current word in the email to each of the synsets in the current topic’s synset list using WordNet’s *path_similarity()* function.

Table 2. Example of how each word in the email has all senses of the word analysed against each topic synset

Current word in email	Current topic being scored
Transaction	Management
Associated Synsets	Current Synset being scored
“expedition.n.01”, “expedition.n.02”, “expedition.n.03”, “excursion.n.01”, “dispatch.n.03”	“administration.n.01”

The function returns a score based on how similar a synset is to another synset. If the resulting score is higher than .35, the program assigns that word in the email a point. To prevent topics with larger synset lists from getting more points than those topics with fewer hyponyms, no more than

one point can be assigned per word. After all the words in the email have been compared to all the topic's synsets, the score is added up and divided by the total number of synsets in the email to give the weighted average for that topic. The process then repeats for the rest of the target topics. Since we have decided that an email can have multiple topics assigned to it, a minimum threshold was created to prevent the program from assigning too many topics to an email. The weighted average score for a topic must be greater than or equal to 0.01 to be assigned as the topic to that particular email (see table 3 for an example). Any email where all the topics fail to meet that minimum threshold are assigned the topic of "Other."

Table 3. Example of mapping between the keywords extracted from an email and topics

Email	Topic scores	Chosen Topics
Rick, Attached is the spreadsheet that contains the capital deployed as of June 2001. Let me know if you need anything else. Thanks, Rob Rob Brown Manager, Enron Corp. Financial Accounting Reporting Off. 713.853.9702 Cell 713.303.4497	{'meeting': 0.0, 'accounting': 0.014084507042253521, 'management': 0.0, 'stock': 0.001006036217303823, 'leisure': 0.0, 'IT': 0.0, 'law': 0.0}	Accounting

5.3 LDA

Presented for the first time in [21], Latent Dirichlet Allocation (LDA) is one of the most popular methods for unsupervised topic detection. Based on the Bag of Words approach, LDA is a generative model that builds on the following intuitive idea: every document is made of a mixture of topics and every topic has a distribution of words that is associated with it. The plate notation of the LDA model is provided in figure 2.

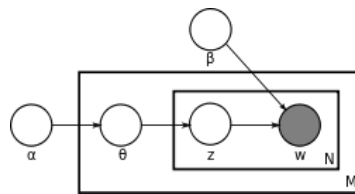


Figure 2. Plate notation for the LDA model

Where:

- α is a Dirichlet prior that represents the topic distributions per-document. A high value for α indicates that each document is likely to contain multiple topics.
- β is a Dirichlet prior that represents the word distribution per-topic. A high beta indicates that each topic will be made of many words.

- θ_i represents the topic distribution for document i . One can think of this parameter as document-topic matrix.
- ϕ_k represents the word distribution for topic k . It consists of rows defined by topics and columns defined by words.
- z_{ij} represents the topic for the j -th word in document i
- w_{ij} represents a specific word j in document i .
- M is the total number of documents within the corpus.
- N number of words in a document.

The Gensim library was used to build the LDA model. To make LDA more effective, the vocabulary dictionary of the model is made up of every noun and plural noun that appears in the email messages except for stopwords. The NLTK built-in Part-of-Speech Tagger was used to identify the nouns. To increase the speed of the program, a list of stopwords is created using NLTK's default stopwords. Each email, being used to create the vocabulary dictionary, passes through a Regular Expression to check validity. Words, that do not match the regular expression and thus are not real words, are added to the stopwords list. As the stopwords list grows, the program speeds up because it knows which words it does not have to pass through to the NLTK POS tagger. A training set of emails is then fed to train the LDA model and produce a set of topics. Each topic produced by the LDA model is a list of keywords. Therefore, the raw topics are not usable for this type of analysis in their current state. Hence, alterations must be made before they can be used in the topical analysis module. The top keyword from each topic list is added to the new topic set. A simple check is done to avoid topic keyword repetition in the new set (see figure 3 for an example of the above steps). The final step in preparing the LDA topics for the analysis is the transformation of the topics into WordNet readable synsets. To do this, every hyponym of every synset of the keyword set is found from WordNet. Because the synsets are being chosen for every sense of the word, the resulting dictionary of synsets is significantly larger than that of the WordNet version where a specific synset is chosen for each topic.

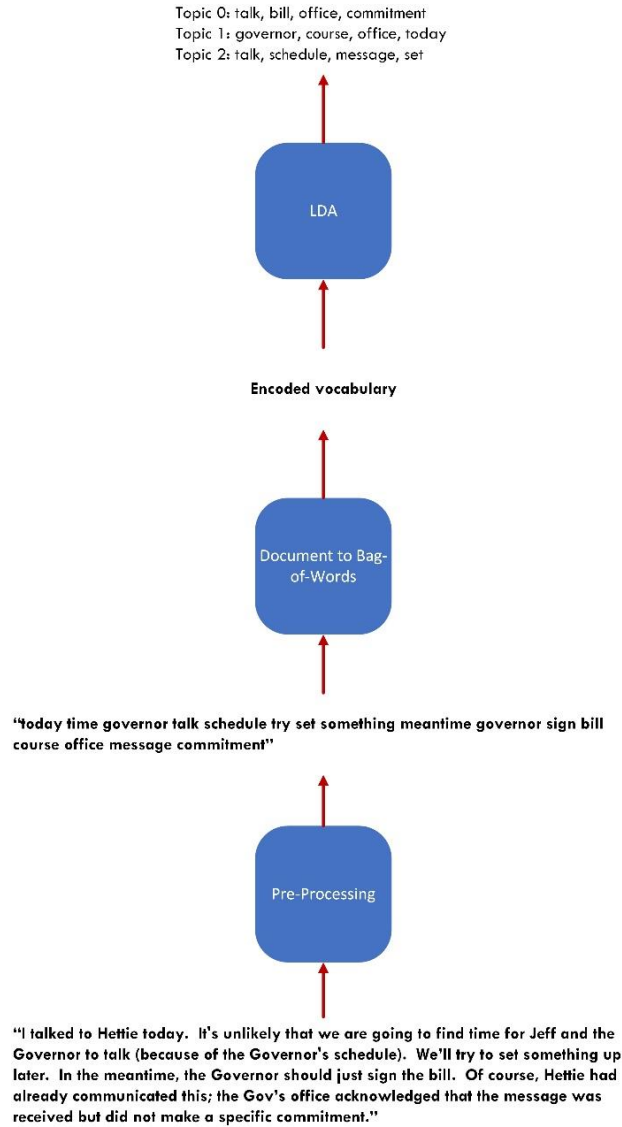


Figure 3. Example of an email topic detection with LDA

6. Evaluation and Results

Given the size of the Enron dataset, it is essential to do performance analysis in terms of processing time. A runtime comparison is depicted in figure 4.

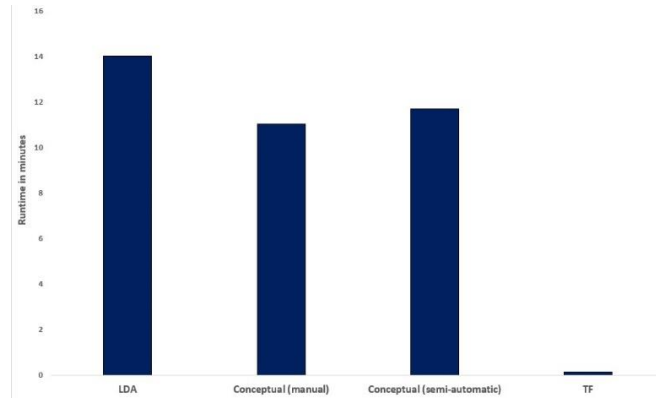


Figure 4. Runtime comparison of the four approaches to complete the topical analysis of the 1999 test emails (in minutes)

As seen in figure 4, the runtime is proportional to the complexity of the method. So, TF is the fastest method given the simplicity of processing, as it analyzed the 1999 test emails with a runtime of 8.88 seconds. On the other hand, LDA, being the most computationally complex approach, requires more time than the three other methods (about 14 minutes). Finally, the difference between the two conceptual methods on the one hand and the LDA approach is not substantial, with the manual synset selection method taking 11 minutes and the semi-automatic synset selection method taking 11 minutes and 45 seconds.

In addition to the runtime, it is important to compare the performance of the adopted approaches. For the testing of the accuracy of the topical analysis, a separate program was created that compared the topics of the 1999 hand-annotated emails to the same 1999 emails that have been run through the different discussed topical analysis programs. The evaluation was performed using the following three following metrics: recall, precision, and F-measure. Since we are dealing with a multiple topic setup, these metrics were calculated based on [22]. Figure 5 depicts the performance of the four adopted measures.

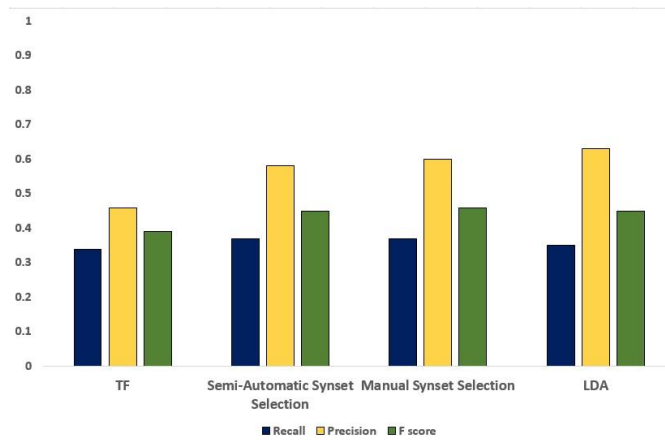
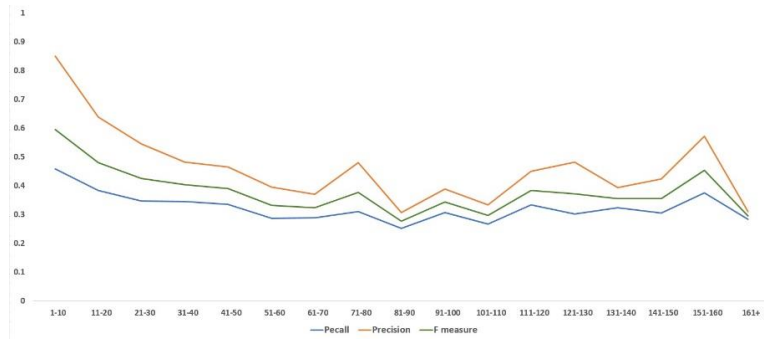


Figure 5. Accuracy Comparison of the Topical Analysis Programs using the 1999 part of the data set that was annotated by hand

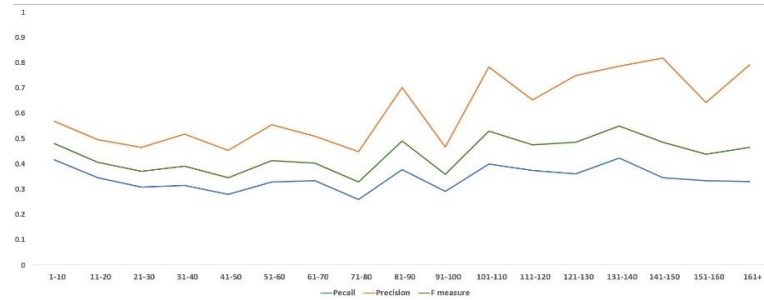
The accuracy of the TF method is the lowest in the three considered measures, with the recall being 0.34, precision being 0.46, and F-score being 0.39. The two conceptual approaches have comparable F-score (0.45 for the semi-automatic and 0.46 for the manual), this score is driven by the small difference in terms of precision (0.58 for the semi-automatic and 0.60 for the manual). LDA has comparable F-score to the conceptual approaches 0.45. However, its recall is slightly lower (0.35), while its precision is slightly higher (0.63).

As we have seen in section 4, there is an important variation in email lengths within the Enron corpus. Therefore, it is important to study how the four different approaches are sensitive to the variation in the texts' lengths. To account for that, we depicted the three adopted measures of performance for every approach by a varying length of the texts (figure 6). The lengths are measured by the number of words. We adopted the word as a measure of length as the lexicon is the basis of topic classification within our four approaches. We also used sixteen gradual length ranges by 10 words, between 1 and 160, as these ranges seem to reflect the variations of lengths as discussed in section 4.

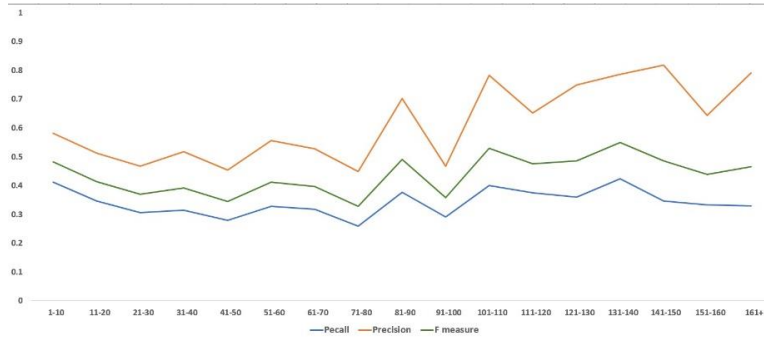
TF



Semi-automatic synset selection



Manual synset selection



LDA

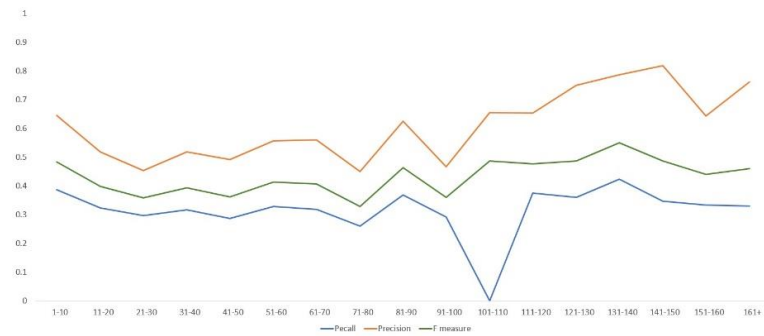


Figure 6. Accuracy Comparison of the Topical Analysis Programs by email lengths using the 1999 part of the data set that was annotated by hand

7. Discussion of the results of topic detection

The results depicted in figure 5 are coherent with our initial expectations. TF has the lowest F-score. This score is driven by a low recall, which is justified by the limited capacity of generalization of the keyword search. This is because TF has a great potential of a mismatch of the topic. The generalization brought by WordNet usage by the three other methods is rewarded by a higher recall, especially with the conceptual methods. On the other hand, the complex processing of LDA gives the highest precision of all the approaches. A final observation about all the approaches, it is easy to see that recall is lower than precision. This suggests that the mapping between the keyword part of all the adopted methods is problematic, as it is hard to build a robust representation of the topics. However, this incomplete representation of the topics is better at building the boundaries between the topics.

The results by email lengths show different patterns. For the keyword-based approach (TF), the tendency is clear: the more words we have, the lower the performance. This is because the increase in size means an increase in the number of candidate keywords. Consequently, within the range 1-10, TF has the highest performance. This can explain the poor overall performance of this approach. On the other hand, the three other approaches seem to better resist the variation in length. Finally, except for TF, precision seems to be more prone to variation with the length increase than recall. Since precision is about adding a new class that is incorrect (e.g. saying that an email about management is also about leisure), the risk of incorrectly adding a new class increases with the increase of the number of words.

8. Visualization of the graph of topics

Following the topical analysis of the emails by the four different approaches comes the creation of the network graphs. This is done with the library NetworkX in Python. In addition to helping draw the graph, this open-source library provides functions for standard graph algorithms as well as different measures of centrality used in SNA. The program goes through every email and gets the “to address” and the “from address” of the email. These will be used to create the nodes and edges of the graph. As the program reads through the emails, it adds weight to the edges between the nodes. If there is no existing node for the “from address” it will create one. It will do the same for the “to address”, but with this one condition changed: if there are multiple recipients of the email, it will check for an existing node for all the “to addresses” and create new ones if necessary. This

allows for the creation of nodes for every recipient of the email. Once the nodes are created, an edge is generated between the sending node and all the recipient nodes with a starting weight of one. NetworkX can detect if an edge already exists, so if there is already an edge, the weight of that edge is increased by one. In addition to keeping track of the weight of each edge, NetworkX can keep track of custom attributes. Using this feature, the weight of each topic is saved to the edge in addition to the edge weight. For example, an edge between two nodes could have the following attributes: 'weight:45, meeting:6, accounting:2, management:7, stock:0, leisure:5, IT:0, law:0, other:25'. These added attributes allow for creating graphs based on different topics. The data visualization tool used to create the examples in this paper is the open-source software Gephi. To give an idea about the usefulness of the topical annotations of the connections, let's first start with a simple example. Suppose we have the following situation: a and b exchanged 100 emails out of which 25 are about accounting. Let's suppose as well that a and c exchanged 60 emails, out of which 40 are about accounting. If we take the absolute numbers, b is more connected with a than c . However, if we are interested in emails about accounting then c is more connected with a .



Figure 7 A general graph and a topic graph

As we can see in figure 7, the topic graph shows some underlying patterns in the social graph that cannot be seen by observing the general graph.

To give examples of a larger scale, let's start with the graph depicting all the connections within the Enron dataset, presented in figure 8.

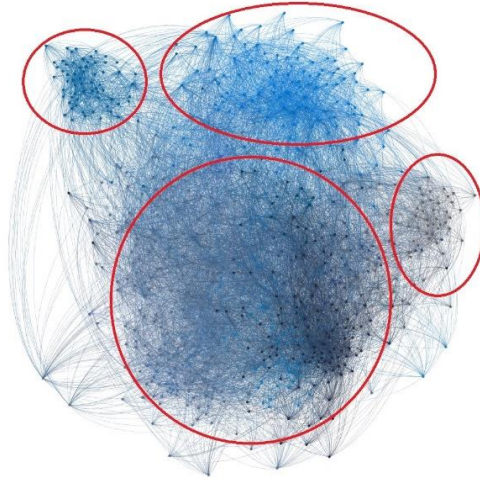


Figure 8 Graph depicting all the unlabeled connection of the Enron dataset

As we can see in figure 8, this graph just gives a very general idea about the connections within the network. One can see there are some clusters (surrounded by red circles) of different sizes. At this level of generality, it is hard to tell if these clusters are about groups of people of similar interests or what is exactly the nature of the interactions within each of these clusters.

If we use the 1999 portion of the dataset. The top 500 nodes (by degree) are provided in figure 9A, along with the top 500 nodes (by degree) with all the nodes of Enron employees that were found guilty highlighted in red that are provided in figure 9B. Despite the reduction of the number of emails, the produced graphs are not very useful as they still give a very general overview of the interaction patterns within the network.

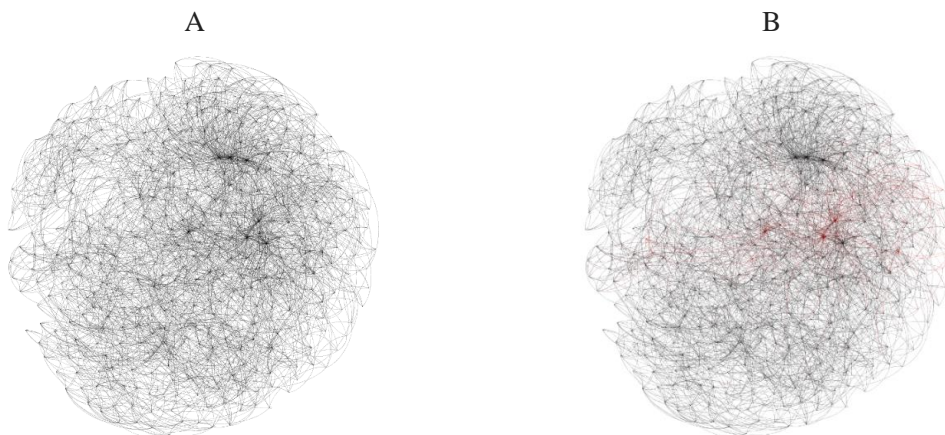


Figure 9 (A) Top 500 nodes without topic – (B) Top 500 nodes without a topic, with the nodes of Enron employees that were found guilty highlighted in red

Another example is provided in figure 10. It is about the top 21 nodes (by degree). This graph showcases how one can find the biggest contributors to a social network. Some of the larger nodes are encoded as follows: A: Jeffrey Skilling, B: Kenneth Lay second email address, C: Jeff Dasovich, D: Tim Belden, and E: Kenneth Lay's primary email address. A surface-level look at this network graph shows that not only do Jeff Dasovich and Tim Belden communicate with a lot of people, they also communicate with each other much more than anyone else. In this example, one might also be interested in who the unlabeled node is that communicates with Kenneth Lay's primary email address. Further investigation reveals that it is his secretary, Rosalee Fleming.

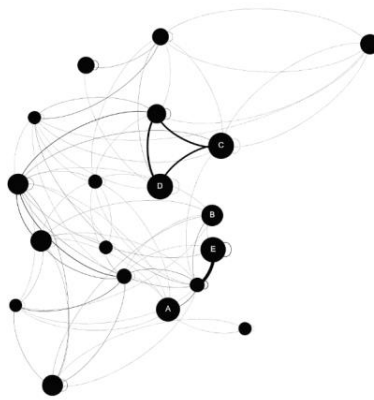


Figure 10. Top 21 nodes with all topics from the full corpus

With the classic method, we can have a more precise view by selecting the weight range (e.g. the most or least connected range). However, despite its precision, this graph does not give any information about the nature of the interactions between the nodes.

In figure 11, we have the employees with the highest count of unique email recipients with the topic of *law* as analyzed with the manual synset selection method. This is an example of how one could analyze a graph to see who talks to most people about a certain topic. In addition to that, we can see who they talk to the most by seeing the larger edges.

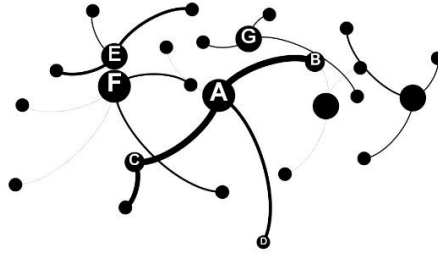


Figure 11. Topic Law from the entire corpus, with A - michelle.akers@enron.com, B - phillip.allen@enron.com, C - eric.bass@enron.com, D - anne.bike@enron.com, E - kayla.harmon@enron.com, F - jeff.dasovich@enron.com, and G - araceli.romero@enron.com

In addition to being useful for understanding the social and professional relations underlying the network, graph visualization is useful for evaluating the performance of the adopted topic detection algorithms. To do so, we generated the meeting of the *meeting* topic using the 1999 human-annotated emails as well as the equivalent graphs generated by three topic detection methods as an example (figure 12). To make the comparison easier, we selected specific nodes that seem important on the human graph and highlighted them in other graphs. The red node represents the user Steven Harris. The red node is present in all the graphs, but we can see that it is much less important in the semi-automatic and keyword search methods than it is in the human method and the manual synset method. Furthermore, the blue node represents Mike Grigsby. This node, which is prominent in the human graph, is only present in the manual synset graph. The yellow node that represents Mitch Robinson is found in only the human graph, meaning that all the other methods failed to categorize any of their emails with the topic "meeting". The orange node is based on what is most prominent in the manual synset method. As we can see, the orange node is also found in the human graph and the semi-auto graph, but not in the keyword search graph. It is interesting to note that what seems central in the WordNet methods is much less prominent in the human graph.

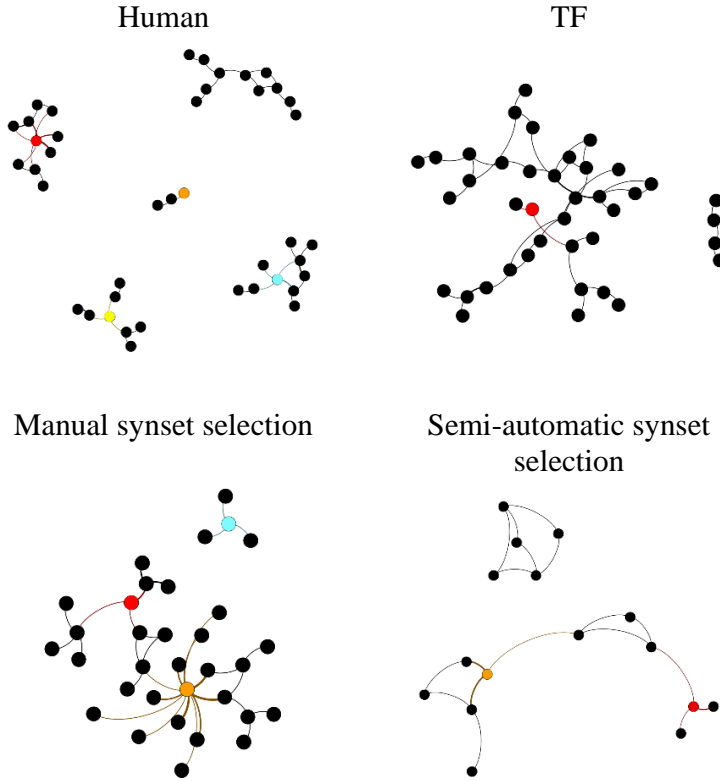


Figure 12. Comparison of partial graphs generated with three topic detection methods with the graph based on the human labeled data

9. Conclusions

This paper is about visualizing social networks with graph topics. It is made of two main parts. In the first part, we compared four different approaches to topic detection using the Enron dataset. The results showed that LDA outperformed the three other approaches especially in terms of precision. In the second part of the work, we demonstrated how topic graphs can shed light, not only on the quantitative aspects of the relations between the users but also on the nature of these relations through the topics. We also showed that the graph generation method can also bring interesting information about the qualitative performance evaluation of the topic labeling methods. Several perspectives of this work are being explored. First, a larger scale comparison of different rule-based and unsupervised machine learning approaches is being carried. In addition, a deeper exploration of the role topics within the graph is also being conducted. Finally, the application of

the concepts presented in this paper is being considered to other types of social networks like Twitter and Facebook.

10. References

- [1] J. Diesner and K. Carley, “Exploration of communication networks from the Enron email corpus”, In Proceedings of Workshop on Link Analysis, Counterterrorism and Security, Newport Beach CA, 2005.
- [2] J. Diesner, T. L. Frantz, and K. M. Carley. “Communication networks from the Enron email corpus”. *Journal of Computational and Mathematical Organization Theory*, 11:201–228, 2005.
- [3] Ryan Rowe, German Creamer, “Automated Social Hierarchy Detection through Email Network Analysis”, Joint 9th WEBKDD and 1st SNAKDD Workshop’07 August 12, San Jose, California, USA, 2007.
- [4] Gerard Salton, ed., *The SMART Retrieval System*. Englewood Cliffs, N.J. Prentice Hall, 1971.
- [5] Everitt B.S., Landau S., Leese M., Stahl D., *Cluster Analysis*, 5th Edition, Wiley, 2010.
- [6] Halabi Ammar, Ahmed-Derar Islim, Mohamed-Zakaria Kurdi, A hybrid approach for indexing and retrieval of archaeological textual information, *International Conference on Knowledge-Based and Intelligent Information and Engineering Systems*, /9/8, pp 527-535, 2010.
- [7] Shafiq Joty, Giuseppe Carenini, Gabriel Murray, and Raymond Ng, Finding Topics in Emails: Is LDA enough? 2009 <https://raihanjoty.github.io/papers/joty-carenni-ng-lda-nips-09>.
- [8] Veselin Stoyanovand, Claire Cardie, Topic Identification for Fine-Grained Opinion Analysis, *Proceedings of the 22nd International Conference on Computational Linguistics (Coling 2008)*, pages 817–824 Manchester, August 2008.
- [9] Chin-Yew Linand, Eduard Hovy, The Automated Acquisition of Topic Signatures for Text Summarization, *COLING '00 Proceedings of the 18th conference on Computational linguistics - Volume 1* Pages 495-501, Saarbrücken, Germany — July 31 - August 04, 2000.
- [10] W. Holmes Finch Maria E. Hernández Finch Constance E. McIntosh Claire Braun, “The use of Topic Modeling to Analyze Open-Ended Survey Items”, *OpenMx XSEM with Applications to Dynamical Systems Analysis*, May 22, 2017.
- [11] Jinsong Su, Deyi Xiong, Yang Liu, Xianpei Han, Hongyu Lin, Junfeng Yao, Min Zhang, A Context-Aware Topic Model for Statistical Machine Translation, *Proceedings of the 53rd Annual Meeting of the Association for Computational Linguistics and the 7th*

- International Joint Conference on Natural Language Processing, pages 229–238, Beijing, China, July 26-31, 2015.
- [12] Lise Getoor, Christopher P. Diehl, LinkMining: A Survey, SIGKDD Explorations, 7(2), pp 3-12, 2005.
- [13] Man Wang, Minghu Jiang, Text categorization of Enron email corpus based on information bottleneck and maximal entropy, ICSP2010 Proceedings, 2010.
- [14] A. McCallum, X. Wang, A Corrada-Emmanuel, Topic and role discovery in social networks with experiments on Enron and academic email, Journal of Artificial Intelligence Research, Volume 30 Issue 1, September Pages 249-272, 2007 .
- [15] M. Zakaria KURDI, Content-dependent vs. content-independent features for gender and age range identification in different types of texts, International Florida Artificial Intelligence Society FLAIRS-33, May 19-22, 2019, Sarasota Florida.
- [16] George A. Miller, WordNet: A Lexical Database for English. Communications of the ACM Vol. 38, No. 11: 39-41, 1995.
- [17] Christiane Fellbaum, WordNet: An Electronic Lexical Database. Cambridge, MA: MIT Press, 1998.
- [18] M. Zakaria KURDI, Natural Language Processing and Computational Linguistics 2: Semantics, Discourse and Applications, London, ISTE-Wiley. ISBN: 978-1-848-21921-2, 2017.
- [19] Gerard Salton, and Michael J. McGill, Introduction to Modern Information Retrieval, New York, McGraw-Hill Book Company, ISBN 0-07-054484-0, 1983.
- [20] Furnas, G. W., T. K. Landauer, L. M. Gomez, and S. T. Dumais, “The vocabulary problem in human-system communications”, Communications of the ACM 30(11), 964-971, 1987.
- [21] David Blei, Andrew Ng, Michael Jordan, and John Lafferty, (ed.). "Latent Dirichlet Allocation". Journal of Machine Learning Research. 3 (4–5): pp. 993-1022, 2003.
- [22] Marina Sokolova, Guy Lapalme, A systematic analysis of performance measures for classification tasks, Information Processing and Management 45, pp 427–437, 2009.

A Hybrid Particle Swarm Optimization and Simulate Annealing (PSO-SA) Algorithm for Scheduling a Flowshop Manufacturing cell with Sequence Dependent Setup Times

Al-Mehdi M. Ibrahim,

College of Engineering, University of Gharayn, Libya

Email: umalmehd@myumanitoba.ca

Tarek Elmekkawy

College of Engineering, Qatar University, Qatar

Email:tmekkawy@qu.edu.qa

and

Hussein Elmehdi

College of Sciences, University of Sharjah, AUE

Email:hmelmehdi@sharjah.ac.ae

Abstract

In cellular manufacturing systems, minimization of the completion time has a great impact on production time, material flow, and productivity. An effective scheduling is crucial to attaining the advantages of cellular manufacturing systems.

In this paper, a Hybrid Particle Swarm Optimization (PSO-SA) algorithm is proposed to solve a cellular flowshop scheduling problem with family sequence-dependent setup time. The proposed PSO-SA algorithm combines Particle Swarm Optimization (PSO) algorithm with Simulated Annealing (SA) as a local search to balance between diversification and intensification. The objective is to find the best sequence of families as well as jobs in each family in order to minimize total flow time; the problem is classified as: $F_m \setminus fmls, Selki, prum \setminus \sum_{j=1}^N C_j$.

The research problem is shown to be an NP-hard problem. PSO-SA is developed to improve the effectiveness of the PSO algorithm and to reduce the average variation from the lower bounds.

The performance the proposed PSO-SA is evaluated based on the Relative Percentage Deviation (RPD) from lower bounds and compared with the best available algorithm.

Results showed that the hybridization of the PSO with SA improves the quality of the PSO algorithm and reduces the gap from the lower bounds especially for large problems.

keywords

Particle Swarm Optimization, Simulated Annealing, Cellular flowshop, Sequencing-dependent setup time, Total Flow Time, Hybridization, Local search.

خوارزمية PSO-SA الهجينة للتخطيط لحلقة تدفق الخلايا مع أوقات ترتيب تعتمد على تسلسل العائلة

في أنظمة التصنيع الخلوية، يكون لتقليل وقت الإكمال تأثير كبير على وقت الإنتاج وتدفق المادة والإنتاجية. التخطيط الفعال أمر بالغ الأهمية لبلوغ مزايا أنظمة التصنيع الخلوية. في هذه الورقة، تم اقتراح خوارزمية تحسين الجسيمات المختلطة (PSO-SA) لحل مشكلة جدولة التدفقات الخلوية مع وقت الإعداد المعتمد على التسلسل العائلي. تجمع خوارزمية PSO-SA المقترحة بين خوارزمية تحسين سرب الجسيمات (PSO) وخواص الصلب المحاكاة (SA) كبحت محلي لتحقيق التوازن بين التنوع والتكيف. الهدف هو إيجاد أفضل تسلسل للعائلات بالإضافة إلى وظائف في كل عائلة من أجل تقليل وقت التدفق الإجمالي. تبين أن مشكلة البحث مشكلة NP-صعبة. تم تطوير PSO-SA لتحسين فعالية خوارزمية PSO ولتقليل التباين المتوسط مقارنة بالحدود الدنيا. يتم تقييم أداء PSO-SA المقترح بناءً على الفجوة النسبية (RPD) من الحدود الدنيا ومقارنته بأفضل خوارزمية متاحة. أظهرت النتائج أن تهجين PSO مع SA يحسن جودة خوارزمية PSO ويقلل الفجوة للحدود الدنيا خاصةً للمشاكل الكبيرة.

1 Introduction and Problem definition

Flowshop group scheduling problem has received much attention in the academic and practice-oriented literature Due to its practical relevance [1]. Manufacturing organizations seek productive efficiency or cost-effectiveness solutions by competing via fast time to market and low production costs [2]. Cellular Manufacturing (CM) uses Group Technology (GT) in grouping machines according to parts processed. GT is a philosophy to put the products with similar design or manufacturing characteristics or both in one group [3]. CM aims to improve the productivity by grouping the parts into part families based on their similarity such as production requirements and setup times. Further, production scheduling is a decision-making process that improves the utilization; it deals with the allocation of resources to tasks over given periods and its goal is to optimize one or more objectives [4]. An efficient job scheduling is a crucial aspect of any manufacturing environment. Thus, the next step for improving the efficiency of a manufacturing cell is to find the best sequence of processing the assigned parts (jobs). The problem is (classified as: $F_m \setminus fmls, Selki, prum \setminus \sum_{j=1}^N C_j$); and known as Flowshop Manufacturing Cell Scheduling Problem (FMCSP) or Cellular Flowshop Scheduling Problem [5]. Most of the existing research focuses on minimization of Makespan (MS) due to its lower computational complexity. MS computes the maximum completion time; the completion time of last job to be processed on the last machine. Total Flow Time (TFT) computes the sum of completion times of jobs over the last machine. Minimization of TFT reflects a stable utilization of resources, reduces the work-in-process inventory, and minimizes setup times costs. Therefore, TFT is more relevant to a dynamic production environment [6]. Moreover, the minimization of TFT of the jobs will reduce the production time, and decrease the number of delayed deliveries. Consequently, productivity, and profitability of the firm will be increased. For example, a company may receive several orders from different customers, and all of them have the same priority (weight) for the company. Minimization of TFT is appropriate as it would indirectly minimize the Work- In-Process inventories (WIP). Therefore, The main goal of this paper is to find the best sequence of part families as well as the jobs or parts in a part family in order to minimize total flow time.

The mentioned problem "Scheduling a flowshop of cellular manufacturing systems with family setup times" was studied for the first time by [7]. Schaller et al. developed several heuristic algorithms with minimization of the makespan as the criteria. Further, they developed a lower bounding method to evaluate the solution quality of the proposed heuristic algorithms. A Genetic algorithm (GA) and a Memetic algorithm (MA) with local search are proposed by [8] for the makespan minimization. They concluded that the solution quality of the MA was outperformed the available algorithms. Hendizadeh, presented various TS based meta-heuristics for FMCSPs with SDSTs to minimize makespan [9]. They proposed the concepts of elitism and the acceptance of worse moves from SA to improve intensification and diversification.

1.1 Problem Statement and Assumptions

In a cellular manufacturing environment, machines are grouped into cells. Each cell is dedicated to the production of a specific part family. A cell consists of machines or workstations, arranged in a processing sequence. In FMCSF, there are N_0 jobs which are grouped according to their similarity and production requirements. Therefore, there are F part families $\{1, 2, \dots, F\}$ to be processed in a cell that has m machines $\{M_1, M_2, \dots, M_m\}$. The ultimate goal is to find the best sequence of processing the part families as well as jobs within each family in order to minimize the total flow time and makespan simultaneously. Using the triplet notation [4], the problem can be notated as: $F_m \setminus fmls, Selki, prum \setminus C_{max}, \sum_{j=1}^N C_j$. The solution of the studied problem is achieved in two phases or levels:

1. Sequencing of part families
2. Sequencing of jobs within each part family

The solution representation consists of $F + 1$ segments; the first segment F represents the sequence of part families on each machine, the other segments correspond to the sequence of jobs within each part family [10, 11, ?, 12, 13, 14]. The sequence of part families and the parts within each part family are the same on all machines (permutation flowshop). As shown in Figure 1, for a feasible schedule, a solution π of FMCSF takes the following structure:

$$\Pi = \{\Pi_{[1]}, \Pi_{[2]}, \dots, \Pi_{[f]}, \Pi_{[f+1]}, \dots, \Pi_{[F]}\}$$

where

$$\Pi_{[f]} = \{\Pi_{[f][1]}, \Pi_{[f][2]}, \dots, \Pi_{[f][j]}, \dots, \Pi_{[f][N_f]}\}$$

is the sequence of the jobs in each part family. Figure 1 shows solution structure of part families as well as jobs in each part family:

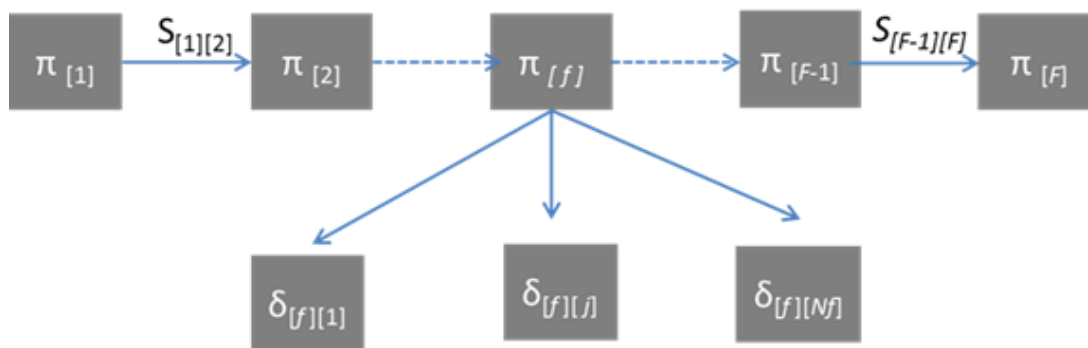


Figure 1: The solution structure of a Flowshop Manufacturing Cell Scheduling Problem [12].

The problem is classified as: $F_m \setminus fmls, Sel_{ki}, prum \setminus \sum_{j=1}^N C_j$. The objective is to minimization of the Total Flow Time (TFT); The following assumptions are used in this research:

- The number of parts (jobs), their processing times, the number of part families, and their setup times are known in advance.
- The sequence of parts and part families are the same on all machines (permutation scheduling).
- Once a part starts to be processed on a machine, the process cannot be interrupted before completion (pre-emption is disallowed).
- Each machine can handle only one part (job) at a time.
- All buffers have unlimited size.
- The jobs belonging to each family should be processed without any preemption by other jobs of other families (group technology assumption).
- The ready time of all parts is zero, i.e, all parts in all part families are available for processing at the start time.
- Setup time depends on both the part to be processed and its preceding part. There is a minor setup time among parts within a family but there is a major (considerable) setup time among the part families.

The minimization of the total flow time was studied for the first time by Salmasi et al [15]. They developed two meta-heuristics based on Tabu Search (TS) and Hybrid Ant Colony Optimization (ACO) algorithm to minimize TFT. They showed that the algorithm had a superior performance compared to the TS algorithm and it has been considered as the best available metaheuristic. They developed an efficient lower bound based on the Branch- and-Price for total flow time minimization. Naderi et al [16] studied the proposed problem, and they developed two different mixed integer linear programming models and showed that the models are effective in solving small and medium sized problems and provide the optimum solution in a reasonable time. They developed a hybrid genetic and simulated annealing algorithm, called (GSA) to solve the problem heuristically and proved that the proposed mathematical models and the proposed metaheuristic algorithm outperformed the available algorithms in the literature.

As a result of the limited work done on the TFT minimization, more algorithms are needed to minimize the TFT. The contribution of the work is to develop a hybrid algorithms combining PSO and SA to balance between diversification and intensification. Furthermore, the PSO-SA is developed to improve the effectiveness of the PSO algorithm and to reduce the average variation from the lower

bounds and to improve the quality of the obtained solutions by PSO algorithm. Therefore, this paper presents the a hybrid algorithm (PSO-SA) to solve the FMCSFs with SDSTs to minimize the TFT.

2 Proposed Algorithms: PSO, and PSO-SA

Particle Swarm Optimization (PSO) is a novel iterative computational evolution model that was developed by Kennedy and Eberhart [17]. An overview of important work and research directions on particle swarms as well as applications are presented by Poli et al [18]. Liu proposed an effective particle swarm optimization (PSO) based memetic algorithm (MA) for the permutation flow shop scheduling problem to minimize the makespan [19]. A novel PSO algorithm for the permutation flowshop scheduling is applied by Lian et al [20] to minimize makespan. Tseng developed a PSO algorithm for the scheduling of multiprocessor tasks in a multistage hybrid flowshop with makespan minimization [21]. Kuo proposed a hybrid PSO model named (HPSO) that combines random-key encoding scheme, individual enhancement (IE) scheme, and PSO to solve the flowshop scheduling problem to minimize makespan [22]. RameshKumar et al [23] proposed a Discrete Particle Swarm Optimization (DPSO) algorithm to solve permutation flowshop scheduling problems with the objective of minimizing the makespan . Lin et al [24] presented a hybrid algorithm combined PSO algorithm with SA technique, and multi-type individual enhancement scheme to solve the job-shop scheduling problem. Liu et al [25] proposed a hybrid PSO with estimation of distributed algorithms to solve permutation flowshop scheduling problem to minimize the makespan. Gohar and Salmasi proposed several hybrid metaheuristic algorithms based on PSO and SA to heuristically solve the flexible flow-line scheduling problem by considering constraints for the beginning and terminating times of processing the jobs. The objective again was to minimize the makespan [26].

Simply, PSO algorithm simulates birds swarm behaviour, and makes every particle in the swarm move according to its experience and the best particles experience to find a new better position. After the evolution, the best particle in the swarm is seen as the best solution for the input problem. The population of PSO is called swarm and each individual or particle which is a potential solution is known with its current position and current velocity. The new position of each individual particle is obtained by assigning a new position as well as a new velocity to the particle. Each particle gains a different position, and the value of each position is evaluated based on the value of the objective function. The main advantage of this approach is that every particle always remembers its best position in the experience. When a particle moves to another position, it must refer to its best experience and the best experience of all particles in the swarm. The best position of each particle that has been gained so far during the previous steps is called the best particle (p-best). The best position gained by all particles so far is called the global best (g-best).

The new position as well as the new velocity of each particle are obtained based on the previous positions, the p-best, and the g-best. Considering an n-dimension search space, there are S particles (swarm size) cooperating to find the global optimum in the search space. In a swarm of S particles, the i^{th} particle is associated with the position vector $\{x_{i1}, x_{i2}, \dots, x_{in}\}$ and the velocity $\{v_{i1}, v_{i2}, \dots, v_{in}\}$.

The p-best and g-best are updated each iteration based on generation of new swarms. Each particle uses its own search experience and the global experience by the swarm to update the velocity and flies to a new position based on the following equations:

$$v_j(t+1) = wv_j(t) + C_1r_1^*(P_j^t - x_j(t)) + C_2r_2^*(G^t - x_j(t)) \quad (1)$$

$$x_j(t+1) = v_j(t+1) + x_j(t) \quad (2)$$

Where w is the inertia weight, it controls the influence of the previous velocity of particles, C_1 and C_2 are called acceleration coefficients that provide weight to the social influence. The parameters r_1 and r_2 are uniformly distributed random variables in the range between $[0, 1]$. For the t^{th} iteration, P_i^t and G^t are the p-best (for i^{th} particle) and g-best particles respectively. The values of these parameters are updated in each iteration based on the following equations:

$$w = w^{min} + \frac{w^{max} - w^{min}}{1 + e^{\frac{-a(maxI-t)}{maxI}}} \quad (3)$$

$$C_1 = C_1^{min} + \frac{C_1^{max} - C_1^{min}}{1 + e^{\frac{-a(maxI-t)}{maxI}}} \quad (4)$$

$$C_2 = C_2^{min} + \frac{C_2^{max} - C_2^{min}}{1 + e^{\frac{-a(t)}{maxI}}} \quad (5)$$

The maximum and minimum values of the above parameters are presented in Table 1, where I is the current iteration, $maxI$ is the pre-set value of maximum number of iterations, and is constant equal to 10. Particles fly in the search space based on equation (1), and equation (2). Every particle always remembers its best position in the experience. When a particle moves to another position, new velocity is calculated according to the previous velocity and the distance of its position from both p-best and g-best. However, the new velocity is limited to the range to control the extreme traveling of particles outside the search space. Particles gain their new positions according to the new velocity and the previous position equation (1) and equation (2). Liu et al [27] implemented Ranked Order Value (ROV) to convert the continuous position value of the particles to job sequence to solve permutation flowshop scheduling problem. In this study, ROV is implemented to convert the position of particles to part families sequences as well the sequence of jobs in each part family.

Table 1: The maximum and minimum values of PSO parameters

Parameter.	Max. values	Min. values
W	2	0.4
C_1	2	0.4
C_2	2	0.4
Position value	0	4
Velocity	-4	4

2.1 Initial Swarm

The algorithm starts with generating the initial velocity and position for j^{th} particle in the swarm of size $N\{j \in \{1, 2, \dots, N\}\}$ according to the following equations:

$$X_{0i} = X_{min} + r_1(X_{max} - X_{min}), \quad (6)$$

$$V_{0i} = V_{min} + r_2(V_{max} - V_{min}), \quad (7)$$

The subscript 0 refers to the starting point, i.e., before the iterations are started. X_{min} , and X_{max} represent the minimum and maximum position values. V_{min} , and V_{max} represent the minimum and maximum velocities. Also r_1 and r_2 are random variables in the range between $[0, 1]$. Therefore, the initial position of particle X_i will be as follows:

$$X_i = \begin{pmatrix} X_{i11} & X_{i12} & \cdots & X_{i1,N_1} \\ X_{i21} & X_{i22} & \cdots & X_{i2,N_2} \\ \vdots & \vdots & \ddots & \vdots \\ X_{if1} & X_{if2} & \cdots & X_{if,N_f} \\ X_{i(F+1)1} & X_{i(F+1)2} & \cdots & X_{i(F+1)F} \end{pmatrix} \quad (8)$$

Particle flies in the search space with velocity matrix V_i

$$V_i = \begin{pmatrix} V_{i11} & V_{i12} & \cdots & V_{i1,N_1} \\ V_{i21} & V_{i22} & \cdots & V_{i2,N_2} \\ \vdots & \vdots & \ddots & \vdots \\ V_{if1} & V_{if2} & \cdots & V_{if,N_f} \\ V_{i(F+1)1} & V_{i(F+1)2} & \cdots & V_{i(F+1)F} \end{pmatrix} \quad (9)$$

Where F refers to number of families and N_f is maximum number of jobs of family f .

2.2 Ranked Order Value (ROV)

Ranked Order Value (ROV) is based on the random representation of permutation of jobs [22], [27]. ROV is included in the proposed PSO algorithms to convert the continuous position of particles to a permutation of families as well as jobs. Basically, ROV is applied based on Smallest Particle Value (SPV); firstly handled and assigned a smallest rank value 1. Then, the second SPV is assigned a rank value 2. Similarly, all the position values will be dealt with to convert the position information of a particle to a family and a job sequence. For example, if we have particles information about a sequence of 4 families with these values of $X_i = \{0.12, 0.22, 0.06, 1.14\}$, based on ROV method, the sequence of these families is $\{3, 2, 1, 4\}$. ROV is used to convert all random numbers generated to a sequence of families as well as the jobs in each iteration (after updating the velocity and position of particles in the swarm). The steps of the PSO algorithm are executed as follows in Algorithm 1.

In this study, two metaheuristics based on Particle Swarm Optimization (PSO) which is a population-based metaheuristic, and Simulated Annealing (SA) which is a single solution based metaheuristic are combined into two different strategies. First, PSO is used to generate the initial solution of the SA algorithm. Second, SA is combined with PSO algorithm as a local search engine. The fundamental concept of the cooperation between PSO and SA is due to the following reasons: 1) The ability of PSO to locate high performance regions of vast search spaces quickly; 2) The simplicity of SA algorithm; and 3) The successful implementation of SA for solving scheduling problems. Therefore, PSO can be applied to locate promising regions. Then, it is highly recommended to apply a single solution based algorithm (such as SA) which is a powerful optimization method in terms of exploitation [28] to be combined with PSO as a local search.

Algorithm 1 The steps of the proposed PSO algorithm

Require: Initialize parameters { swarm size n , maximum Iteration I_{max} , $C_{1max}, C_{1min}, C_{2max}, C_{2min}, V_{max}, V_{min}, W_{max}, W_{min}, X_{max}, X_{min}$ }

- Step 1: Set iteration $t = 0$
- Step 2: If $t = 0$
 - Generate initial positions X_i^t and V_i^t initial velocities for $i \in \{1, 2, \dots, n\}$ according to equations (6, and 7)
 - Else
 - Generate a new swarm by updating the velocity V_i^t and position X_i^t of particles according to equations (1, and 2)
- Step 3: Apply the (ROV) on X_i^t to find the sequence of families as well as jobs in families.
- Step 4: Calculate the objective function $f(X_i^t)$ for each particle $i \in \{1, 2, \dots, n\}$
 - o Step 4.1 For each particle in the swarm the p-best (P_i^t) is calculated as:

$$P_i^t = \operatorname{argmin}_{X_i^j} f(X_i^j) \quad \text{for } j \in \{1, 2, \dots, t\}$$

- o Step 4.2 The g-best can be calculated as:

$$G^t = \operatorname{argmin}_{P_i^t} f(P_i^t) \quad \text{for } i \in \{1, 2, \dots, n\}$$

- Step 5 Set $t = t + 1$
 - Step 6 If $t = I_{max}$, STOP; else, go to step 3.
-

2.3 Simulated Annealing (SA) Algorithm

SA is a meta-heuristic approach that can provide optimal (or near-optimal) solutions to combinatorial optimization problems. Since its introduction by Kirkpatrick et al (1983) [29]. SA has been applied to a vast number of optimization problems. SA approach starts from an initial sequence (current solution), and then moves successively among the neighboring sequences to generate another solution. Basically, SA is a two step process: perturb (generate a new solution), and then evaluate the quality of the new solution [30]. Eglese provided an overview to implement the SA algorithm [31]. For the sake of getting an overview about simulated annealing algorithm readers are referred to references [32, 33]. A metaheuristic based on SA is proposed by Vakharia et al [34] to schedule part families as well as jobs with each part family for FMCSP with SDST. Sridhar et al [35] proposed an algorithm based on SA for scheduling the FMCSP (without considering the setup times) to minimize the total flow time.

Annealing is the process through which slow cooling of metal produces uniform, low energy-state crystallization, whereas fast cooling produces poor crystallization. The optimization procedure of SA algorithm to find a near global minimum mimics the crystallization cooling procedure. SA procedure starts with a random initial solution as the current solution. Then, the algorithm generates a new solution from the predetermined neighbourhood. The initial solution is randomly generated by using the initial position and velocity according to equations 6, and 7. The steps of SA algorithm are shown in Algorithm 2. The fitness value of the new solution is then compared with the current solution to determine if the new one is better. For minimization problems, if the fitness value of the new solution is smaller than that of the current one, the new solution is automatically accepted and becomes the current solution from which the search continues. The algorithm will then proceed with further iterations. Larger fitness values for next solution may also be accepted as the current solution under certain conditions to escape from a local minimum.

2.4 SA procedure

The procedure of the proposed SA starts with setting the levels of parameters. The current state or temperature T is set to the initial value T_0 . An initial solution X is randomly generated and it is considered as the current solution. For each iteration, the next solution Y is generated from the current solution by perturbation on job sequence or on family sequence using the swapping and insertion techniques. Consider E_i as the energy state of the fitness value of current solution and E_j is the fitness value of the new solution obtained as a result of the manipulation of the job sequence within a family F . Let $\Delta E = E_j - E_i$; which refers to the difference between $\Delta E = TFT(Y) - TFT(X)$. If $\Delta E \leq 0$, the probability of replacing current solution X with the new solution Y is 1. If $\Delta E > 0$, then, probability of accepting the new solution depends on the Cauchy $\left(\frac{T}{T^2+(\Delta E)^2}\right)$ function. The new solution replaces the current solution, if $\left(\frac{T}{T^2+(\Delta E)^2}\right)$ is greater than some random number RN between 0 and 1. Then, temperature T is reduced based on cooling rate after running maximum number of iterations (Ite) from the previous decrease, according to the formula (the typical value of α is 0.95). The algorithm is terminated if T is lower than T_f . During the search evolutions, the best solution with the least total flow time is recorded. The algorithm is also terminated if the current solution is not improved in non-improving successive reductions in temperature. Following the termination of the SA procedure, the near- global optimal schedule is X_{best} with total flow time TFT_{best} .

2.5 Hybrid Particle Swarm Optimization algorithm

In designing metaheuristics, two conflicting criteria must be taken into account: exploration of the search space (diversification) and exploitation of the best solutions found (intensification) [?]. Promising regions are determined by the obtained good solutions. On one hand, in intensification,

Algorithm 2 The steps of the proposed SA algorithm

Require: Initialize SA parameters and set a solution X to be current solution $\{ T_0, T_F, \alpha = 0.95, I_{iter}, N_{non-imp.} \}$

- Step 1: Set iteration $t = 0$
 - Step 2: For $F=1$ to Family size
Set $T = T_0$, No. of Moves = 1, and counter = 1
 - Step 2.1: while $T > T_F$ do:
 - o Step 2.1.1: if $F=1$, Generate by swapping the family sequence
Else
Generate a new neighbour solution Y from current solution X by minor swapping on job sequence of F^{th} family, and calculate the difference in objective functions of X , and Y to be $\Delta E = TFT(Y) - TFT(X)$
 - o Step 2.1.2: IF $\Delta E \leq 0$, then replace the current solution with the new solution and go to Step 2.1.4; otherwise, go to Step 2.1.3
 - o Step 2.1.3: Generate a random number RN in the range $[0, 1]$
IF $RN < \frac{T}{T^2 + (\Delta E)^2}$, then replace solution with solution Y and go to Step 2.1.4
 - o Step 2.1.4: Increment No. of Moves by one. IF No. of Moves $< N_{non-imp.}$, then go to Step 2.1.1; Else, go to Step 2.1.5
 - o Step 2.1.5: IF the best solution is improved, then restart the counter from zero; otherwise, increase the counter by one unit
 - o Step 2.1.6 IF counter = I_{iter} , decrease the temperature using geometric schedule $T = \alpha T$, make No. of Moves = 1, and go to Step 2.1.
 - Step 3: Return the current solution in the end as X_{best} with TFT_{best}
-

the promising regions are explored more thoroughly in the hope to find better solutions. On the other hand, in diversification non-explored regions have be visited to be sure that all the regions of the search space are explored. Therefore, the proposed algorithm should compromise and balance between diversification and intensification criteria. Moreover, hybridization is implemented to balance between these criteria and to manage the cooperation between the operation of the search among the candidate solutions (populations or swarms), a diversifying agent, and the intensifying agent. The hybrid approach implanted in this study to balance between intensification and diversification is shown in Figure 2. PSO is used to perform the global search, and SA algorithm is combined as a local search to improve quality of search.

The main goal of hybridizing the PSO algorithm is to improve the quality of the obtained solution

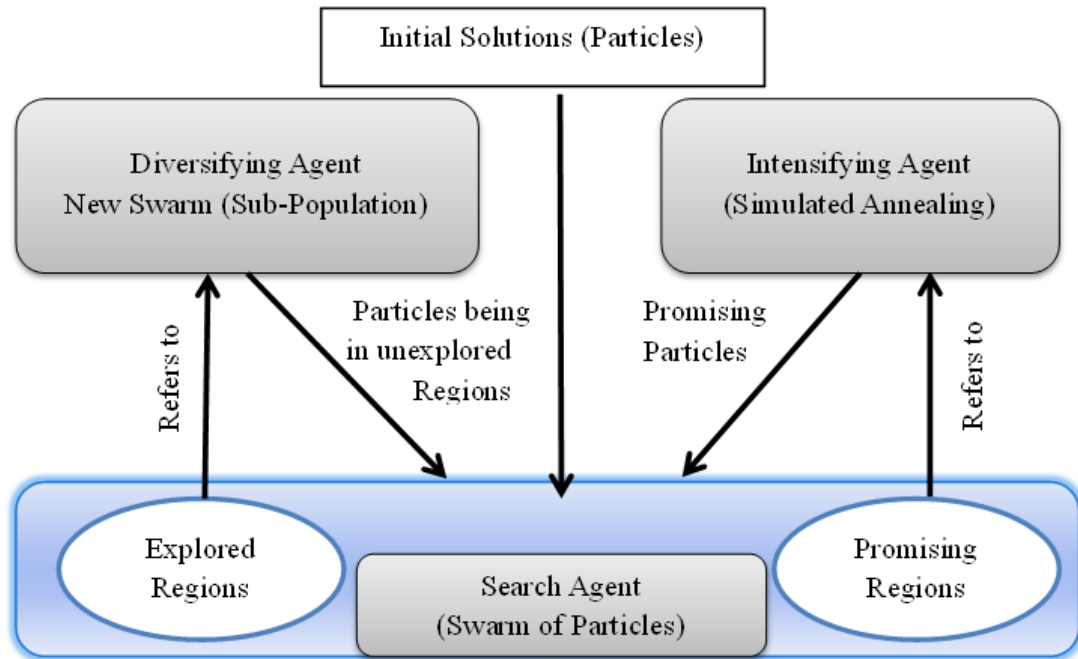


Figure 2: Hybridization of particle swarm optimization and simulated annealing

using a pure PSO metaheuristic. SA is basically combined with PSO as a local search to find better solutions. At the first stage, PSO is proposed to solve the studied problem, and it showed a better performance than other algorithms such as GA proposed by the author [36]. The proposed PSO algorithm provides very good solutions that matched the best existing algorithms for small and medium instances. For large problems, the performance of the PSO algorithm deviates from the best solutions due to the large solution space, and the higher probability to be trapped in local optima. Therefore, PSO has been combined with SA to improve the quality of solutions and reduce the variation from the lower bounds for the large problem instances. The main role of combining SA algorithm with PSO is to enhance the intensification and search for a better solution within the neighbourhoods (this combination is named PSO-SA).

In the PSO-SA, each particle flies in the solution space seeking for a better position based on its best experience (p-best), and the global experience (g-best) based on the new velocity and new position (equations 6, and 7). Therefore, particles are enhanced to move toward the global optima. A local search engine based on SA is implemented to search on the neighbourhood of the g-best particle each iteration by using swapping of the job sequences in families. Note that swapping is implemented only to the job sequence for simplicity. Local search is conducted on the g-best particle in each iteration. The procedure of the proposed PSO-SA algorithm is similar to the proposed PSO algorithm. As compared to algorithm 1, the PSO-SA algorithm shown in algorithm 3 differs only in step 6, where a local search based on SA (denoted by L.S) is incorporated with PSO to improve g-best particle that improves the searching and finding promising regions in next iterations of PSO.

Algorithm 3 The steps of the proposed PSO-SA algorithm

Require: Initialize parameters { swarm size n , maximum Iteration I_{max} , $C_{1max}, C_{1min}, C_{2max}, C_{2min}, V_{max}, V_{min}, W_{max}, W_{min}, X_{max}, X_{min}$ }

- Step 1: Set iteration $t = 0$
 - Step 2: If $t = 0$
 - Generate initial positions X_i^t and V_i^t initial velocities for $i \in \{1, 2, \dots, n\}$ according to equations (6, and 7)
 - Else
 - Generate a new swarm by updating the velocity V_i^t and position X_i^t of particles according to equations (1, and 2)
 - Step 3: Apply the (ROV) on X_i^t to find the sequence of families as well as jobs in families.
 - Step 4: Calculate the objective function $f(X_i^t)$ for each particle $i \in \{1, 2, \dots, n\}$
 - o Step 4.1 For each particle in the swarm the p-best (P_i^t) is calculated as:
$$P_i^t = \underset{X_i^j}{\operatorname{argmin}} f(X_i^j) \quad \text{for } j \in \{1, 2, \dots, t\}$$
 - o Step 4.2 The g-best can be calculated as:
$$G^t = \underset{P_i^t}{\operatorname{argmin}} f(P_i^t) \quad \text{for } i \in \{1, 2, \dots, n\}$$
 - Step 5 Set $t = t + 1$
 - Step 6 Set $G^t = L.S(G^t)$
 - Step 7 If $t = I_{max}$, STOP; else, go to step 2.
-

3 Results and discussion

The proposed PSO-SA algorithm is coded using C++ language and run on a PC with an Intel ® core I7 (2.93 GHz) CPU and 4.0 GB memory. The analysis of performance of PSO-SA versus the other proposed algorithms is presented in Section 4.5. The performance of the proposed PSO-SA algorithm is compared with the best available algorithms in the literature. PSO-SA performs similar to the best available algorithm (ACO) developed by Salmasi et al [?] for solving most of the test problems for the six-machine test. However, there is a very small deviation from the best in solving the large size problems for two-machine test problems as shown in Figures 3 and 4. As a result of the adding of SA algorithm as a local search, the performance of the PSO algorithm has been improved and matched with the best available algorithm.

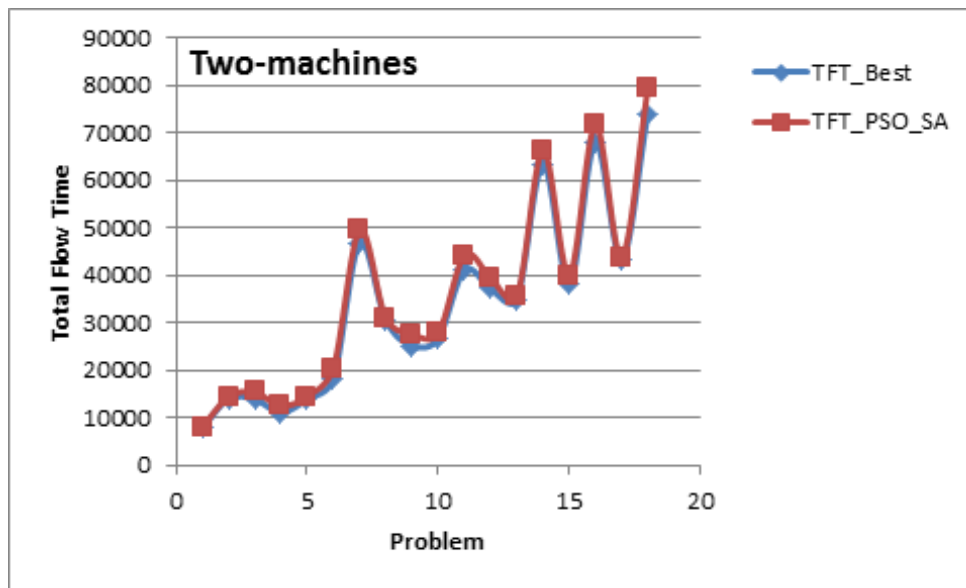


Figure 3: Performance of the proposed PSO-SA vs. ACO for 2-machine problems

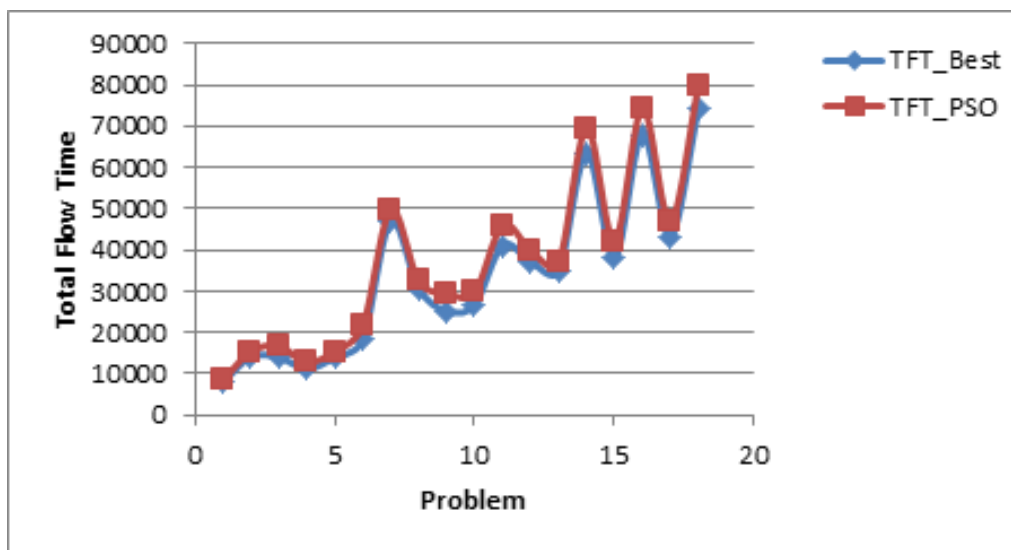


Figure 4: Performance of the proposed PSO vs. ACO for 2-machine problems

4 Conclusion

A Hybrid Particle Swarm Optimization (PSO-SA) algorithm has been developed to solve the Flow-shop Manufacturing Cell Scheduling Problem with Sequence Dependent Setup Times (FMCSP with SDSTs) to minimize the total flow time. Results showed that the PSO-SA is outperform the PSO algorithm especially for the large problems. The results of proposed algorithm was compared with best available algorithm and showed the same results in a reasonable computation time. Implementing the SA algorithm as a local search improves the quality of the obtained solutions due to the balance between diversification and intensification. As a result of the limited work on the

proposed problem, there is room for designing more algorithms based on a pure metaheuristic algorithm or combination of different metaheuristics. For instance, Ant Colony Optimization (ACO) could be combined with a single solution based algorithm such as Variable Neighborhood Search (VNS).

References

- [1] J. S. Neufeld, J. N. D. Gupta, and U. Buscher, "A comprehensive review of flowshop group scheduling literature," *Computers and Operations Research*, vol. 70, pp. 56–74, 2016.
- [2] F. Zhao, J. Tang, and J. Wang, "An improved particle swarm optimization with decline disturbance index (DDPSO) for multi-objective job-shop scheduling problem," *Comput. Oper. Res.*, vol. 45, pp. 38–50, may 2014.
- [3] M. Zandieh, B. Dorri, and a. R. Khamseh, "Robust metaheuristics for group scheduling with sequence-dependent setup times in hybrid flexible flow shops," *Int. J. Adv. Manuf. Technol.*, vol. 43, no. 7-8, pp. 767–778, sep 2008.
- [4] M. Pinedo, *Scheduling: theory, algorithms, and systems*. Springer, 2012.
- [5] S. Lin, K. Ying, and Z. Lee, "Metaheuristics for scheduling a non-permutation flowline manufacturing cell with sequence dependent family setup times," *Comput. Oper. Res.*, vol. 36, no. 4, pp. 1110–1121, apr 2009.
- [6] L.-Y. Tseng and Y.-T. Lin, "A genetic local search algorithm for minimizing total flowtime in the permutation flowshop scheduling problem," *Int. J. Prod. Econ.*, vol. 127, no. 1, pp. 121–128, sep 2010.
- [7] J. Schaller, J. N. D. Gupta, and A. J. Vakharia, "Scheduling a flowline manufacturing cell with sequence dependent family setup times," *Eur. J. Oper. Res.*, vol. 125, no. 2, pp. 324–339, sep 2000.
- [8] P. Franca, J. Gupta, A. Mendes, P. Moscato, and K. Veltink, "Evolutionary algorithms for scheduling a flowshop manufacturing cell with sequence dependent family setups," *Comput. Ind. Eng.*, vol. 48(3), pp. 491–506, 2005.
- [9] S. Hamed Hendizadeh, H. Faramarzi, S. Mansouri, J. N. Gupta, and T. Y ElMekkawy, "Metaheuristics for scheduling a flowline manufacturing cell with sequence dependent family setup times," *Int. J. Prod. Econ.*, vol. 111, no. 2, pp. 593–605, feb 2008.

- [10] S.-W. Lin, J. N. Gupta, K.-C. Ying, and Z.-J. Lee, "Using simulated annealing to schedule a flowshop manufacturing cell with sequence-dependent family setup times," *Int. J. Prod. Res.*, vol. 47, no. 12, pp. 3205–3217, jun 2009.
- [11] N. Salmasi, R. Logendran, and M. R. Skandari, "Makespan minimization of a flowshop sequence-dependent group scheduling problem," *Int. J. Adv. Manuf. Technol.*, feb 2011.
- [12] R. Bouabda, B. Jarboui, M. Eddaly, and A. Rebai, "A branch and bound enhanced genetic algorithm for scheduling a flowline manufacturing cell with sequence dependent family setup times," *Comput. Oper. Res.*, vol. 38, no. 1, pp. 387–393, 2011.
- [13] M. Eddaly, B. Jarboui, R. Bouabda, and A. Rebai, "Hybrid Estimation of distribution algorithm for permutation flowshop scheduling with dependent family setup times," in *2009 Int. Conf. Comput. Ind. Eng.*, 2009, pp. 217–220.
- [14] S. Hamed Hendizadeh, H. Faramarzi, S. Mansouri, J. N. Gupta, and T. Y ElMekkawy, "Meta-heuristics for scheduling a flowline manufacturing cell with sequence dependent family setup times," *International Journal of Production Economics*, vol. 111(2), pp. 593–605, 2008.
- [15] N. Salmasi, R. Logendran, and M. R. Skandari, "Total flow time minimization in a flowshop sequence-dependent group scheduling problem," *Computers & Operations Research*, vol. 37, no. 1, pp. 199–212, jan 2010.
- [16] B. Naderi and N. Salmasi, "Permutation flowshops in group scheduling with sequence-dependent setup times," *Eur. J. Ind. Eng.*, vol. 6, no. 2, pp. 177–198, 2012.
- [17] J. Kennedy and R. Eberhart, "Particle swarm optimization," *Proc. ICNN'95 - Int. Conf. Neural Networks*, vol. 4, pp. 1942–1948, 1995.
- [18] R. Poli, J. Kennedy, and T. Blackwell, "Particle swarm optimization," *Swarm Intell.*, vol. 1, no. 1, pp. 33–57, aug 2007.
- [19] B. Liu, L. Wang, and Y.-H. Jin, "An effective PSO-based memetic algorithm for flow shop scheduling," *IEEE Trans. Syst. Man. Cybern. B. Cybern.*, vol. 37, no. 1, pp. 18–27, mar 2007.
- [20] Z. Lian, X. Gu, and B. Jiao, "A novel particle swarm optimization algorithm for permutation flow-shop scheduling to minimize makespan," *Chaos, Solitons & Fractals*, vol. 35, no. 5, pp. 851–861, mar 2008.
- [21] C.-T. Tseng and C.-J. Liao, "A particle swarm optimization algorithm for hybrid flow-shop scheduling with multiprocessor tasks," *Int. J. Prod. Res.*, vol. 46, no. 17, pp. 4655–4670, sep 2008.

- [22] I.-H. Kuo, S.-J. Horng, T.-W. Kao, T.-L. Lin, C.-L. Lee, T. Terano, and Y. Pan, “An efficient flow-shop scheduling algorithm based on a hybrid particle swarm optimization model,” *Expert Syst. Appl.*, vol. 36, no. 3, pp. 7027–7032, apr 2009.
- [23] K. Rameshkumar, R. Suresh, and K. Mohanasundaram, “Discrete particle swarm optimization (DPSO) algorithm for permutation flowshop scheduling to minimize makespan,” *Adv. Nat. Comput.*, pp. 572–581, 2005.
- [24] T.-L. Lin, S.-J. Horng, T.-W. Kao, Y.-H. Chen, R.-S. Run, R.-J. Chen, J.-L. Lai, and I.-H. Kuo, “An efficient job-shop scheduling algorithm based on particle swarm optimization,” *Expert Syst. Appl.*, vol. 37, no. 3, pp. 2629–2636, mar 2010.
- [25] H. Liu, L. Gao, and Q. Pan, “A hybrid particle swarm optimization with estimation of distribution algorithm for solving permutation flowshop scheduling problem,” *Expert Syst. Appl.*, vol. 38, no. 4, pp. 4348–4360, apr 2011.
- [26] S. Gohari and N. Salmasi, “Flexible flowline scheduling problem with constraints for the beginning and terminating time of processing of jobs at stages,” *Int. J. Comput. Integr. Manuf.*, pp. 1–14, 2014.
- [27] B. Liu, L. Wang, and Y.-H. Jin, “An effective hybrid PSO-based algorithm for flow shop scheduling with limited buffers,” *Comput. Oper. Res.*, vol. 35, no. 9, pp. 2791–2806, sep 2008.
- [28] E.-G. Talbi, *Hybrid Metaheuristics*, ser. Studies in Computational Intelligence, E.-G. Talbi, Ed. Berlin, Heidelberg: Springer Berlin Heidelberg, 2013, vol. 434.
- [29] S. Kirkpatrick, C. Gelatt, and M. Vecchi, “Optimization by simulated annealing,” *Science*, pp. 671–680, 1983.
- [30] S. Ledesma, G. Aviña, and R. Sanchez, “Practical considerations for simulated annealing implementation,” *Simulated Annealing*, no. February, pp. 401–420, 2008.
- [31] R. W. Eglese, “Simulated annealing: a tool for operational research,” *Eur. J. Oper. Res.*, vol. 46, pp. 271–281, 1990.
- [32] R. Rutenbar, “Simulated annealing algorithms: An overview,” *Circuits Devices Mag. IEEE*, no. x, 1989.
- [33] F. Buseti, “Simulated annealing overview,” *World Wide Web URL [www. geocities. com/ DOI10.1.1.66.5018](http://www.geocities.com/DOI10.1.1.66.5018)*, 2003.

- [34] A. J. Vakharia and Y.-L. Chang, “A simulated annealing approach to scheduling a manufacturing cell,” *Nav. Res. Logist.*, vol. 37, no. 4, pp. 559–577, aug 1990.
- [35] J. Sridhar and C. Rajendran, “Scheduling in a cellular manufacturing system: a simulated annealing approach,” *Int. J. Prod. Res.*, vol. 31, no. 12, pp. 2927–2945, dec 1993.
- [36] A.-m. Ibrahim, T. Elmekawy, and Q. Peng, “Robust Metaheuristics for Scheduling Cellular Flowshop with Family Sequence- Dependent Setup Times,” *Procedia CIRP*, vol. 17C, pp. 428–433, 2014.

A Comprehensive Review on NO_x & DPM Diesel Engine Emissions and Its Control Techniques

Majid Khan,

Mechanical Engineering, King Fahd University of Petroleum & Minerals, Saudi Arabia

majidk014@gmail.com

Muhammad Mustafa Generous,

Mechanical Engineering, King Fahd University of Petroleum & Minerals, Saudi Arabia

g201708470@kfupm.edu.sa

Minaam Mehmood Hussaini

Civil Engineering, King Fahd University of Petroleum & Minerals, Saudi Arabia

g201705690@kfupm.edu.sa

and

Ahmed Ismail Adam

Civil Engineering, King Fahd University of Petroleum & Minerals, Saudi Arabia

g201704750@kfupm.edu.sa

Abstract

Diesel engine as a power source is widely used in automobile and industrial applications. Although this enormous use boomed the economic development, but it also caused serious environmental hazards. Diesel engine uses combustion phenomenon that gives birth to SO_x, NO_x, soot particles and other dangerous compounds. Diesel engine emissions highly contribute to the atmospheric pollution and other environmental effects. So, their treatment is considered as serious concern and has great significance in evaluation of feasible control techniques. Diesel engine emission encompasses many compounds but NO_x and Diesel particulate matters (DPM) are major emission due to human health and other environmental issues. NO_x and DPM can cause serious health concerns especially for respiratory tract of living being. Therefore, efforts are made to summarize NO_x and DPM formation process and its control techniques in diesel engine. Both Pre-combustion and Post-combustion techniques till to date are discussed and are compared. Various types of fuel additives are also discussed as a control technique for DPM emissions. This comprehensive study has created a junction to list out the numerous techniques evaluated by the various researchers.

Keywords

Exhaust Emission, Particulate matter, NO_x Emission, Emission control techniques, Air pollution.

مراجعة شاملة لانبعاثات محركات الديزل NOx و DPM وتقنيات التحكم فيها

يستخدم محرك الديزل كمصدر للطاقة على نطاق واسع في السيارات والتطبيقات الصناعية. على الرغم من أن هذا الاستخدام الهائل ازدهرت به التنمية الاقتصادية، لكنه تسبب أيضا في مخاطر بيئية خطيرة. يستخدم محرك الديزل ظاهرة الاحتراق التي تولد SOX ، NOX وجزيئات أكاسيد النيتروجين، وغيرها من المركبات الخطيرة. تتسبب انبعاثات محركات الديزل بدرجة كبيرة في تلوث الغلاف الجوي والتأثيرات البيئية الأخرى. كذلك، تعتبر معالجتها مصدر قلق بالغ ولها أهمية كبيرة في تقييم تقنيات التحكم الممكنة.

على الرغم من أن انبعاثات محركات الديزل تضم العديد من المركبات، إلا أن انبعاث أكاسيد النيتروجين NOX وجزيئات الديزل (DPM) تعد من الانبعاثات الرئيسية التي تشكل خطرا على صحة الإنسان والمشكلات البيئية الأخرى. أكاسيد النيتروجين NOX و DPM يمكن أن تسبب مشكلات صحية خطيرة وخاصة بالنسبة للجهاز التنفسي للكائنات الحية. نتيجة لذلك، تبذل الجهود لتلخيص عملية تشكيل أكاسيد النيتروجين NOX و DPM وتقنيات التحكم في محرك الديزل. تناقش لحدّ الآن كل من تقنيات ما قبل الاحتراق وما بعد الاحتراق وتتمّ مقارنتها. وتناقش أيضا أنواع مختلفة من إضافات الوقود كطريقة للتحكم في انبعاثات DPM . هذه الدراسة المعمّقة ولّدت تقاطعا لسرد التقنيات العديدة التي قام بتقييمها مختلف الباحثين.

1. Introduction

Ever increasing energy demand and stringent regulation to control environmental pollutants like the emission of particulates, SO_x and NO_x are pressurizing the researchers to find energy viable and environmental friendly engine emission control technologies [1]. Various techniques were applied to make IC engines such as Diesel engines energy efficient.

In olden times smoke out of the chimney was considered the sign of prosperity of nation and then time changed and stringent laws was imposed to bring pollutants especially SO_x , NO_x , Lead (Pb) emission and particulate emissions from engines to acceptable concentration in order to avoid their effects on human health, property, and aesthetics of the environment [2].

In perfect combustion with clean diesel, combustion exhaust stream should have only CO_2 and H_2O . All carbon in the fuel is oxidized to CO_2 and hydrogen to H_2O . However, in actual conditions, fuel is not pure hydrocarbon and contains some amount of traces of nitrogen, sulfur and other chemicals constituent as impurities. Therefore, in real combustion process different compounds are there in the engine's exhaust in form of solid particles as well some gases. If the air fuel ratio is rich in nature the combustion stream would have CO , soot, black carbon smoke and unburned HC, and the other case when the mixture is lean then combustion process generates NO_x at high temperature conditions as shown by figure 1. Among all exhaust emissions from diesel engine at different range of air fuel ratios, major concerns is associated with NO_x , CO , HC, Smoke (Particles and soot)[3][4].

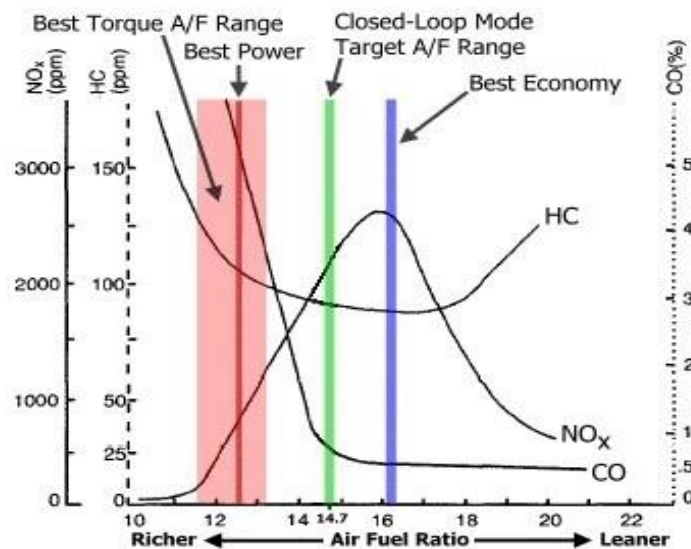


Figure 1. Diesel engine Emission against wide range of operating Air fuel ratios[5]

From Figure 1 it seems that however at all operating fuel mixture range diesel engine exhaust gas is composed of several dissimilar gases like NO , N_2 , CO_2 , H_2O and O_2 . But among them, some are proved to be harmless, but some are considered as harmful and treated as major pollutants. The most dangerous among these, are NO_x and particulate emissions and have different acute health problems[6], [7]. Therefore, it is obligatory to lessen these emissions [8].

In general all control techniques can be classified under the umbrella of two main categories for Diesel engine combustion engines[9] and its schematic is represented in Figure 2.

1. Pre-combustion control techniques 2. Post-combustion control techniques

Pre-combustion control techniques are also known as prevention techniques. These are methods which prevent creation of harmful pollutants inside combustion chamber during the combustion process before they started to generate. While post-combustion control techniques are those method which control the harmful pollutants before there emission or discharge into the ambient air or atmosphere. This kind of techniques deals with the after treatment of emissions once they have been formed [9].

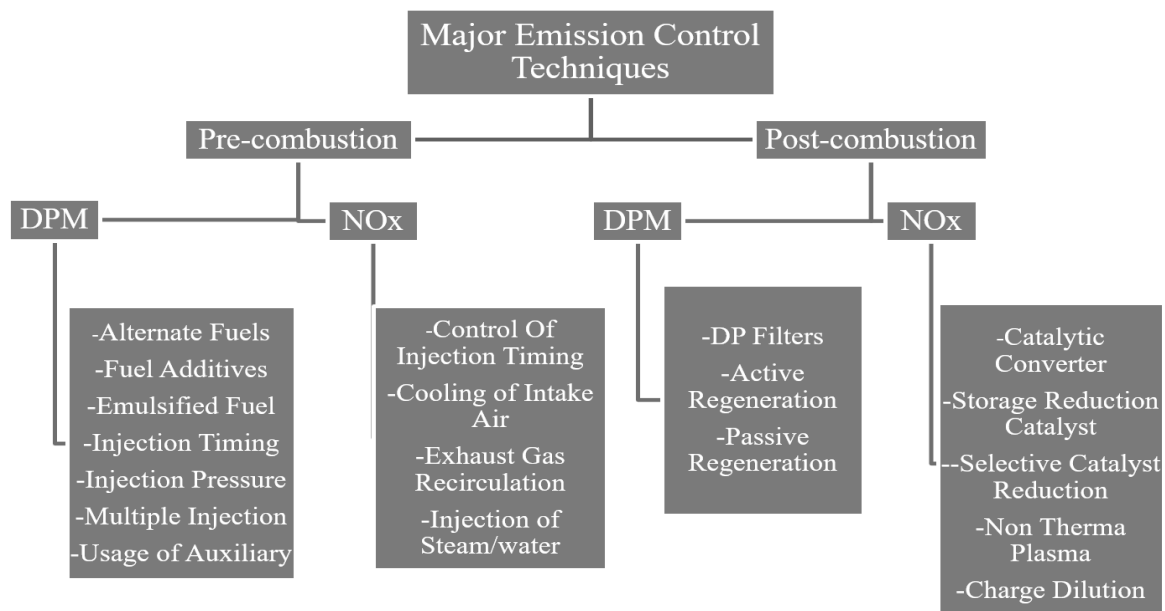


Figure 2. Detailed control emission techniques of NOx & DPM [10].

In this comprehensive review efforts are made to summarize all possible techniques reported to date to control the mentioned major emission. Pre-combustion and post-combustion techniques are separately discussed, and a comparison is made on the work of different researchers. CO₂ emission is not regulated, and study has been made to specifically discuss carbon dioxide emission in relation with NOx and DPM [11].

2. Diesel Particulate Emission and its control techniques

2.1 Particulate Matters and Human Health Concerns

Various studies have been made to explore the effects of DPM on human health. Even models are developed in laboratory experiments by using animal mouse. It has found that DPM especially short size (below 20 nm) is very dangerous for human respiratory system. They have ability to penetrate not only in lungs but also in alveoli of respiratory system. Some finer particles can even penetrate in human blood stream [10], [12]. Studies [11], [12] have shown the effect of fine particulates on lungs and human respiratory system and concluded that they

may cause severe lungs injures and other severe diseases. Long exposure to DPM may leads to lungs cancer. These situation may be alarming for industrial labor working in the environment where they are more likely to be exposed to high concentration of particulates [10], [15], [16]. P. S Glimour et al. stipulated that DPM might lead in the production of free radicals. These radicals may lead to ill function of lungs [18]. Many researchers also reported that exposure to DPM may leads to cough, nausea, guinea pig, bladder cancer and bronchus problems [13], [19]. Moreover, DPM may cause lungs tumor, asthma, skin allergy and allergy. Some finer particles may even have a tendency to penetrate deep into brain and neuron cells. In this way they may cause malfunction of central nervous system. Health hazardous which are briefly summarized in this section forced the researchers to study the composition of DPM, its formation processes and techniques to control these fine particles.

2.2 Composition of DPM

There are various ways to define DPM composition and it be simplify with two major components of DPM namely:

- 1). Organic Portion
- 2) Inorganic Portion.

Organic portion may further be classified as soluble portion and insoluble portion (Fig. 3). Soluble DPM may be extracted from the mixture of burned gases by using different organic solvents. In general DPM are sum of unburned hydrocarbons, with liquid and other solid constituents. [20], [21].

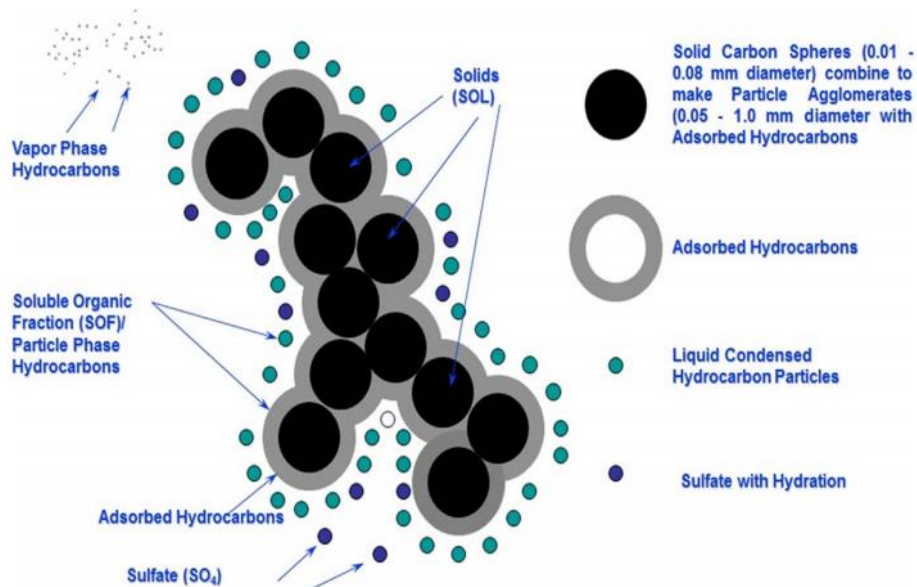


Figure 3. Composition of DPM [10]

2.3 Soot Formation

Soot formation from liquid organic fuel is detailed described by many researchers as Mohankumar et al. [10] [22]. In a condensed form it can summarize in following six steps in Figure 4 [22].

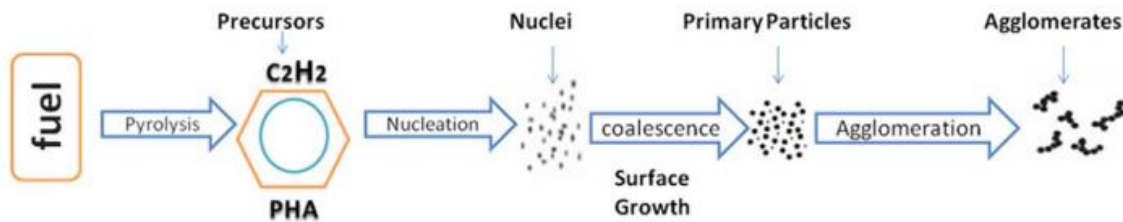


Figure 4. Mechanism Steps of Soot Formation [10].

Table 1. Summary of process forming particulates.

i) Pyrolysis	ii) Nucleation	iii) Growth	iv) Conglomer- -ation	v) Oxidizing environment
-An endothermic process that leads to a change in molecular structure of the compounds at high temperature & in the absence of oxygen contents. -Soot composition & quantity depends on following two factors 1) Temperature 2) Oxygen concentration	-It is Formation of nuclei from gaseous phase in combustion chamber (Fig.3) [10]. -Process takes place at higher temperature (around 1300K). -Initially nuclei are small but later they may combine to form bigger ones.	-Growth occurs when hydrocarbon & other matters stick to the surface of nuclei generated earlier by nucleation. -Growth occurs more for small size particle This is due to reason that small particles have reactive radical concentration.	- Small particles combine to form large particles as result of coalesce. -Particle size increases & their quantity decreases. Sometime these particles may combine in fashion resulting in the formation of chain [22]	Oxygen rich environment suppresses the formation of soot to a much larger extent. This is the reason why premixed type of flame has relatively much less quantity of soot produced during combustion. The formation with flame is given in Figure 5

Premixed flames have higher concentration of oxygen in the mixture as compare diffusion flame. This process is responsible for the production of building blocks of suit [23].

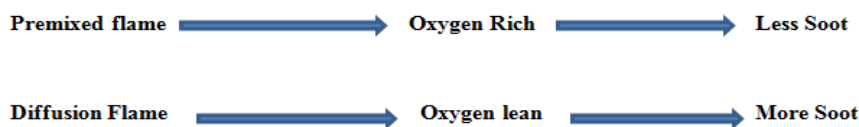


Figure 5. Soot Formation with respect to flame nature

2.4 Fuel Chemistry and Soot Formation

Fuel chemistry plays a major role in determining the quantity and composition of soot. If supplies excess amount of soluble fraction than soot mass may increase. Fuel structure i.e. bonds type and their strength is also major factors. Chemistry of fuel and its effect on soot was studied by many researchers [24], [25]. Table 1 below summarizes relation of soot formation with composition of fuel.

Table 2. Effects of Soot formation of fuel chemistry

Element in the fuel	Effects on the soot formation
Carbon	carbon has direct relation with soot formation. More carbon in the fuel means more soot production.
Oxygen	Oxygen in the fuel has inverse relation with the soot formation. This mean if there is less oxygen in the fuel than less soot will be formed. The best examples are premixed and diffusion flames.
Hydrogen	It also has inverse relation. Fuel with less hydrogen produces more soot.
Sulfur	It has no relation with soot formation but it may increase the mass of soot.

3. Diesel Particulate Matters Control Techniques

Complete Spectrum of DPM techniques is shown in Figure 6 as studied by researchers.

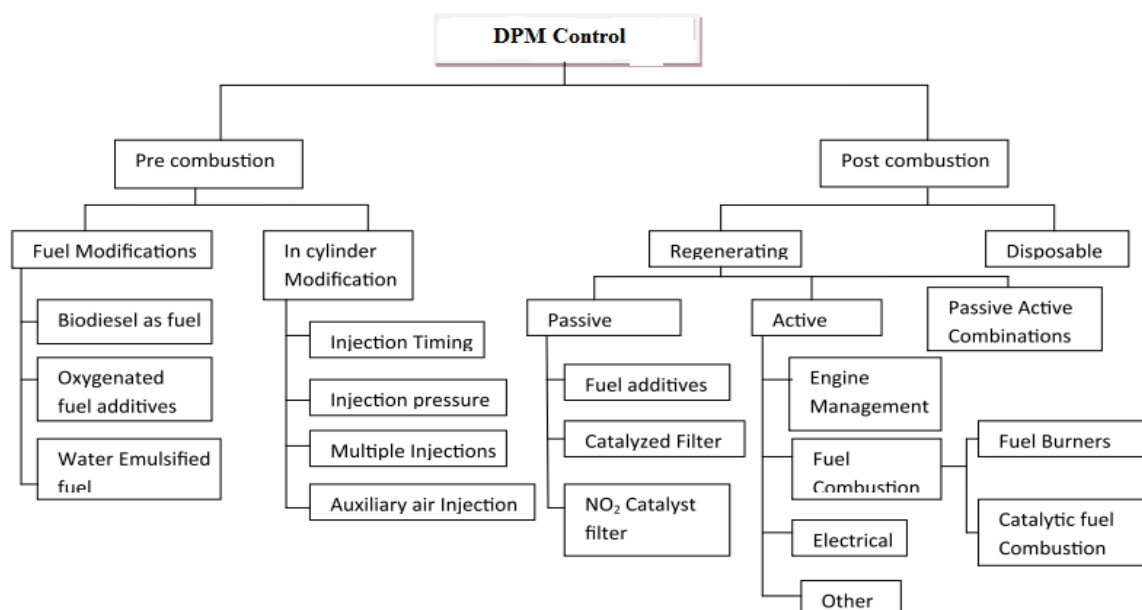


Figure 6. Complete spectrum of Techniques of DPM Emission [10].

3.1 Pre-Combustion Strategies

3.1.1 Alternate Fuels

Biodiesel fuels derived from animal fats and vegetable oils were found to be very effective for the reduction of DPM by many researchers. Diesel engine operated with biodiesel instead of diesel reduces particulate emission to a considerable extent but unregulated emission may increase [28]. Same conclusion was also reported by many other researchers [29]–[31].

3.1.2 Fuel Additives

Various additives like methanol, ethanol, butanol, and ethyl ether are can be used as additives to the diesel engine fuel. These compounds can provide oxygen during chemical reaction. As discussed earlier oxygen rich combustion reduce soot formation by improving cetane number and overall quality of combustion [32]–[34].

3.1.3 Emulsified Fuels

Water emulsified fuels are made by dispersing primary fluid through immiscible secondary fluid. Water has relatively lower boiling point due to which it explodes earlier resulting in longer ignition delay and combustion duration. Process also provide more time for air fuel mixing. All these activities facilitate the reduction of particulate matters in the exhaust of diesel engine. M. Nadeem et al. & many researchers concluded that emulsified fuels reduces DPM and other diesel engine emission with a negligible compromise in the efficiency [35]–[37].

3.1.4 Effects of Injection Timing

Injection time can be used to somehow control DPM emission. Injection time has direct ignition delay. Ignition delay increases with increase in injection time. Increased ignition delay provides an opportunity to air and fuel to pre-mix thoroughly. This through mixing facilitates efficient combustion process resulting in reduction of DPM. Sayin and Canacki [38] investigated the effect of ignition time for different load condition on the emissions of hydrocarbons and came up with the same results.

3.1.5 Effects of Injection Pressure

Injection pressure is another parameter that can help to minimize DPM emissions. Subject was widely investigated by many researchers and same conclusion was drawn. DPM emission shows a rapid decrease with increase in injection pressure. Same conclusion was also reported by Peng Ye, and André L. Boehman [39].

There are three major reasons behind the reduction DPM with increasing injection pressure:

1. Enhancement in injection pressure forces fine atomization of fuel droplets.
2. Fuel droplet size gets reduced.
3. Enhanced pressure causes through mixing pre mixing of air and fuel.

Mohankumar et al. [10] also reported reduction in hole size of nozzle as parameter for reduction in DPM.

3.1.6 Auxiliary Injection Technique

DPM emission can be reduced by injecting air exactly after the end of injection. This can create turbulence and more refine mixing of air and fuel. Therefore, more through mixing results in proper combustion process that may lead to reduction in DPM.

But this technique has a few side effects. First, enhanced heat transfer reduces efficiency of engine. Therefore, it will cost a compromise on efficiency of engine. It may also lead to increase in manufacturing and designing cost as an auxiliary system is required to pump air in to the combustion chamber.

3.1.7 Multiple Injection Technique

Multiple-injection is a technique in which multiple injection strategy is used in a single cycle of combustion. It is effective for both NO_x and DPM control. Its effective was increased by using electronic gadgets to monitor time and injection pressure. Injection can be divided in three segments: Pilot injection, Post injection & Main injection [40][41].

4. Post Combustion Techniques

4.1 Diesel Particulate Filters (DPF)

A lot of work has been reported on this topic since 1980. DPF is widely used technology to control DPM from diesel engine. There are many types of DPF are under investigation depending upon porous media like ceramic fiber and ceramic monoliths, alumina coated mesh, and honey comb mesh are widely studied mediums. Geometry of mesh cells is another widely studied dimension in the public literature. It may be squared, honey comb shape, hexagonal, octagonal or any other shape. K. Tsuneyoshi and K. Yamamoto [42] for example studied hexagonal and square cell geometry and concluded that hexagonal geometry is far more efficient than conventional geometry. Studies have reported that they can be 99% efficient depending upon suitable selection of different parameters for the filter. [43]

On the other side, many factors have been found that badly affected the efficiency of DPF. For example, K. Yamamoto et al. studied the effect of soot deposition on the efficiency of DPF with different porosity and length. They reported increase in back pressure with increasing concentration of soot formation [44]. Ceramic wall-based filters are another type of filter widely investigated in the public literature. They use alternate cells that are plugged at one end and the other end is open. Exhaust flows downstream through one cell and enters the other cell that ultimately leads it out in the atmosphere as shown in Figure.7

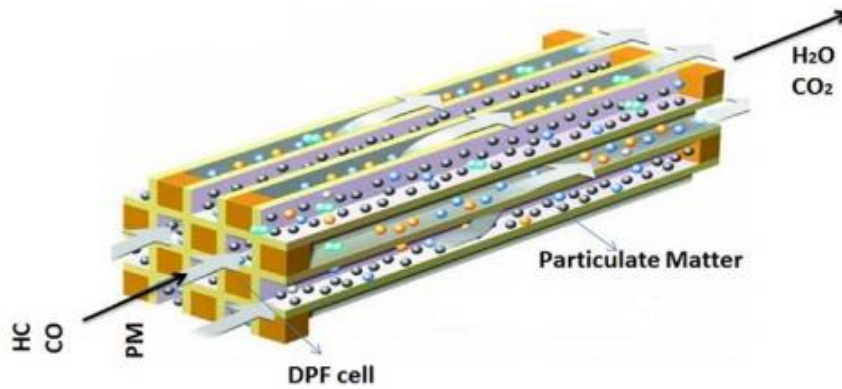


Figure7. Exhaust of diesel Engine flowing through Particulate Filter [10].

4.2 Regeneration

It is not tough to filter exhaust using a fine micro-structured mesh. Exhaust leaves soot particles when it is forced to pass through these micro paths. But these particles may lead to the blockage of these channels. Blockage of these channels reduces the filter efficiency of DPF. Most challenging job is to get these soot particles out of the refine mesh. Regeneration is a technique in which soot particles trapped in the mesh of DPF are oxidized to CO₂ at high temperature and pressure without melting and damaging the mesh itself. There are many categories of regeneration of briefly explained below Figure 8 and their detail is in Table 3.

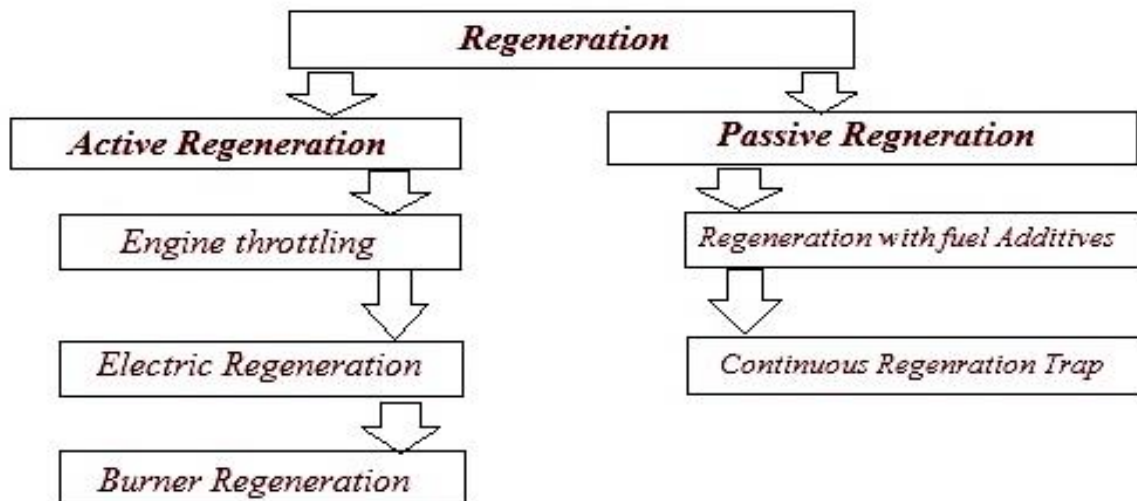


Figure 8. Sub classification of Regeneration [10].

Table 3. Sub Categories of Regeneration technique in Diesel Engine

Active Regeneration			Passive Regeneration	
-Uses sensor technology to oxidize the soot particles -Exhaust temperature is raised above 500K upon receiving the signal from sensor. - Soot particles are ignited and oxidized at high temperature 03 means of temperature increment.			-Catalyst to put on surface of filter -specially designed catalytic oxidation device to enhance soot particle oxidation process -Economic and easy maintenance	
<p><i>Engine Throttling</i></p> <p>-Fuel air ratio is increased while throttling</p> <p><u>Advantage</u></p> <p>Exhaust temperature is enhanced</p> <p><u>Drawback</u></p> <p>-Fuel consumption is increased abruptly</p> <p>-Reduction in air & more fuels lead to CO emissions</p>	<p><i>Burner Regeneration</i></p> <p>uses a burner in front of the filter</p> <p><u>Advantage</u></p> <p>DP blocks the filter leads to increase backpressure sense by sensor</p> <p>ECU on the burner at oxidation occurs at 6500 C and all soot removed</p> <p><u>Drawback</u></p> <p>Malfunctioning of sensor leads to damage of DPF</p>	<p><i>Electric Regeneration</i></p> <p>Same as burner Reg. but uses electrical resistance to heat</p> <p><u>Advantage</u></p> <p>Less cleaning and easy to maintain the system</p>	<p><i>Regeneration by Fuel Additives</i></p> <p>Fuel radicals as Fe, Zn, Cu, and Pb can be used as fuel additives to accelerate</p> <p><u>Advantage</u></p> <p>-Reduces the oxygen temperature of soot. Hence, oxidation occur now at lower temperature.</p> <p>-This is very cheap method for regeneration</p>	<p><i>Continuous Regenerating Trap</i></p> <p>Catalyst is employed on the surface of substrate</p> <p><u>Advantage</u></p> <p>Particulate matter removal due to oxidation at surface</p>

5. Emission of Nitrogen Oxides

Generally, NO_x represents a family of seven compounds. Nitrogen (N₂) is a diatomic molecule & chemically inert gas. Our atmospheric air consists around 79% Nitrogen. At elevated temperatures (approx. around 1500°C and above this temperature) this Nitrogen (N₂) disassociate into its atomic state (N). This atomic Nitrogen (N) is highly reactive in nature and has ionization levels from +1 to +5 valence states. That's why nitrogen can exist in several different oxides like N₂O, NO, N₂O₂, N₂O₃, NO₂, N₂O₅ and N₂O₄ [45].

Environmental protection agency (EPA) regulates critically nitrogen dioxide (NO₂) among its family of compounds. The reason is that it is the most dominant form of NO_x in the troposphere region that is resulted from stationary/automobile or by anthropogenic/human activities in urban areas of lower atmosphere [45]. Figure 9 shows the causes of NO_x generated by activities. Most of NO_x emitted from different sources is found as NO & this, later on, is oxidized in the atmosphere to NO₂ within very short interval of time. It is found that around 10 - 20% of total emission from diesel engines is emitted as NO₂, which is proved approx. five times more toxic and dangerous than NO regarding health. Both NO & NO₂ are collectively termed as NO_x. The other oxides of nitrogen occur in minor quantities and rapidly react to NO and NO₂ in Diesel engine's combustion. EPA has recognized dedicated standards for human and welfare health called as "National Ambient Air Quality Standards (NAAQS)" for NO₂. These standards outline that level of air quality which is mandatory to maintain, with an adequate factor of safety, to care for public health (called as primary standard) and public welfare (termed as secondary standard). For restriction of NO_x emission the primary and secondary standard both defined limit for NO₂ as 0.053 parts per million (ppm) (100 micrograms per cubic annual arithmetic mean concentration[46].

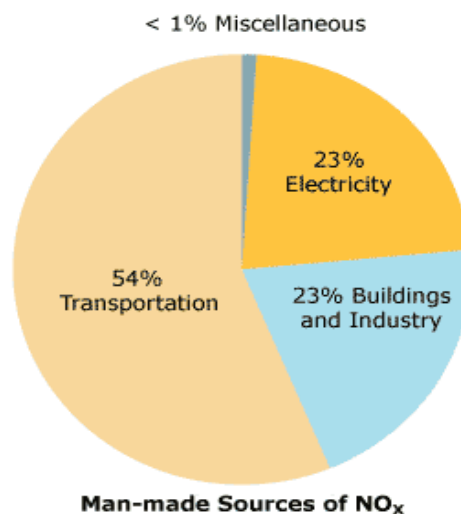


Figure 9. Typical Major sources of NO_x Emission [47].

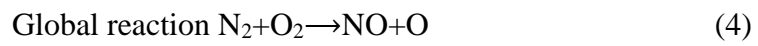
5.1. Sources of Nitrogen Oxides Formation

NO_x can be formed inside the combustion chamber by three mechanisms.[48]

5.1.2 Thermal NO_x

NO_x emission from diesel engine exhaust is mainly considered by formation from Thermal effect. Thermal NO_x is generated during combustion when nitrogen reacts with abundant oxygen at elevated temperature (usually at 1500°C or above). It is formed in exhaust gases behind the flame front. The chemical thermodynamics favor the formation of NO_x generation at high temperature simply by the dissociation of molecular nitrogen and molecular oxygen. The strong covalent triple bond in N₂ molecule require high temperature to break into its atomic form or its radical N₂. NO_x formation is highly depending upon the temperature so its trend formation against various temperature is shown in figure 10.

The chemical Equations can be understood by the Zeldovich mechanisms [49]



5.2. Prompt NO_x

Prompt NO_x forms from molecular nitrogen of atmospheric air when combine with fuel in rich mixture. This nitrogen then oxidizes along with the fuel and becomes NO_x during combustion. It is called prompt NO because it forms quickly as the combustion reaction and it cannot be limited from its generation. Sources of Prompt NO_x are the number of radicals that formed during fuel fragmentation in HC flames e.g. CH, CH₂, and C₂H.[49]

5.3. Fuel NO_x

Fuel NO_x is formed only when there is nitrogen itself in the fuel as a constituent. Fuels containing Nitrogen when burn (e.g., coal) creates fuel NO_x that result from oxidation of the already-ionized nitrogen contained in the fuel. Gas fuels have relatively low amount of nitrogen and thus produced low fuel NO. During combustion, from 10-15% of this nitrogen will react with hydrocarbon radical's CH or CH₃ and will form hydrogen cyanide HCN which will then lead to NO. Therefore, all of nitrogen which is basically the organic nitrogen does not transform to NO. If the mixture contains more fuel i.e. is fuel rich, then environment of combustion chamber becomes reducing one and this tends to push the fuel nitrogen form either N₂ or NH₃. But if the system is lean i.e. excess oxygen so there is oxidizing environment then more NO is formed. Unlike thermal NO_x fuel NO is not very temperature sensitive. In diesel engine mostly hydrocarbon fuel is used so that fuel NO_x is not considered as the formation criteria for NO_x

inside diesel Engine[49]. Variation of all this three NO_x with combustion temperature inside Diesel Engine is shown in Figure 10 and Table 4 highlights the key differences between all NO_x.

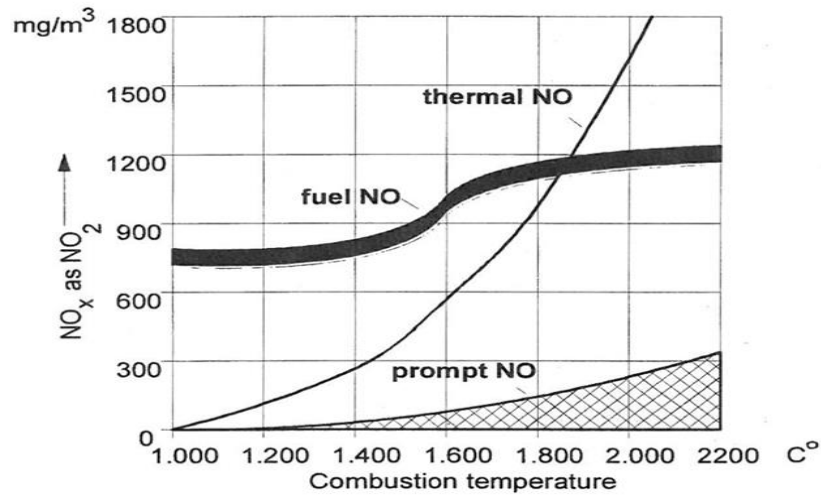


Figure 10. NO_x forming inside a typical Diesel Engine against temperature in combustion zone [47].

Table 4. Main difference between three types of NO_x [50].

Formation mechanism	Description
THERMAL NO _x	Involves the oxidation of the atmospheric nitrogen contained in the fuel oxidant mixture during the high temperature combustion of fossil fuels
PROMPT NO _x	No formed at a rate faster than that from thermal NO due to high speed reactions that occur at flame from reactions of fuel derived radicals (typically CN- groups) with N ₂ . This process is commonly referred as the “fenimore prompt NO” mechanism
FUEL NO _x	Involves the conversion of originally bound nitrogen compounds contained within the fuel (primary coal and heavy oil)

6. Control Techniques of Nitrogen Oxides Emissions

6.1 Pre combustion/Active Control Techniques of NO_x Emission

6.1.1 Injection Timing Control

Injection Timing of fuel greatly effects the formation of NO_x inside the combustion chamber. Figure 11 represent NO_x variation over injection timing. By reducing the timing at which fuel injector injects, peak cylinder pressure can be minimized, which in turn helps to reduce peak cylinder temperature also. As NO_x is temperature dependent So ultimately NO_x reduces.[9]

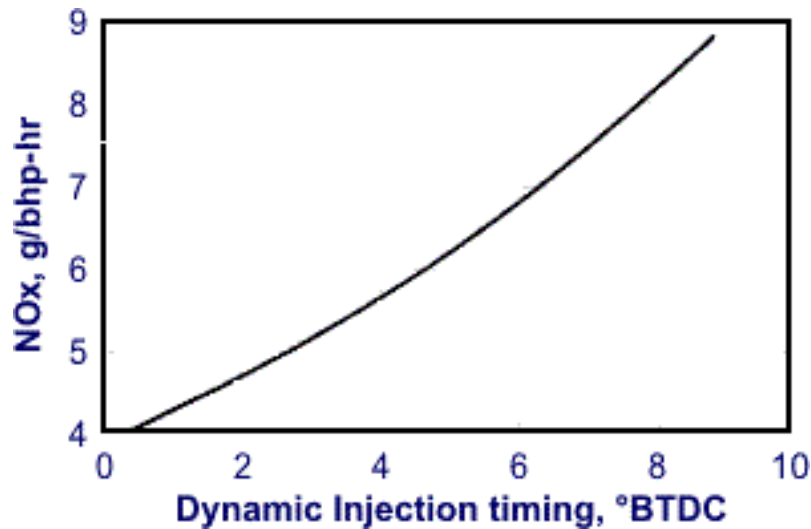


Figure 11. Trend of NOx inside a typical Diesel Engine with injection Timing[9]

6.1.2 Cooling the Intake Air

Unlike injection timing strategy, cooling of air in intake manifold has lower effect. Heat capacity of air increases as its temperature inside the intake manifold decreases by cooling, resulting overall reduction in peak cylinder temperature as well as lower peak temperature. This makes impact the formation of NOx and enables the less production of NOx. Figures 11 show the effect of intake manifold temperature on NOx emission[9].

6.1.3 Exhaust Gas Recirculation

Exhaust gas recirculation, also termed as EGR is one of the prominent techniques that have been employed in diesel engines for reduction of NOx emissions. NOx formation mainly depends upon the temperature of combustion reaction. EGR's working principle favors those conditions which lessen the formation of NOx emission i.e. reduction of peak temperature during combustion reaction by diluting the concentration of oxygen in the combustion charge, increasing the thermal capacity of combustion mixture and dissociation of water molecules in recirculated exhaust by endothermically. [51]

Therefore it is recirculating the small percentage of exhaust gas makes the combustion mixture lean and hence controls the temperature of combustion chamber[52].

6.1.4 Injection of Steam or Water:

Injection of water or steam in the air flow intake of diesel engine is an effective technique to lower the temperature of combustion zone. This can reduce temperature up to 1400 °F thus it lessens the NOx generation. This method is found to reduce NOx emission up to 40ppm. But at the same time the limitation of this method is that it causes the concentration of CO and unburned hydrocarbon at exhaust stream to be increased[3][53].

The injection of water into the intake of air can be done through following methods

- Water fumigation along with intake air
- Dedicated injectors for direct injection of water into the combustion chamber mixture
- Premixing of fuel and water before the injection inside the combustion chamber[54]

It is observed that water injection in any form from above methods such as mixture of water and diesel called diesel emulsion, fumigation or direct injection in to cylinder, diminishes the established flame temperature and lessen thermal NO_x formation. However the application of these methods causes the HC and CO emissions and SFC increment and this depend upon the method of water injection used with load and speed variations of engine[3].

6.2. Post Combustion/ Passive Control Techniques

6.2.1. Catalytic Converter

Catalytic converter is one of the foremost and longstanding techniques used in both commercial as well in automobile diesel engine to reduce the NO_x, CO and other emission before emitting it into atmosphere. Physically it is a metal box whose size depends upon the application of engine. Two connecting pipes are there, one is called input pipe connected to the main hot exhaust manifold and other is connected to the stack or exhaust to emit final into atmosphere. It consists of dense honeycomb structure made of ceramic material with proper coating of catalyst. The honeycomb structure allows gases to pass through greater area so that reaction at the surface takes place efficiently[55].

The exhaust gases from the engine passes over the catalyst, chemical reaction happens on its surface, breaking the pollutant gases and transforming them into other gases that are harmless and can be discharge to atmosphere. One limitation with this kind of simple technique is to avoid the usage of lead containing fuel because lead in conventional fuel deteriorates the catalyst drastically and catalyst fail to take pollutant gases[56]. The chemical reactions inside the converter is shown in table 4.

A simple catalyst converter consists of two kind of catalyst

- Catalyst one serves the purpose of reduction of Nitrogen oxide pollutants. By reduction process, oxygen is removed from NO_x and release Nitrogen in atmosphere which is harmless as ambient air contains 79% nitrogen.
- The other catalyst works exactly the same, but the chemical reaction is opposite to that of the reduction i.e. it works on oxidation process. CO is oxidized to CO₂ by providing the oxygen. In similar fashion unburned Hydrocarbon is converted to carbon dioxide and water and released to atmosphere.

Three different chemical reactions are going one for reduction of nitrogen and other two are oxidation of oxygen and unburned hydrocarbon. This specific type is called three-way catalyzt converters. Figure 12 show three-way catalytic converter for NO_x reduction.

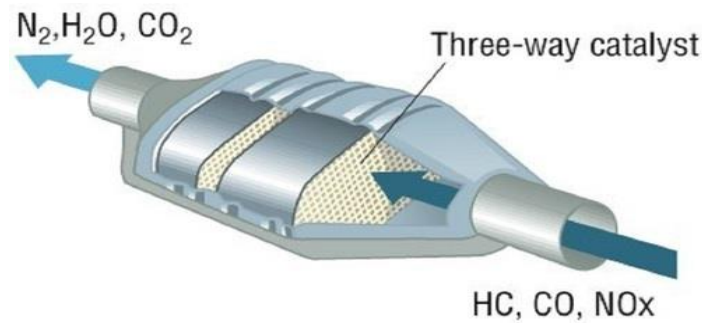


Figure 12. Three-way catalytic converter [47].

Table 5. Chemical reactions inside three-way catalytic converter for removal of NO_x

<u>Reduction of NO_x to N₂</u>	<u>Oxidation of CO to CO₂</u>	<u>oxidation of unburned Hydrocarbon</u>
$2\text{CO} + 2\text{NO} \rightarrow 2\text{CO} + \text{N}_2$	$2\text{CO} + \text{O}_2 \rightarrow 2\text{CO}_2$	$\text{HC} + \text{O}_2 \rightarrow \text{H}_2\text{O} + \text{CO}_2$ [56]
$\text{HC} + \text{NO} \rightarrow \text{CO}_2 + \text{H}_2\text{O} + \text{N}_2.$		
$2\text{H}_2 + 2\text{NO} \rightarrow 2\text{H}_2\text{O} + \text{N}_2$		

6.2.2. NO_x Storage-Reduction Catalysts (NSR)

Most of the diesel engine operates on lean mixture with excess amount of oxygen in its combustion chamber. This condition is not ideal for the catalytic converter because it require both oxidizing and reducing environment. Therefor for large industrial application a different kind of catalyst converter is required that must provide only reducing environment for reduction of NO_x and in this regard NO_x storage reduction catalyst is suitable for large diesel engine The NO_x reduction process completed in two stages: 1- NO_x stored when the engine is running on high air fuel ratio 2- Release along with lessening of NO_x during engine operation when operating conditions are rich.

In this system, a catalyst which is usually platinum, used on metal oxide (Al₂O₃, SiO₂, TiO₂) with doped of BaO on it. Platinum assist the reduction of NO into NO₂ which then gets absorbed in the support as nitrate[9]. Figure 13a represent the simple pictorial view of mechanism of NSR while reduction and storage.

If fuel air mixture is rich in nature, these nitrates get release from the same support and converted to N₂ in the presence of hydrocarbons, that serves to provide a reducing environment. This transformation is quite tough at either very low load engine or at very high load operations due to inadequate HC emission and catalyst remains inactive. There is a limit of exhaust temperature at which NO_x conversion efficient has its maximum value. it is solely depending upon HC/NO_x ratio. Higher will be the HC/NO_x ratio, higher will be the value of

temperature at which maximum NO_x conversion occurs. Figure 13b shows the effect of HC/NO_x ratio on the value of optimum temperature for maximum NO_x conversion[57]. There is also limitation of this system like catalytic converter. Here that fuel should be used which have low sulfur content because NSR becomes deactivated as sulfur content passes over it [9].

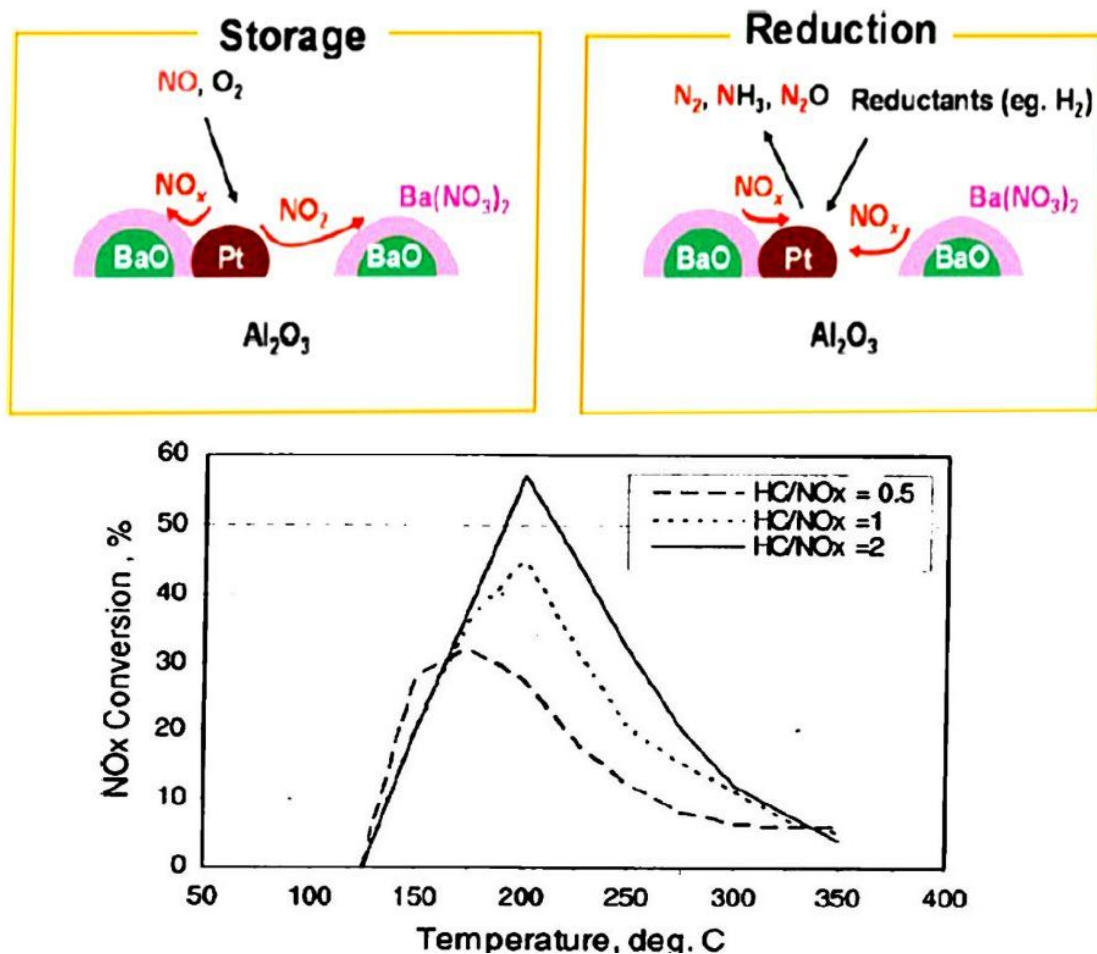


Figure 13. a) Storage of NO_x & reduction during engine operation [47], b) NO_x conversion Efficiency at combustion temperature at various ratios of Hydrocarbon [9]

6.2.3. Selective Catalyst Reduction

This technique utilizes ammonia for producing the reduction environment of NO_x. Urea is the source of ammonia in this method with 30-40% concentration in water.

Figure 14 represents arrangement of SCR system. SCR system is ceramic honeycomb substrate with catalytic coating of mixture of vanadium, tungsten, and titanium oxide. There are 03 sections in this reduction technique: hydrolysis catalyst section, SCR catalyst section, and oxidation catalyst section. Urea is injected at upside of SCR system and per concentration of NO_x. Urea breaks in the first step i.e. hydrolysis and produce ammonia. Ammonia comes into SCR catalyst and reduces NO_x into harmless gas N₂ [9],[58].

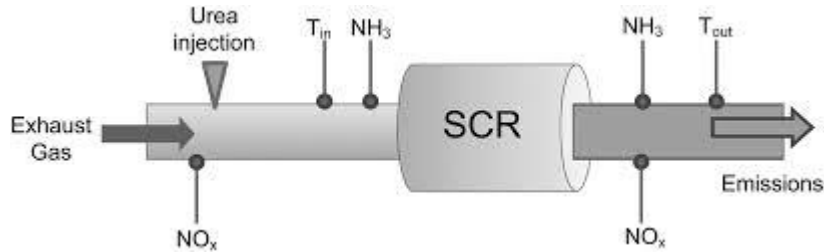


Figure 14. Selective Catalyst Reduction [47].

6.2.4. Non-Thermal Plasma

It is technique that control NO_x after it has been produced in combustion engine. Non thermal Plasma is basically the ionized gas not produced from the heat but produced by the four techniques Dielectric Barrier Discharge (DBD), Corona Discharge (CD), Electron Beam Generated Plasma (EBGP) and Microwave Plasma (MP). It simply ionizes the reducing agents that injected the in-flue gases that react with NO_x and reduced them. It is beneficial because it does not increase the flue gases temperature because it is non-thermal[59][60].

6.2.5. Charge Dilution Method

Diluting the intake mixture of diesel engine proved successful in reduction of NO_x in diesel engine. Diluting the charge reduces the flame temperature which reduced the NO_x generation. Gases such as N₂, CO₂, or inert gases if circulated with mixture charge are found successful in NO_x reduction at wide range of operating conditions in diesel engines Figure 15a depicts the effect of different gases in dilution of intake charge and its temperature. CO₂ has found as one of the effective diluents in NO_x reductions. Around with 6% CO₂ admission NO_x emission reduce approximately by 50%. However, with the application of this technique, smoke emission found to be higher around 60% and CO emission also increased approximately by 8.5 times in comparison without the charge diluted. In addition to this, engine efficiency parameters alike torque, power, BMEP and SFC have deteriorated approximately 5.9%, 5.5%, 6%, 3.3% respectively form the value which obtained when there is no charge dilution[3].

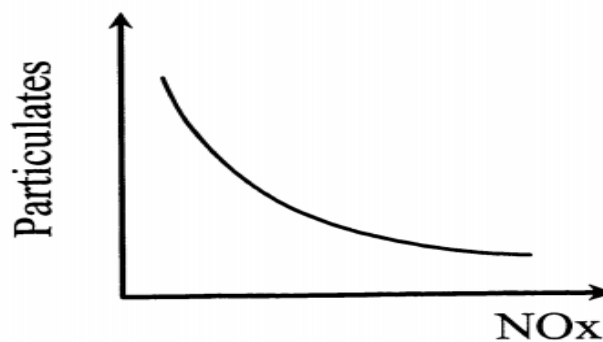


Figure 15. Trade of between DPM and NO_x in reduction techniques

7. Discussion Section

Two broad categories are there for emission control of NO_x and DPM. Pre combustion techniques mostly focused on parametric control of intake charge such as air and fuel for controlled combustion in chamber. While post combustion techniques generally employed catalyst and other methods for promoting the chemical reaction that inhibit the pollutants level into atmosphere. Among three mechanism of NO_x formation, thermal NO_x is the dominant one in diesel engine and major source of harmful radical in environment. High temperature in Diesel engine (because of greater compression ratio) is the main cause of NO_x formation during combustion while on the other hand DPM emission mostly occur due to rich mixture in combustion zone. The thorough review of control techniques depicts that these two emissions i.e. NO_x and DPM are at the two-extreme end in term of controlling method. The employment of any technique for controlling one emission leads to some higher percentage of other emission due to parametric control of temperature and combustion zone mixture. Hence there is a general trade off exist between these two emissions and can be seen by general graph of figure 15b. Reduction in one emission produces a greater percentage of another pollutant in exhaust on practical ground applications, selection of any technique merely depends upon its feasibility and type of diesel engine for which it is to be employed.

8. Conclusion

Diesel Engines have been widely used from the earliest 21st century as power source in marine, automobile and in industrial applications. With their usage, different emissions resulting from exhaust of diesel engine had become the source of environmental pollutions and severe threat for global environmental regulations. Most of the emission are result from impurities present in the intake fuel and chemical reactions taking place at high temperature inside the chamber. Among all emissions of diesel engine NO_x and DPM are found acute ones from prepositive of human health and environmental policies. With technological advancement and time lots of research work has been performed to reduces these two emissions either before the combustion zone or after the combustion keeping the engine efficiency at optimum. Hence in this paper a comprehensive review is made on NO_x and DPM emission covering their formation and types along with emphasizing on pre and post combustion reduction techniques. Employment of each method and their Resulting effect is described in detail with their advantages and limitations. With these techniques there is an inverse relation of PM and NO_x emission. If one technique reduces NO_x then PM found to be increase and vice versa. There is a tradeoff between NO_x and PM emission. Selection of each technique depend upon the its application and feasibility.

9. References

- [1] K. Shen, F. Li, Z. Zhang, and C. Yin, "Effects of LP and HP cooled EGR on performance and emissions in turbocharged GDI engine," *Appl. Therm. Eng.*, vol. 125, no. x, pp. 746–755, 2017.
- [2] H. Wei, T. Zhu, G. Shu, L. Tan, and Y. Wang, "Gasoline engine exhaust gas recirculation - A review," *Appl. Energy*, vol. 99, no. X, pp. 534–544, 2012.
- [3] G. S. Hebbar, "NO_x from diesel engine emission and control strategies - a review," *Int. J. Mech. Eng. Rob. Res*, vol. 3, no. 4, pp. 471–482, 2014.
- [4] I. A. Reşitoğlu, K. Altinişik, and A. Keskin, "The pollutant emissions from diesel-engine vehicles and exhaust," *Clean Technol. Environ. Policy*, vol. 17, no. 1, pp. 15–27, 2015.
- [5] C. C. X. et al. . Chang Chun Xu et al., "Investigation of ICE to Reduce Exhaust Emission, A Review," *Int. J. Mech. Prod. Eng. Res. Dev.*, vol. 9, no. 3, pp. 395–408, 2019.
- [6] P. Appavu, V. Ramanan M, J. Jayaraman, and H. Venu, "NO_x emission reduction techniques in biodiesel-fuelled CI engine: a review," *Aust. J. Mech. Eng.*, vol. 00, no. 00, pp. 1–11, 2019.
- [7] T. V. Johnson, "Diesel Emission Control Review," *SAE Int. J. Fuels Lubr.*, vol. 2, pp. 1–12, 2009.
- [8] S. R. Engineering, "Study on exhaust emissions & its reduction techniques in engines," 2015.
- [9] P. C. Shukla, T. Gupta, "Techniques to Control Emissions from Diesel Engine," 2018.
- [10] S. Mohankumar and P. Senthilkumar, "Particulate matter formation and its control methodologies for diesel engine: A comprehensive review," *Renew. Sustain. Energy Rev.*, vol. 80, no. June 2016, pp. 1227–1238, 2017.
- [11] H. C. McKee, J. M. Clark, and R. J. Wheeler, "Measurement of diesel engine emissions," *J. Air Pollut. Control Assoc.*, vol. 12, no. 11, pp. 516–546, 1962.
- [12] E. J. Calabrese, G. S. Moore, R. A. Guisti, C. A. Rowan, and E. N. Schulz, "A review of human health effects associated with exposure to diesel fuel exhaust," *Environ. Int.*, vol. 5, no. 4–6, pp. 473–477, 1981.
- [13] C. A. Pope III, R. T. Burnett, M. J. Thun, E. E. Calle, D. Krewski, and G. D. Thurston, "to Fine Particulate Air Pollution," *J. Am. Med. Assoc.*, vol. 287, no. 9, pp. 1132–1141, 2002.
- [14] M. C. Turner, D. Krewski, C. A. Pope, Y. Chen, S. M. Gapstur, and M. J. Thun, "Long-term ambient fine particulate matter air pollution and lung cancer in a large cohort of never-smokers," *Am. J. Respir. Crit. Care Med.*, vol. 184, no. 12, pp. 1374–1381, 2011.
- [15] C. J. Johnston, J. N. Finkelstein, P. Mercer, N. Corson, R. Gelein, and G. Oberdorster, "Pulmonary effects induced by ultrafine PTFE particles," *Toxicol. Appl. Pharmacol.*, vol. 168, no. 3, pp. 208–215, 2000.
- [16] D. W. Dockery, J. Schwartz, and J. D. Spengler, "Air pollution and daily mortality: Associations with particulates and acid aerosols," *Environ. Res.*, vol. 59, no. 2, pp. 362–

373, 1992.

- [17] R. Hauser, E. a Eisen, L. Pothier, and D. C. Christiani, "A prospective study of lung function among boilermaker construction workers exposed to combustion particulates.," *Am. J. Ind. Med.*, vol. 39, no. 5, pp. 454–62, 2001.
- [18] P. S. Gilmour, D. M. Brown, T. G. Lindsay, P. H. Beswick, W. MacNee, and K. Donaldson, "Adverse health effects of PM10 particles: involvement of iron in generation of hydroxyl radical.," *Occup. Environ. Med.*, vol. 53, no. 12, pp. 817–822, 1996.
- [19] S. McDowell and K. Gammon, "Differential gene expression in the initiation and progression of nickel-induced acute lung injury," pp. 1943–1948, 1999
- [20] D. N. Belton and K. C. Taylor, "Automobile Exhaust Emission Control by Catalysts," *Curr. Opin. Solid State Mater. Sci.*, vol. 4, no. 1, pp. 97–102, 1999.
- [21] D. D. Hunter and B. J. Udem, "Identification and substance P content of vagal afferent neurons innervating the epithelium of the guinea pig trachea," *Amer J Respir Crit Care Med*, vol. 159, no. 6, pp. 1943–1948, 1999.
- [22] O. I. Smith, "Fundamentals of soot formation in flames with application to diesel engine particulate emissions," *Prog. Energy Combust. Sci.*, vol. 7, no. 4, pp. 275–291, 1981.
- [23] B. S. Haynes and H. G. Wagner, "Soot Formation," *Prog. Energy Combust. Sci.*, vol. 7, no. 4, pp. 229–273, 1981.
- [24] Ö. L. Gülder, "Effects of oxygen on soot formation in methane, propane, and n-Butane diffusion flames," *Combust. Flame*, vol. 101, no. 3, pp. 302–310, 1995.
- [25] D. B. Olson, J. C. Pickens, and R. J. Gill, "The Effects of Molecular Structure on Soot Formation {II}. Diffusion Flames," *Combust. Flame*, vol. 62, pp. 43–60, 1985.
- [26] H. F. Calcote and D. M. Manos, "Effect of molecular structure on incipient soot formation," *Combust. Flame*, vol. 49, no. 1–3, pp. 289–304, 1983.
- [27] M. Astarita, F. E. Corcione, and B. M. Vaglieco, "Fuel composition effects on particulate formation in a divided chamber diesel system," *Exp. Therm. Fluid Sci.*, vol. 21, no. 1–3, pp. 142–149, 2000.
- [28] L. Zhu, Y. Xiao, C. S. Cheung, C. Guan, and Z. Huang, "Combustion, gaseous and particulate emission of a diesel engine fueled with n-pentanol (C5 alcohol) blended with waste cooking oil biodiesel," *Appl. Therm. Eng.*, vol. 102, pp. 73–79, 2016.
- [29] C. Yao, C. S. Cheung, C. Cheng, Y. Wang, T. L. Chan, and S. C. Lee, "Effect of Diesel/methanol compound combustion on Diesel engine combustion and emissions," *Energy Convers. Manag.*, vol. 49, no. 6, pp. 1696–1704, 2008.
- [30] B. Choi et al., "Effect of diesel fuel blend with n-butanol on the emission of a turbocharged common rail direct injection diesel engine," *Appl. Energy*, vol. 146, pp. 20–28, 2015.
- [31] Z. H. Zhang, K. S. Tsang, C. S. Cheung, T. L. Chan, and C. D. Yao, "Effect of fumigation methanol and ethanol on the gaseous and particulate emissions of a direct-injection diesel engine," *Atmos. Environ.*, vol. 45, no. 11, pp. 2001–2008, 2011.

- [32] D. Hernández, J. J. Fernández, F. Mondragón, & D. López, “Production & utilization performance of glycerol derived additive for engines,” *Fuel*, vol. 92, no. 1, pp. 130–136, 2012.
- [33] Y. Wang, H. Liu, & C. F. F. Lee, “Particulate matter emission characteristics of diesel engines with biodiesel : A review,” *Renew. Sustain. Energy Rev.*, vol. 64, pp. 569–581, 2016.
- [34] M. Yao, H. Wang, Z. Zheng, and Y. Yue, “Experimental study of n-butanol additive and multi-injection on HD diesel engine performance and emissions,” *Fuel*, vol. 89, no. 9, pp. 2191–2201, 2010.
- [35] Y. C. Chang, W. J. Lee, S. L. Lin, and L. C. Wang, “Green energy: Water-containing acetone-butanol-ethanol diesel blends fueled ,” *Appl. Energy*, vol. 109, pp. 182–191, 2013.
- [36] S. L. Lin, W. J. Lee, C. F. F. Lee, and Y. P. Wu, “Reduction in emissions of nitrogen oxides, particulate matter, and polycyclic aromatic hydrocarbon by adding water-containing butanol into a diesel-fueled engine generator,” *Fuel*, vol. 93, pp. 364–372, 2012.
- [37] M. Nadeem, C. Rangkuti, K. Anuar, M. R. U. Haq, I. B. Tan, and S. S. Shah, “Diesel engine performance and emission evaluation using emulsified fuels stabilized by conventional and gemini surfactants,” *Fuel*, vol. 85, no. 14–15, pp. 2111–2119, 2006.
- [38] C. Sayin and M. Canakci, “Effects of injection timing on the engine performance & exhaust emissions of a dual-fuel diesel engine,” *Energy Convers. Manag.*, vol. 50, no. 1, pp. 203–213, 2009.
- [39] P. Ye and A. L. Boehman, “An investigation of the impact of injection strategy and biodiesel on engine NOx and particulate matter emissions with a common-rail turbocharged diesel engine,” *Fuel*, vol. 97, no. x, pp. 476–488, 2012.
- [40] C. Y. Choi and R. D. Reitz, “Experimental study on the effects of oxygenated fuel blends and multiple injection strategies on DI diesel engine emissions,” *Fuel*, vol. 78, no. 11, pp. 1303–1317, 1999.
- [41] Y. Niki, Y. Nitta, H. Sekiguchi, and K. Hirata, “Diesel Fuel Multiple Injection Effects on Emission Characteristics of Diesel Engine Mixed Ammonia Gas Into Intake Air,” *J. Eng. Gas Turbines Power*, vol. 141, no. 6, p. 061020, 2019.
- [42] K. Tsuneyoshi and K. Yamamoto, “A study on the cell structure and the performances of wall-flow diesel particulate filter,” *Energy*, vol. 48, no. 1, pp. 492–499, 2012.
- [43] J. Fang et al., “The effect of operating parameters on regeneration characteristics and particulate emission characteristics of diesel particulate filters,” *Appl. Therm. Eng.*, vol. 148, no. November 2018, pp. 860–867, 2019.
- [44] K. Yamamoto, S. Satake, and H. Yamashita, “Microstructure and particle-laden flow in diesel particulate filter,” *Int. J. Therm. Sci.*, vol. 48, no. 2, pp. 303–307, 2009.
- [45] T. Johnson, “Diesel engine emissions and their control: An overview,” *Platin. Met. Rev.*, vol. 52, no. 1, pp. 23–37, 2008.
- [46] Environmental Protection Agency (EPA), “Nitrogen oxides (NOx), why and how they are controlled,” *Epa-456/F-99-006R*, no. November, p. 48, 1999.

- [47] V. Praveena and M. L. J. Martin, "A review on various after treatment techniques to reduce NO_x emissions in a CI engine," *J. Energy Inst.*, vol. 91, no. 5, pp. 704–720, 2018.
- [48] V. K. Varshney, "Design of an Experimental EGR System for a Two Cylinder Diesel Engine," pp. 1–13, 2000.
- [49] L.-C. Stan and D.-E. Mitu, "Simplified mechanism used to estimate the NO_x emission of Diesel engine," *2nd Int. Conf. Manuf. Eng. Qual. Prod. Syst.*, no. 104, pp. 61–64, 2010.
- [50] C. E. Bowen, "An experimental investigation into the use of exhaust gas recirculation for diesel engine NO_x control." 1998.
- [51] Y. Ma and J. Wang, "Predictive Control for NO_x Emission Reductions in Diesel Engine Vehicle Platoon Application," *IEEE Trans. Veh. Technol.*, vol. 68, no. 7, pp. 1–1, 2019.
- [52] G. H. Abd-Alla, "Using exhaust gas recirculation in internal combustion engines: a review," *Energy Convers. Manag.*, vol. 43, no. 8, pp. 1027–1042, 2002.
- [53] J. Serrano, F. J. Jiménez-Espadafor, A. Lora, L. Modesto-López, A. Gañán-Calvo, and J. López-Serrano, "Experimental analysis of NO_x reduction through water addition and comparison with exhaust gas recycling," *Energy*, vol. 168, no. x, pp. 737–752, 2019.
- [54] G. Zamboni, "Influence of Fuel Injection, Turbocharging and EGR Systems Control on Combustion Parameters in an Automotive Diesel Engine," *Appl. Sci.*, vol. 9, no. 3, p. 484, 2019.
- [55] N. I. Mahyon, T. Li, R. Martinez-Botas, Z. Wu, and K. Li, "A new hollow fibre catalytic converter design for sustainable automotive emissions control," *Catal. Commun.*, vol. 120, no. November 2018, pp. 86–90, 2019.
- [56] C. M. Schär, C. H. Onder, and H. P. Geering, "Control of an SCR catalytic converter system for a mobile heavy-duty application," *IEEE Trans. Control Syst. Technol.*, vol. 14, no. 4, pp. 641–653, 2006.
- [57] S. Walter, L. Ruwisch, U. Göbel, G. Hagen, and R. Moos, "Radio Frequency-Based Determination of the Oxygen and the NO_x Storage Level of NO_x Storage Catalysts," *Top. Catal.*, vol. 62, no. 1–4, pp. 157–163, 2019.
- [58] A. S. Ayodhya, V. T. Lamani, M. Thirumoorthy, and G. N. Kumar, "NO_x reduction studies on a diesel engine operating on waste plastic oil blend using selective catalytic reduction technique," *J. Energy Inst.*, pp. 1–10, 2018.
- [59] N. Manivannan, W. Balachandran, R. Beleca, and M. Abbod, "Non-Thermal Plasma Technology for the Abatement of NO_x and SO_x from the Exhaust of Marine Diesel Engine," *J. Clean Energy Technol.*, vol. 2, no. 3, pp. 233–236, 2014.
- [60] A. B. Oskooei, J. Koohsorkhi, and M. Mehrpooya, "Simulation of plasma-assisted catalytic reduction of NO_x, CO, and HC from diesel engine exhaust with COMSOL," *Chem. Eng. Sci.*, vol. 197, no. x, pp. 135–149, 2019.

Modified Compact Central Finite Difference Schemes For The Simulations Of Wave Equation At Any Wave Number

Hafiz Abdul Wajid

Faculty of Engineering, Islamic University of Madinah, Saudi Arabia

hawajid@iu.edu.sa

and

Hifza Iqbal

Faculty of Science, University of Lahore, Pakistan

iqbalhifza3@gmail.com

Abstract

In this paper, we present modified central finite difference (C.F.D.) schemes for solution of the wave equation. The modified schemes (a) provide highly accurate solutions at nodes of the spatial grid for all time steps; (b) preserve the compact stencil structure as of standard C.F.D. scheme and higher order accuracy is achieved without implementation of new code; (c) offer highly accurate solutions for low as well as high wave numbers without use of fine grid. Finally, in order to display superiority of modified C.F.D. schemes numerical computations and graphs are presented for applications such vibrating string and wave propagations compared with standard C.F.D. schemes.

keyword

Compact Finite Difference Schemes, Numerical dispersion, Numerical dissipation, Wave equation, High wave number, wave propagations, Vibrational analysis

المخططات المدمجة للفروق المنتهية المركزية المعدلة لمحاكاة معادلة الموجة في أي رقم موجة

في هذه الورقة، نقدم مخططات معدلة للفروق المنتهية المركزية (C.F.D) لحل معادلة الموجة. توفر المخططات المعدلة (أ) عقدًا دقيقة للغاية لحل الشبكة المكانية لجميع المراحل الزمنية؛ (ب) الحفاظ على هياكل الاستنسل المدمجة لمعيار C.F.D يتم تحقيق مخطط ودقة ترتيب عالية دون تطبيق رمز جديد؛ (ج) تقديم حلول دقيقة للغاية لأعداد الموجات المنخفضة وكذلك العالية دون استخدام الشبكة الدقيقة. أخيرًا، من أجل إظهار تفوق C.F.D تعديل الرسوم البيانية والحسابات الرقمية يتم تقديمها للتطبيقات مثل انتشار الأحيال والموجات الاهتزازية مقارنة مع معيار مخططات .C.F.D

1 Introduction

In today's era of science and technology, we are all surrounded by waves in the form of microwave oven, cell phones, ultrasound scans and radar systems etc. Sound basics of waves and understanding of their propagating nature can lead to improve life of human existence and can help us for future explorations of both nature and universe around us. However, complex mathematical form of such phenomenon either time independent or dependent poses a challenge to physicists, engineers and mathematicians to find explicit analytical solutions. This is often tedious and in many circumstances even not realistically possible. This invites numerical analysts to step in, and make efforts to make an impossible thing a possible one. Hence, efficient and reliable numerical methods are required to deal with such problems. In history a tremendous work has come forth by many [1, 2, 3, 4, 5, 6, 7, 8]. Unfortunately, by use of these discretization schemes issues known as numerical dispersion and numerical dissipation in wave propagations literature are born.

We now list a few of remarkable contributions regarding time independent form of wave equation for large wave numbers. In [9, 10, 11] compact finite difference schemes were presented for Helmholtz equation. Properties such as convergence and accuracy were discussed in detail. However, Nohoubass, Jevtic and Lee [12] in 1998, introduced a novel representation of the second order central finite difference (C.F.D.) scheme by redefining the usual second order C.F.D. approximation with a central node of $2 \cos(\kappa h) + (\kappa h)^2$ instead of 2. This idea was further extended by Yau and Li [13] where they presented exact construction of non-reflecting boundary condition. In [14], an alternative approach was adopted for the construction of modified central finite difference schemes for simulations of Helmholtz equation at any wave number for uniform grids only using *Bloch wave property*. The idea proposed in [14] was further extended for the construction of modified C.F.D. schemes for adaptive grids [15]. In this work we adopt the approach presented in [14, 15] for time harmonic wave equation and extend this for time dependent wave equation.

The organization of the paper is as follows. In Section 2, we present framework for the construction of modified compact central finite difference schemes. In Section 3, numerical examples are presented and in final section schemes are constructed for two dimensional problem and dispersion analysis is presented.

2 Framework for the construction of modified compact central finite difference schemes

We consider the one dimensional wave equation

$$\frac{\partial^2 u}{\partial x^2} = \frac{1}{c^2} \frac{\partial^2 u}{\partial t^2} \quad u = u(x, t) \text{ and } c > 0 \text{ represents wave speed} \quad (1)$$

in order to motivate the ideas for the construction of modified compact C.F.D. schemes.

2.1 Construction of modified compact explicit C.F.D. scheme

For the construction of exact C.F.D. schemes, we adopt the idea of Nehrass and Li presented in [12] for Helmholtz equation. Here we use this idea for wave equation (1). We replace partial derivatives, $\partial^2 u / \partial x^2$ and $\partial^2 u / \partial t^2$, present in (1), by standard second order C.F.D. approximation such that coefficient of middle node 2 is replaced with α giving

$$\begin{aligned} \frac{\partial^2 u}{\partial x^2} &= \frac{1}{h^2} [u_{m+1}^n - \alpha u_m^n + u_{m-1}^n] + O(h^2), \\ \text{and } \frac{\partial^2 u}{\partial t^2} &= \frac{1}{\ell^2} [u_m^{n+1} - \alpha u_m^n + u_m^{n-1}] + O(\ell^2). \end{aligned}$$

Inserting above approximations in (1) and performing ordinary simplifications, we get

$$u_m^{n+1} = (cr)^2 [u_{m+1}^n + u_{m-1}^n] + \alpha(1 - (cr)^2)u_m^n - u_m^{n-1} + O(h^2) + O(\ell^2) \quad (2)$$

with $r = \ell/h$. The unknown α in (2) was termed as dispersion reducing parameter in [12]. A solution of the form $u_m^n = e^{i(m\kappa h - n\omega\ell)}$, known as plane wave solution when substituted in (2) gives after simplifications

$$[2((cr)^2 \cos(\kappa h) - \cos(\omega\ell)) + \alpha(1 - (cr)^2)]u_m^n = 0$$

where $\kappa, \omega > 0$, are the wave number and frequency respectively. Since $u_m^n \neq 0$, and solving for α , we have

$$\alpha = \frac{2[(cr)^2 \cos(\kappa h) - \cos(\omega\ell)]}{((cr)^2 - 1)}. \quad (3)$$

With this value of α , (2) results into compact explicit C.F.D. scheme given by

$$u_m^{n+1} = (cr)^2 (u_{m-1}^n + u_{m+1}^n) + 2[\cos(\omega\ell) - (cr)^2 \cos(\kappa h)]u_m^n - u_m^{n-1}. \quad (4)$$

Interestingly, (4) can also be constructed using a very powerful tool known as *Bloch wave property* [14] defined by

$$u_{m+j}^n = u_m^n e^{ij\kappa h} \quad \text{and} \quad u_m^{n+\tilde{j}} = u_m^n e^{i\tilde{j}\omega\ell} \quad \forall j, \tilde{j} \in \mathbb{Z} \text{ and } \ell, h > 0 \quad (5)$$

therefore, we have

$$u_{m-1}^n + u_{m+1}^n = 2 \cos(\kappa h)u_m^n \quad \text{and} \quad u_m^{n+1} + u_m^{n-1} = 2 \cos(\omega\ell)u_m^n. \quad (6)$$

Using (6) in standard explicit C.F.D. scheme with 2 as the coefficient of the middle node, we have

$$\begin{aligned} & u_m^{n+1} - (cr)^2 [u_{m-1}^n + u_{m+1}^n] - 2(1 - (cr)^2)u_m^n + u_m^{n-1} \\ & = -2[(1 - (cr)^2) - \cos(\omega\ell) - (cr)^2 \cos(\kappa h)]u_m^n \end{aligned}$$

Rewriting above results into (4) and it is interesting to note that the use of the Bloch wave property provide exactly the same scheme. Moreover, as given in [14] that with the use of Bloch wave property, one can make schemes of any order exact either forward, backward or central for Helmholtz equation. Considering this modification of standard implicit C.F.D. scheme is presented in next section.

2.2 Construction of modified compact implicit C.F.D. scheme

This section is devoted for the construction of modified implicit scheme of (1) by replacing time derivative $\partial^2 u / \partial t^2$ with standard second order C.F.D. approximation whereas spatial derivative $\partial^2 u / \partial x^2$ is replaced with weighted average, such that middle node coefficient 2 is replaced with α given by

$$\frac{\partial^2 u}{\partial t^2} = \frac{1}{\ell^2} [u_m^{n-1} + u_m^{n+1} - 2u_m^n] + O(\ell^2) \quad \text{and}$$

$$\begin{aligned} \frac{\partial^2 u}{\partial x^2} = \frac{1}{4h^2} \left\{ u_{m+1}^{n+1} - \alpha u_m^{n+1} + u_{m-1}^{n+1} + 2(u_{m-1}^n - \alpha u_m^n + u_{m+1}^n) \right. \\ \left. + u_{m+1}^{n-1} - \alpha u_m^{n-1} + u_{m-1}^{n-1} \right\} + O(h^2). \end{aligned}$$

Substitution of above approximations in (1) after simplifications give

$$\begin{aligned} \frac{(cr)^2}{4} \left\{ u_{m+1}^{n+1} - \alpha u_m^{n+1} + u_{m-1}^{n+1} + 2(u_{m-1}^n - \alpha u_m^n + u_{m+1}^n) \right. \\ \left. + u_{m+1}^{n-1} - \alpha u_m^{n-1} + u_{m-1}^{n-1} \right\} = u_m^{n+1} - 2u_m^n + u_m^{n-1}. \quad (7) \end{aligned}$$

Now, using Bloch wave property given in (5) and performing straight forward calculations, equation (7) gives following value of α :

$$\alpha = 2 \cos(\kappa h) + \frac{4}{(cr)^2} \frac{1 - \cos(\omega\ell)}{1 + \cos(\omega\ell)}. \quad (8)$$

Inserting value of α from (8) into (7) gives

$$\begin{aligned}
 & -\frac{(cr)^2}{4} [u_{m-1}^{n+1} + u_{m+1}^{n+1}] = \frac{(cr)^2}{2} [u_{m-1}^n + u_{m+1}^n] + \frac{(cr)^2}{4} [u_{m+1}^{n-1} + u_{m-1}^{n-1}] \\
 & - \left[1 + \frac{(cr)^2}{2} \cos(\kappa h) - \frac{\cos(\omega\ell) - 1}{\cos(\omega\ell) + 1} \right] u_m^{n+1} + \left[2 - (cr)^2 \cos(\kappa h) - 2 \frac{\cos(\omega\ell) - 1}{\cos(\omega\ell) + 1} \right] u_m^n \\
 & - \left[1 + \frac{(cr)^2}{2} \cos(\kappa h) - \frac{\cos(\omega\ell) - 1}{\cos(\omega\ell) + 1} \right] u_m^{n-1} \quad (9)
 \end{aligned}$$

which is the required form of modified compact implicit C.F.D. scheme.

2.3 Combined form of modified compact explicit and implicit C.F.D. schemes

We now present combined form of both modified explicit and implicit schemes obtained in (4) and (9) by introducing parameter β given by

$$\begin{aligned}
 & \left\{ 1 + \beta \left(2(cr)^2 \cos(\kappa h) + 4 \left[\frac{1 - \cos(\omega\ell)}{1 + \cos(\omega\ell)} \right] \right) \right\} u_m^{n+1} - (cr)^2 \beta (u_{m-1}^{n+1} + u_{m+1}^{n+1}) + \\
 & = (cr)^2 (1 - 2\beta) u_{m-1}^n + \left\{ 8\beta + 2(3\beta - 1)(cr)^2 \cos(\kappa h) + 2(1 - 4\beta) \cos(\omega\ell) \right. \\
 & \left. + 8\beta \left[\frac{\cos(\omega\ell) - 1}{\cos(\omega\ell) + 1} \right] \right\} u_m^n - (cr)^2 (-1 + 2\beta) u_{m+1}^n + (cr)^2 \beta (u_{m-1}^{n-1} + u_{m+1}^{n-1}) \\
 & - \left\{ 1 + \beta \left(2(cr)^2 \cos(\kappa h) + 4 \left[\frac{1 - \cos(\omega\ell)}{1 + \cos(\omega\ell)} \right] \right) \right\} u_m^{n-1}. \quad (10)
 \end{aligned}$$

Choosing $\beta = 0$ in (10), results into (4) whilst for $\beta = 1/4$, (10) reduces to (9).

Interestingly, series expansions of $\cos(\omega\ell)$ and $\cos(\kappa h)$ present in (10) in terms of $\omega\ell$ and κh results into combined representation of standard explicit and implicit schemes obtained in [16] when $\omega\ell \rightarrow 0$ and $\kappa h \rightarrow 0$ given below

$$\begin{aligned}
 & -(cr)^2 \beta (u_{m+1}^{n+1} + u_{m-1}^{n+1}) + (1 + 2(cr)^2 \beta) u_m^{n+1} = 2(1 + (cr)^2 (2\beta - 1)) u_m^n \\
 & + (cr)^2 (1 - 2\beta) [u_{m-1}^n + u_{m+1}^n] + (cr)^2 \beta [u_{m+1}^{n-1} + u_{m-1}^{n-1}] - (1 + 2(cr)^2 \beta) u_m^{n-1}. \quad (11)
 \end{aligned}$$

This is an attractive feature of modified scheme and is consistent with the requirement of not using finer mesh size especially when simulations are required for high wave numbers.

2.4 Numerical Dispersion of Modified and Standard Schemes: A Comparison

Now to present dispersion analysis of modified compact explicit and implicit C.F.D. schemes, we substitute a plane wave solution of the form $u_m^n = e^{i(m\tilde{\kappa}h - \omega n\ell)}$ in combined form (10) and obtain after straight forward manipulations

$$(cr)^2[\cos(\tilde{\kappa}h) - \cos(\kappa h)]u_m^n = 0$$

where $\tilde{\kappa}$ is known as the discrete wave number. For a non-trivial solution $u_m^n \neq 0$ above equation implies

$$\tilde{\kappa} = \kappa.$$

Therefore the modified schemes (10), do not suffer from issues such as numerical dispersion and dissipation contrary to standard schemes (11) as reported in [14, 16].

3 Numerical Examples

We now test performance of modified schemes by solving problems such as a vibrating string and propagation of wave from left to right in following sections.

3.1 A vibrating string problem

Consider one dimensional wave equation

$$\frac{\partial^2 u}{\partial t^2} = \frac{\partial^2 u}{\partial x^2}, \quad x \in (0, 1) \text{ and } t > 0 \quad (12)$$

with boundary conditions,

$$u(0, t) = u(1, t) = 0 \quad t > 0 \quad (13)$$

and initial conditions

$$u(x, 0) = \sin(\pi x) \text{ and } \frac{\partial u(x, 0)}{\partial t} = u_t(x, 0) = 0 \quad x \in [0, 1]. \quad (14)$$

This problem has an exact solution [16] given by

$$u(x, t) = \sin(\pi x) \cos(\pi t). \quad (15)$$

This problem describes a string tied at both ends vibrating up and down with $\sin(\pi x)$ as initial displacement and zero initial velocity. Initial and boundary conditions are chosen such that continuity

between them is preserved with $c^2 = 1$ as speed of the medium. Spatial $(0, 1)$ and time $t \geq 0$ domains are discretized into N subintervals of length $h = 1/N$ and length ℓ respectively. This means each node is represented by coordinates of the form: $(x_m, t_n) = (mh, n\ell)$ for $m = 0, 1, 2, \dots, N$ and $n = 0, 1, 2, \dots$. Moreover, for this problem error is defined by $Z_m^n = |u_m^n - \tilde{U}_m^n|$ [16] with u_m^n and \tilde{U}_m^n as exact and numerical solutions respectively. For time $t = 1$ highest value of the error is picked for spatial range $x \in (0, 1)$.

3.2 Combined form of standard and modified C.F.D. schemes

First of all, we give combined form of standard and modified C.F.D. schemes given for $c = 1$

$$\begin{aligned} & -r^2\beta(u_{m+1}^{n+1} + u_{m-1}^{n+1}) + (1 + 2r^2\beta)u_m^{n+1} \\ & = 2(1 + 2r^2\beta - r^2)u_m^n + r^2(1 - 2\beta)[u_{m-1}^n + u_{m+1}^n] \\ & \quad + r^2\beta[u_{m+1}^{n-1} + u_{m-1}^{n-1}] - (1 + 2r^2\beta)u_m^{n-1} \end{aligned} \quad (16)$$

and

$$\begin{aligned} & \left\{ 1 + \beta \left(2r^2 \cos(h\pi) + 4 \left[\frac{1 - \cos(\ell\pi)}{1 + \cos(\ell\pi)} \right] \right) \right\} u_m^{n+1} - r^2\beta(u_{m-1}^{n+1} + u_{m+1}^{n+1}) \\ & = r^2(1 - 2\beta)[u_{m-1}^n + u_{m+1}^n] + \left\{ 8\beta + 2(-1 + 3\beta)r^2 \cos(h\pi) \right. \\ & \quad \left. + 2(1 - 4\beta) \cos(\ell\pi) + 8\beta \left(\frac{\cos(\ell\pi) - 1}{\cos(\ell\pi) + 1} \right) \right\} u_m^n \\ & \quad + r^2\beta(u_{m-1}^{n-1} + u_{m+1}^{n-1}) - \left\{ 1 + \beta \left(2r^2 \cos(h\pi) + 4 \left[\frac{1 - \cos(\ell\pi)}{1 + \cos(\ell\pi)} \right] \right) \right\} u_m^{n-1}. \end{aligned} \quad (17)$$

Above schemes are valid for all internal nodes of the spatial grid and for boundary nodes solution is already known as Dirichlet boundary conditions are chosen. Also, above schemes result into standard explicit and standard implicit forms for $\beta = 0$ and $\beta = 1/4$ respectively.

3.3 Solution at first time step for standard and modified schemes

We now consider initial velocity given in (14), that is

$$u_t(x, 0) = 0.$$

and replacing time derivative by second order C.F.D. approximation gives

$$\frac{1}{2\ell} (u_m^{n+1} - u_m^{n-1}) = 0 \Rightarrow u_m^{n-1} = u_m^{n+1}. \quad (18)$$

Inserting (18) into (16) and (17), we obtain desired schemes for initial time step for standard

$$\begin{aligned} & -r^2\beta(u_{m+1}^{n+1} + u_{m-1}^{n+1}) + 2(1 + 2r^2\beta)u_m^{n+1} \\ & = 2(1 + 2r^2\beta - r^2)u_m^n + r^2(1 - 2\beta)[u_{m-1}^n + u_{m+1}^n] \\ & \quad + r^2\beta[u_{m+1}^{n-1} + u_{m-1}^{n-1}] \end{aligned}$$

and modified scheme

$$\begin{aligned} & 2 \left\{ 1 + \beta \left(2r^2 \cos(h\pi) + 4 \left[\frac{1 - \cos(\ell\pi)}{1 + \cos(\ell\pi)} \right] \right) \right\} u_m^{n+1} - r^2\beta(u_{m-1}^{n+1} + u_{m+1}^{n+1}) \\ & = r^2(1 - 2\beta)[u_{m-1}^n + u_{m+1}^n] + \left\{ 8\beta + 2(-1 + 3\beta)r^2 \cos(h\pi) \right. \\ & \quad \left. + 2(1 - 4\beta) \cos(\ell\pi) + 8\beta \left(\frac{\cos(\ell\pi) - 1}{\cos(\ell\pi) + 1} \right) \right\} u_m^n + r^2\beta(u_{m-1}^{n-1} + u_{m+1}^{n-1}) \\ & \quad - 2 \sin(\ell\pi) \sin(\pi x) \sin(\pi t) \left\{ 1 + \beta \left(2r^2 \cos(h\pi) + 4 \left[\frac{1 - \cos(\ell\pi)}{1 + \cos(\ell\pi)} \right] \right) \right\}. \end{aligned}$$

3.4 Analysis of vibrating string problem for all schemes

Table 1: Errors analysis for vibrating string problem with standard and modified explicit schemes

Scheme	One Vibrating Mode		Seven Vibrating Modes	
	Standard	Modified	Standard	Modified
r=0.25	$0.73 * 10^{-4}$	$1.99 * 10^{-15}$	1.6328	$8.88 * 10^{-16}$
r=0.5	$0.47 * 10^{-4}$	$2.22 * 10^{-16}$	1.9286	$6.66 * 10^{-16}$
r=1	0	0	0	0
r=2	$0.82 * 10^{-3}$	$1.33 * 10^{-13}$	67163	$4.49 * 10^{-12}$
r=5	$0.99 * 10^{-1}$	$8.43 * 10^{-14}$	2994.5	$5.16 * 10^{-14}$

Comparison of results obtained with standard and modified C.F.D explicit schemes in case of single as well as seven vibrating modes are given in Table 1 for constant value of $h = 0.1$

Table 2: Errors analysis for vibrating string problem with standard and modified implicit schemes

Scheme	One Vibrating Mode		Seven Vibrating Modes	
	Standard	Modified	Standard	Modified
r=0.25	$0.10 * 10^{-3}$	$2.99 * 10^{-15}$	1.24764	$1.8 * 10^{-12}$
r=0.5	$0.18 * 10^{-3}$	$1.33 * 10^{-15}$	0.49350	$5.42 * 10^{-12}$
r=1	$0.72 * 10^{-3}$	0	0.59156	$6.1 * 10^{-13}$
r=2	$0.59 * 10^{-2}$	$2.22 * 10^{-16}$	0.53966	$2.13 * 10^{-12}$
r=5	0.116021	$2.22 * 10^{-16}$	1.561386	$9.2 * 10^{-11}$

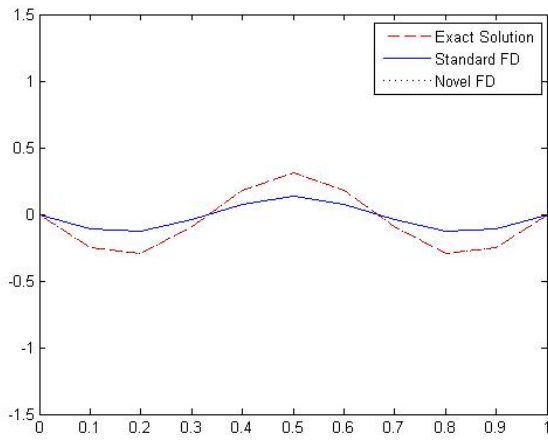
and varying values of $r = 0.25, 0.5, 1, 2, 5$, with temporal step sizes $l = 0.025, 0.05, 0.1, 0.2, 0.5$ respectively.

It is evident from Table 1 that highly accurate results are obtained with modified schemes compared with standard schemes even with increasing values of r for either one or seven vibrating modes. Interestingly, standard scheme performed good for lower values of $r = 0.25, 0.5$ and also for $r = 2$ for only one vibrating mode case. However, standard scheme fails to provide accurate results in case of increasing i.e. seven vibrating modes. Therefore, increasing vibrations worsen dispersive and dissipative behaviour in case of standard schemes whereas modified schemes still provides highly accurate results even for large value of $r = 5$. Practical applications require to choose very small values of r in case of standard schemes which adds to prohibitive computational cost to achieve certain level of accuracy. On contrary, modified schemes offers highly promising results even for $r = 5$

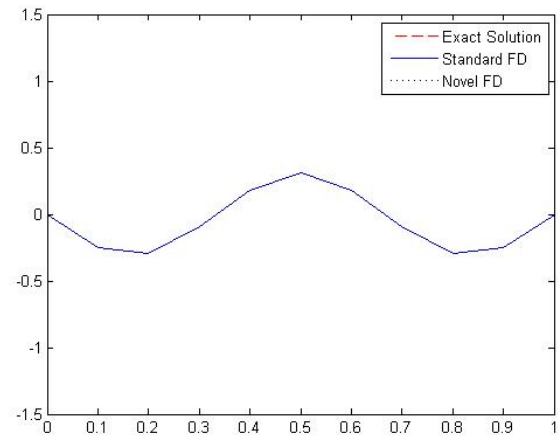
For $r = 1$, which is known as magical number [16, 17], both standard and modified explicit schemes provide dispersion less results with zero error which is a proven characteristic of explicit scheme [16, 17]. Explicit modified scheme constructed also fulfils this characteristic. Standard implicit scheme does not fulfil this characteristic as is evident from Table 2, however modified scheme results into dispersion and dissipation free results for single vibrating mode. Whilst for seven vibrating modes implicit schemes provides highly accurate results. In general modified scheme out performs compared to standard scheme (see Tables 1 and 2).

In Figure 1 dispersion error behaviour is shown for three modes of vibrating string using all schemes. Dispersion is prominent for standard explicit and implicit schemes where as modified schemes are perfect interpolate exact solution (see Figure 1 (a),(c) and (d)). Also, dispersion free behaviour is evident in case of magical number i.e. $r = 1$ for both standard and modified explicit schemes (see Figure 1 (b)). However, dispersion is prominent in case of standard implicit scheme

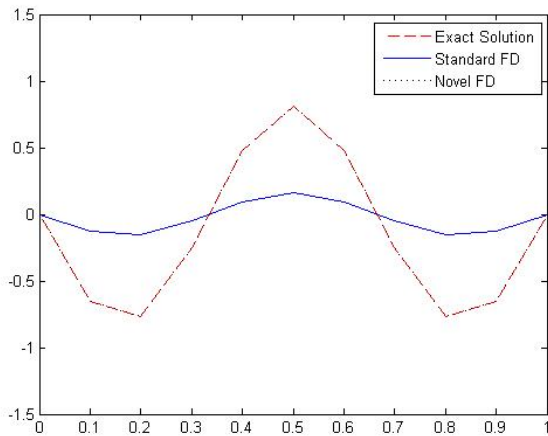
in contrast to the modified implicit scheme which is almost dispersion less (see Figure 1 (d)). Same findings were reported in [6, 7] in case of problems with highly oscillatory nature.



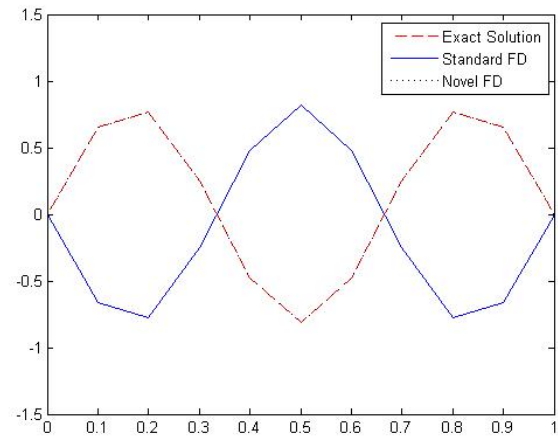
(a) Explicit schemes with $r = 4$



(b) Explicit schemes with $r = 1$



(c) Implicit schemes with $r = 5$



(d) Implicit schemes with $r = 1$

Figure 1: Behaviour of all schemes for three vibrating modes.

3.5 A travelling wave from left to right

We now solve (1) with boundary conditions,

$$u(0,t) = e^{i\kappa x} \text{ and } u_x(1,t) + u_t(1,t) = 0 \quad t > 0 \quad (19)$$

and initial conditions

$$u(x,0) = e^{i\kappa x} \text{ and } u_t(x,0) = -i\kappa e^{i\kappa x} \quad 0 \leq x \leq 1. \quad (20)$$

The exact solution of this problem is

$$u(x,t) = e^{i\kappa(x-t)}. \quad (21)$$

Above example models a wave travelling from left to right with $-i\kappa e^{i\kappa x}$ initial velocity and medium speed is taken as $c^2 = 1$. Also, same configurations for grid are used as were used in model problem one. For this problem discrete l_∞ norm, defined as [16]

$$E_\infty = \max_{m=1,2,\dots,N} \max_{n=1,2,\dots} |u_m^n - \tilde{U}_m^n|.$$

is considered. Furthermore, for this problem only standard explicit scheme and its modified version is considered as one can construct modified implicit scheme following similar steps.

3.5.1 Standard explicit C.F.D scheme of second order for travelling wave problem

In order to avoid repetitions, we obtain the desired scheme by choosing $\beta = 0$ into (16)

$$u_m^{n+1} = r^2(u_{m-1}^n + u_{m+1}^n) + 2(1-r^2)u_m^n - u_m^{n-1} \quad (22)$$

with $r = \ell/h$. We can apply scheme (22) only at interior nodes of the grid as using this at right end node i.e. (Nth node) gives fictitious node. Fictitious nodes also known as phantom nodes and always lie outside the boundary. As solution is not known at this node and consequently removal of this node is required which is considered in next section.

3.5.2 Solution at right end node for standard scheme

Consider non-reflecting boundary condition given by

$$u_x(x,t) + u_t(x,t) = 0. \quad (23)$$

Replacing derivatives in (23) by C.F.D. approximation of second order given below

$$u_x = \frac{1}{2h} [u_{m-1}^n - u_{m+1}^n] + O(h^2) \text{ and } u_t = \frac{1}{2\ell} [u_m^{n-1} + u_m^{n+1}] + O(\ell^2)$$

gives after simplifications and rearranging

$$u_m^{n+1} = u_{m-1}^n - \frac{u_m^{n-1} - u_m^{n+1}}{r}.$$

Now, inserting above value of u_m^{n+1} in (22), and performing simplifications gives

$$u_m^{n+1} = 2(1-r)u_m^n + \frac{2r^2}{1+r}u_{m-1}^n - \frac{1-r}{1+r}u_m^{n-1}.$$

3.5.3 Solution for first time step for standard scheme

We consider initial velocity given by

$$u_t = -i\kappa u_m^n. \quad (24)$$

Replacing temporal derivative with second order C.F.D. approximation leads to

$$u_m^{n-1} = u_m^{n+1} + 2i\ell\kappa u(x, t). \quad (25)$$

Substituting (25) in (22), we obtain scheme given below to calculate solution value at initial time step

$$u_m^{n+1} = (1-r^2 - i\ell\kappa)u_m^n + \frac{r^2}{2}(u_{m-1}^n + u_{m+1}^n).$$

3.5.4 Modified compact explicit C.F.D. scheme for travelling wave problem

For wave propagation problem, the modified compact explicit C.F.D. scheme has following form:

$$u_m^{n+1} = r^2[u_{m-1}^n + u_{m+1}^n] - u_m^{n-1} - 2[r^2 \cos(\kappa h) - \cos(\ell\kappa)]u_m^n \quad (26)$$

which can only be used at internal nodes, and therefore for solution at right end node, we have next section.

3.5.5 Solution at right end node for modified scheme

For solution at right end node, we give

$$u_m^{n+1} = u_{m-1}^n + 2i(\sin(\kappa h) - \sin(\ell\kappa))u_m^n + u_m^{n-1} - u_m^{n+1}$$

which when inserted into (26) and after simplifications gives

$$u_m^{n+1} = \frac{2}{(1+r^2)} [\cos(\ell\kappa) + ir^2 \sin(\kappa h) - ir^2 \sin(\ell\kappa) - r^2 \cos(\kappa h)] u_m^n + \left(\frac{2r^2}{1+r^2}\right) u_{m-1}^n - \left(\frac{1-r^2}{1+r^2}\right) u_m^{n-1}.$$

3.5.6 Solution for first time step for modified scheme

Now using exact form of (24) given by

$$u_m^{n+1} = u_m^{n+1} + 2i \sin(\ell \kappa) u_m^n$$

in (26) provides scheme for initial time step

$$u_m^{n+1} = \frac{r^2}{2} [u_{m+1}^n + u_{m-1}^n] - [r^2 \cos(\kappa h) + i \sin(\ell \kappa) - \cos(\ell \kappa)] u_m^n.$$

Table 3: Error analysis for wave propagation problem for standard explicit scheme

κ	(a) $r = 0.05, h = 1$	(b) $r = 0.5, h = 0.1$	(c) $r = 1, h = 0.01$
10^{10}	$6.21 * 10^{10}$	$1.27 * 10^{10}$	$1 * 10^{10}$
10^8	$7.35 * 10^8$	$2.16 * 10^7$	$9.99 * 10^7$
10^6	$9.03 * 10^6$	$1.97 * 10^5$	$9.99 * 10^5$
10^4	$3.85 * 10^4$	$9.98 * 10^3$	$9.99 * 10^3$
10^2	$6.95 * 10^2$	$2.89 * 10^1$	$1 * 10^2$
10^0	1.8158	0.7005	0.9999
10^{-2}	$4.5 * 10^{-3}$	$7.06 * 10^{-3}$	$1 * 10^{-2}$
10^{-4}	$4.52 * 10^{-5}$	$7.06 * 10^{-5}$	$9.99 * 10^{-5}$

3.5.7 Analysis of second problem: A travelling wave with standard and modified explicit schemes

Results obtained for three different combinations (a) $r = 0.05, h = 1$, (b) $r = 0.5, h = 0.1$, and (c) $r = 1, h = 0.01$ with standard and modified explicit schemes are given with varying range of wave numbers κ in Table (3) and Table (4) respectively. It is evident that for high value of wave number such as $\kappa = 10^8, \kappa = 10^9$ or $\kappa = 10^{10}$, modified schemes provide highly accurate results as error stays less than 10^{-5} for all combinations (see Table (4)). However, results obtained using standard scheme are highly erroneous for large values of wave numbers but for very very small values of wave numbers, i.e. when $\kappa h < 1$ reliable results can be seen from Table (3).

Table 4: Errors analysis for wave propagation problem for modified explicit scheme

κ	(a) $r = 0.05, h=1$	(b) $r = 0.5, h=0.1$	(c) $r = 1, h=0.01$
10^{10}	$3.55 * 10^{-5}$	$6.28 * 10^{-3}$	$6.66 * 10^{-5}$
10^8	$3.42 * 10^{-7}$	$2.22 * 10^{-7}$	$6.51 * 10^{-7}$
10^6	$3.51 * 10^{-9}$	$1.98 * 10^{-9}$	$6.67 * 10^{-9}$
10^4	$3.50 * 10^{-11}$	$2.32 * 10^{-9}$	$6.71 * 10^{-11}$
10^2	$3.90 * 10^{-13}$	$1.72 * 10^{-13}$	$6.49 * 10^{-13}$
10^0	$1.95 * 10^{-11}$	$2.37 * 10^{-14}$	$7.72 * 10^{-15}$
10^{-2}	$9.9 * 10^{-12}$	$2.62 * 10^{-14}$	$6.49 * 10^{-17}$
10^{-4}	$2.02 * 10^{-11}$	$5.32 * 10^{-15}$	$0.78 * 10^{-19}$

For further analysis in Figure 2 results are shown and it is found that wave obtained using standard scheme shows:

- dispersion (phase lag is evident) for moderate values of wave numbers (Figure 2 (a)–(b));
- erroneous results for wave number to 50 (Figure 2 (c));
- dissipated wave when wave number is 100 (Figure 2 (d));
- On the other hand wave obtained using modified scheme gives nodally exact solutions for all values of wave numbers.

4 Modified Compact Explicit and Implicit Schemes for Two dimensional Case

Consider the two dimensional wave equation given by

$$\frac{\partial^2 u}{\partial x^2} + \frac{\partial^2 u}{\partial y^2} = \frac{1}{c^2} \frac{\partial^2 u}{\partial t^2} \quad (x, y) \in (a, b) \text{ and } t > 0. \quad (27)$$

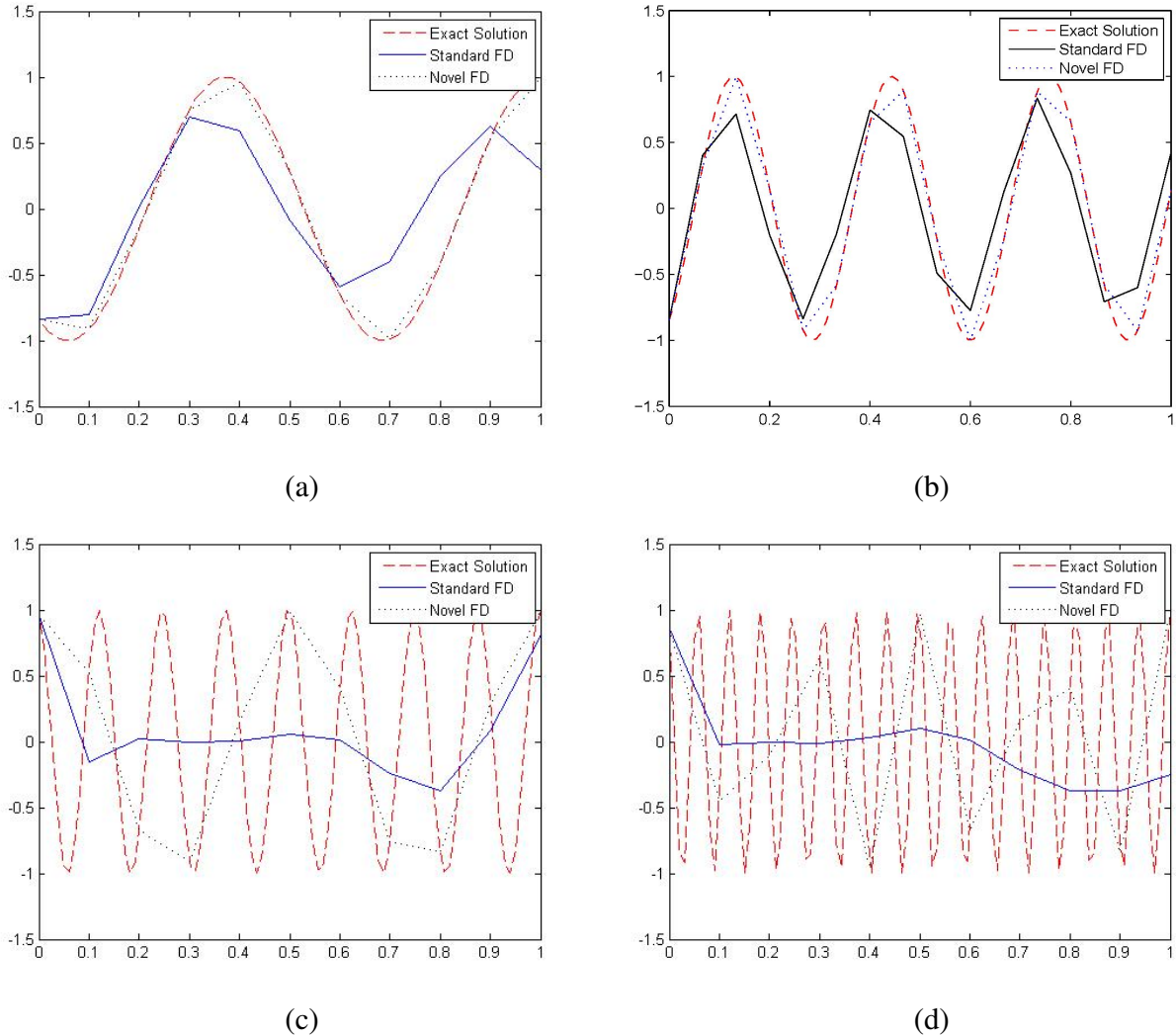


Figure 2: Wave propagation with $r = 0.5$ for (a) $\kappa = 10$, (b) $\kappa = 20$, (c) $\kappa = 50$, and (d) $\kappa = 100$.

In order to construct modified compact explicit scheme, the partial derivatives, $\partial^2 u / \partial x^2$, $\partial^2 u / \partial y^2$ and $\partial^2 u / \partial t^2$, present in (27) are replaced with below given approximation with α chosen as coefficient of the middle node instead of 2 given by

$$\begin{aligned} \frac{\partial^2 u}{\partial x^2} &= \frac{1}{h^2} [u_{i-1,j}^n - \alpha u_{i,j}^n + u_{i+1,j}^n] + O(h^2), \\ \frac{\partial^2 u}{\partial y^2} &= \frac{1}{h^2} [u_{i,j-1}^n - \alpha u_{i,j}^n + u_{i,j+1}^n] + O(h^2), \\ \text{and } \frac{\partial^2 u}{\partial t^2} &= \frac{1}{\ell^2} [u_{i,j}^{n-1} - \alpha u_{i,j}^n + u_{i,j}^{n+1}] + O(\ell^2). \end{aligned}$$

Substituting above approximations in (27) and performing simplifications gives

$$u_{i,j}^{n+1} = (cr)^2 (u_{i-1,j}^n + u_{i+1,j}^n - \alpha u_{i,j}^n + u_{i,j-1}^n + u_{i,j+1}^n) - u_{i,j}^{n-1}. \quad (28)$$

Now the value of α is calculated by inserting $u_{i,j}^n = e^{i(h(ik_1+jk_2)-\omega n\ell)}$ into (28)

$$\alpha = \frac{2}{(2(cr)^2 - 1)} [(cr)^2 (\cos(k_1h) + \cos(k_2h)) - \cos(\omega\ell)]$$

with $k_1 = k \cos(\theta)$ and $k_2 = k \sin(\theta)$ satisfying $k^2 = k_1^2 + k_2^2$ and θ is the incident angle. Inserting this value of α in (28), gives required modified compact explicit scheme for two dimensional case

$$u_{i,j}^{n+1} = (cr)^2 (u_{i-1,j}^n + u_{i+1,j}^n + u_{i,j-1}^n + u_{i,j+1}^n) + \frac{2u_{i,j}^n}{(1 - 2(cr)^2)} [(cr)^2 (\cos(k_1h) + \cos(k_2h)) - \cos(\omega\ell)] - u_{i,j}^{n-1}. \quad (29)$$

Similarly, modified compact implicit scheme for two dimensional case is given by

$$\begin{aligned} \frac{(cr)^2}{4} [u_{i-1,j}^{n+1} + u_{i+1,j}^{n+1} + u_{i,j-1}^{n+1} + u_{i,j+1}^{n+1}] &= -\frac{(cr)^2}{2} [u_{i-1,j}^n + u_{i+1,j}^n + u_{i,j-1}^n + u_{i,j+1}^n] \\ &\quad - \frac{(cr)^2}{4} [u_{i-1,j}^{n-1} + u_{i+1,j}^{n-1} + u_{i,j-1}^{n-1} + u_{i,j+1}^{n-1}] \\ &+ \left[1 + \frac{(cr)^2}{2} (\cos(k_1h) + \cos(k_2h)) + \frac{1 - \cos(\omega\ell)}{1 - \cos(\omega\ell)} \right] (u_{i,j}^{n-1} + u_{i,j}^{n+1}) \\ &- \left[2 - (cr)^2 (\cos(k_1h) + \cos(k_2h)) - \frac{2(1 - \cos(\omega\ell))}{(cr)^2(1 - \cos(\omega\ell))} \right] u_{i,j}^n. \end{aligned} \quad (30)$$

4.1 Dispersion Analysis

Now to avoid repetition, following steps as presented in Section 4.4 inserting a plane wave solution of the form $u_{i,j}^n = e^{i(\tilde{k}_1ih + \tilde{k}_2jh - \omega n\ell)}$, with \tilde{k}_1, \tilde{k}_2 as discrete wave numbers into either (29) and (30) results into following after straight forward manipulations

$$[\cos(\tilde{k}_1h) - \cos(k_1h)] + [\cos(\tilde{k}_2h) - \cos(k_2h)] = 0$$

which implies

$$\tilde{k}_1 = k_1 \text{ and } \tilde{k}_2 = k_2.$$

5 Conclusions

In this work range of modified compact central finite difference (C.F.D.) schemes are constructed in case of rectangular grid for one dimensional transient wave equation. Salient features of these schemes are given below:

1. they provide compact stencil i.e. minimum number of grid nodes are involved;

2. they provide dispersion free numerical results;
3. they do not require to write brand new code altogether which means implementation of these schemes bears no additional cost;
4. cover all range of wave numbers, small as well as large. However, these schemes are constructed for large wave number applications;
5. are computationally attractive and cost effective as achieving optimal results do not require use of fine mesh;
6. leads to standard C.F.D. schemes with series expansion of terms $\cos(\kappa h)$ and $\cos(\omega \ell)$ present in modified schemes;
7. provide highly accurate results even for values of $r > 1$ which is very attractive feature for practical applications.

References

- [1] M. Ainsworth and H. A. Wajid, "Optimally blended spectral-finite element scheme for wave propagation and nonstandard reduced integration," *SIAM Journal on Numerical Analysis*, vol. 48, no. 1, pp. 346–371, 2010.
- [2] G. C. Cohen, *Higher order numerical methods for transient wave equations*. ASA, 2003.
- [3] F. Ihlenburg, *Finite element analysis of acoustic scattering*. Springer Science & Business Media, 2006, vol. 132.
- [4] L. L. Thompson and P. M. Pinsky, "Complex wavenumber fourier analysis of the p-version finite element method," *Computational Mechanics*, vol. 13, no. 4, pp. 255–275, 1994.
- [5] H. A. Wajid and S. Ayub, "An optimally blended finite-spectral element scheme with minimal dispersion for maxwell equations," *Journal of Computational Physics*, vol. 231, no. 24, pp. 8176–8187, 2012.
- [6] F. Ihlenburg and I. Babuška, "Finite element solution of the helmholtz equation with high wave number part i: The h-version of the fem," *Computers & Mathematics with Applications*, vol. 30, no. 9, pp. 9–37, 1995.
- [7] F. Ihlenburg and I. Babuska, "Finite element solution of the helmholtz equation with high wave number part ii: the hp version of the fem," *SIAM Journal on Numerical Analysis*, vol. 34, no. 1, pp. 315–358, 1997.

- [8] I. Babuška, F. Ihlenburg, E. T. Paik, and S. A. Sauter, “A generalized finite element method for solving the helmholtz equation in two dimensions with minimal pollution,” *Computer methods in applied mechanics and engineering*, vol. 128, no. 3-4, pp. 325–359, 1995.
- [9] M. Nabavi, M. K. Siddiqui, and J. Dargahi, “A new 9-point sixth-order accurate compact finite-difference method for the helmholtz equation,” *Journal of Sound and Vibration*, vol. 307, no. 3-5, pp. 972–982, 2007.
- [10] Y. Fu, “Compact fourth-order finite difference schemes for helmholtz equation with high wave numbers,” *Journal of Computational Mathematics*, pp. 98–111, 2008.
- [11] G. Sutmann, “Compact finite difference schemes of sixth order for the helmholtz equation,” *Journal of Computational and Applied Mathematics*, vol. 203, no. 1, pp. 15–31, 2007.
- [12] J. W. Nehrbass, J. O. Jevtic, and R. Lee, “Reducing the phase error for finite-difference methods without increasing the order,” *IEEE Transactions on Antennas and Propagation*, vol. 46, no. 8, pp. 1194–1201, 1998.
- [13] Y. S. Wong and G. Li, “Exact finite difference schemes for solving helmholtz equation at any wavenumber,” *International Journal of Numerical Analysis and Modeling, Series B*, vol. 2, no. 1, pp. 91–108, 2011.
- [14] H. A. Wajid, N. Ahmed, H. Iqbal, and M. S. Arshad, “Modified finite difference schemes on uniform grids for simulations of the helmholtz equation at any wave number,” *Journal of Applied Mathematics*, vol. 2014, 2014.
- [15] H. A. Wajid, “Simulations of the helmholtz equation at any wave number for adaptive grids using a modified central finite difference scheme,” *Turkish Journal of Mathematics*, vol. 40, no. 4, pp. 806–815, 2016.
- [16] E. Twizell, *Computational methods for partial differential equations*. Ellis Horwood, 1984, no. 1.
- [17] I. Singer and E. Turkel, “High-order finite difference methods for the helmholtz equation,” *Computer Methods in Applied Mechanics and Engineering*, vol. 163, no. 1-4, pp. 343–358, 1998.

A Theoretical Analysis of Air Cooling System Using Thermal Ejector Adapted to Operation Conditions for Control Strategy

Mahmoud Bady

Faculty of Engineering, Islamic University of Madinah, KSA

Mechanical Engineering Department, Assiut University, Assiut 271516, Egypt

(On leave)

mfbady@iu.edu.sa

and

Mohamed Ouzzane

Faculty of Engineering, Islamic University of Madinah, KSA

m.ouzzane@iu.edu.sa

Abstract

The thermal ejector is a passive component used for thermal compression, activated by heat (waste or solar), applied mainly for cooling and refrigerating. Nowadays, it is of interest to many researchers and engineers worldwide. The present study introduces a theoretical analysis of the cooling system which uses a gas ejector thermal compression. In such work, the ejector performance is adapted according to the operation conditions of the cooling system in order to attain a control strategy to satisfy the required cooling load with acceptable performance. Theoretical models are developed and applied for the design and simulation of the ejector. Besides the conservation equations of mass, energy and momentum, the gas dynamic equations, state equations, isentropic relations as well as some appropriate assumptions are applied to simulate the flow and mixing in the ejector. These models coupled with the equations of the other components (condenser, evaporator, pump, and generator) are used to analyze the performance of the cooling system. Two FORTRAN programs are developed to carry out the investigation; one for the ejector design and the other is for the simulation purpose. Properties of refrigerant R134a are calculated using real gas equations. Among many parameters, it is thought that the generator pressure is the cornerstone in the cycle. So, it is considered as the key parameter in this investigation to evaluate the cycle performance. The effectiveness of the model is verified by comparing the calculated results with experimental data available in the literature. Then, the simulation results have been used to propose a control strategy to select the appropriate ejector for a given operating condition, where multiple parallel ejectors are

used in the system. From the study results, it was found that; for generator pressures lower than the design pressure, the ejector is working very well, where the cycle performance parameters equal to or lower than the required values by the system design. At high generator pressures, strong shock waves inside the ejector are occurred, which leads to significant condensing pressure at the ejector exit (condenser inlet). At such high pressure, the designed system has the ability to deliver cooling capacity for high condensing pressure during hot seasons.

Keywords

Air cooling system, refrigeration, thermal ejector, thermal compression.

تحليل نظري لنظام تبريد الهواء باستخدام القاذف الحراري المتكيف مع ظروف التشغيل لاستراتيجية التحكم

القاذف الحراري هو عنصر سلمي يستخدم للضغط الحراري ، ويتم تنشيطه بالطاقة الحرارية سواء الطاقة المهذرة أو الطاقة الشمسية، ويستخدم بشكل أساسي في دوائر التبريد والتكييف حيث أصبح القاذف في الوقت الراهن محط اهتمام العديد من الباحثين والمهندسين في جميع أنحاء العالم وبالتالي تقدم الدراسة الحالية تحليلاً نظرياً لدائرة تبريد تستخدم قاذف غازي للضغط الحراري حيث يتم تغيير أداء القاذف وفقاً لظروف تشغيل نظام التبريد من أجل تحقيق استراتيجية تحكم تضمن الحصول علي حمل التبريد المطلوب بأداء مقبول وقد تم تطوير نماذج رياضية نظرية وتطبيقها في عملية تصميم ومحاكاة القاذف إلى جانب معادلات حفظ الكتلة والطاقة وكمية التحرك ، كما تم تطبيق المعادلات الديناميكية للغاز، ومعادلات الحالة ، والعلاقات القياسية وكذلك بعض الافتراضات المناسبة لمحاكاة التدفق والخلط داخل القاذف وتم استخدام هذه النماذج إلى جانب معادلات الاجزاء دائرة التبريد الأخرى مثل المكثف ، المبخر ، المضخة ، والمولد لتحليل أداء نظام التبريد ولعمل هذه الدراسة قام الباحثون بتطوير برنامجين بلغة الفورتران *FORTRAN* لإجراء الدراسة ؛ أحدهما لتصميم القاذف والآخر لعملية المحاكاة وتم حساب خواص مائع التبريد (فريون 134- أ) باستخدام معادلات الغاز الحقيقية ومن بين العديد من المتغيرات ، اعتبر المؤلفون أن ضغط المولد هو حجر الزاوية في دورة التبريد ولذلك تم استخدامه كمتغير رئيسي في هذه الدراسة لتقييم أداء الدورة و تم التحقق من فعالية النموذج الرياضي المستخدم من خلال مقارنة النتائج المحسوبة مع البيانات التجريبية المتاحة في الدراسات القديمة وعلي هذا الاساس تم استخدام نتائج المحاكاة لاقتراح استراتيجية تحكم لتحديد القاذف المناسب لحالة تشغيل معينة ، حيث يمكن استخدام قاذفات متوازية متعددة في نظام التبريد و قد أظهرت نتائج الدراسة أنه عندما يكون ضغط المولد أقل من ضغط التصميم ، يعمل القاذف بشكل جيد للغاية ، حيث تكون معاملات أداء الدورة مساوية أو أقل من القيم المطلوبة من النظام.... أما عند الضغوط الاعلي فإنه تحدث موجات تصادمية قوية داخل القاذف، مما يؤدي إلى ضغط عالي عند مخرج القاذف (مدخل المكثف) وبالتالي، عند هذا الضغط العالي، فإن نظام التبريد تكون لديه القدرة على توفير قدرة تبريد خلال المواسم الحارة.

Nomenclature:

A	Cross sectional area (m ²)
COP	Coefficient of performance (--)
D	Diameter (m)
h	Enthalpy (J/kg.K)
M	Mach number (--)
\dot{m}	Mass flow rate (kg/s)
p	Pressure (kPa)
Q	Heat rate (W)
s	Entropy (J/K)
T	Temperature (°C)
u	Speed (m/s)
V _{son}	Sonic speed (m/s)
\dot{W}	Power (kW)
XL	Section length (m)
ρ	Density (kg/m ³)
ω	Entrainment ratio (--)
ϕ	Coefficient of friction due to mixing
τ	Compression ratio (--)

1. Introduction

Recently, thermal ejectors have received a lot of interest in the cooling system industry. Such interest can be attributed to the energy consumption of conventional compressors, which represents a considerable load on electrical grids, particularly when the cooling demand is high. Additionally, their simple geometry and reduced cost make them very attractive for many applications. The thermal ejector is a passive component used for thermal compression in cooling and refrigerating systems. It can be driven by low-grade heat sources, such as solar collectors, geothermal energy, industrial processes, and waste heat, instead, of high-grade electric energy [1, 2].

The ejector function in the cooling system is the same as the compressor in the conventional systems. However, in the ejector-cooling system, the ejector is considered the key component of the whole system. It is composed of a nozzle, a mixing section, and a diffuser. During the operation, a high-pressure driving flow, which is the primary stream, enters the nozzle, wherein its flow velocity increases. The driving flow reaches sonic velocity at the throat and accelerates into a high-velocity flow with low pressure at the nozzle exit. In such time, a low-pressure flow, which is the secondary stream, enters the ejector from the suction-flow inlet. The flow is

then accelerated towards the mixing section. Then, the two flows are completely mixed inside the mixing section, where a part of the kinetic energy from the primary stream is transferred to the secondary stream. The kinetic energy of the mixed flow converts to pressure energy in a diffuser.

The most important feature in the ejector-cooling system is that; it can use renewable sources of energy to drive the generator. Solar and wind energies represent the most promising energy resources to drive heat-recovery systems, as they are easily accessible and cheap compared to other renewable energy sources. However, the supply of these energies is unstable, which represents a serious problem in the regulation and stabilization of the ejector-cooling systems powered by these energy sources. Accordingly, there is a serious need to design a control technique within the cycle components that can operate the cooling system according to variable operating conditions. From this perspective, the main objective of the current research is to enhance the performance of the ejector-cooling system by controlling the flow conditions with variable operating conditions.

To apply a control technique, the present study proposes the use of multiple parallel ejectors in the cooling system, where only one ejector is in operation. The other ejectors are switched off during the operation of ejector 1 (Ej-1). If -for any variation in the operating conditions of the cycle- the working ejector is unable to attain the required cooling capacity, the refrigerant flow to that ejector is stopped, and the flow path is switched to one of the other ejectors. The control depends basically on the obtained cooling load of the system compared to the desired one, and the cycle the coefficient of performance (COP).

2. Literature Review

Extensive experimental and theoretical investigations on thermal ejectors and their operation have been carried out during the last few decades. However, its modelling still represents a serious problem not yet completely resolved because of its highly complex flow field structure. Ridha et al. [3] studied the conjugate effects of ejector performance characteristics, the activation pressure-temperature conditions at the generator and the interaction with the compressor on refrigeration systems. Besides the conventional compression cycle, they selected three configurations: a hybrid ejector compressor booster and two cascade compressor ejector cycles. Dahmani et al. [4] presented a design methodology for simple ejector refrigeration systems of fixed cooling capacity. They carried out their investigation on four

refrigerants (R134a, R152a, R290, and R600a). Ouzzane et al. [5] derived a local mathematical model and computer programs for ejector studies in refrigeration cycles, one program for optimal ejector design and the other for simulation with more in-built flexibility. The model is based on Munday and Bagster's theory [6] and isentropic flow in the nozzles and the diffuser. In another study by Cardemil et al. [7], a new theoretical ejector model was developed for the performance evaluation of vapor ejectors operating in the critical mode. The model was derived based on the 1-D methodology and made use of real gas equations.

When the ejector is working under variable operating conditions, Yan et al. [8] evaluated the influence of the area ratio on the entrainment ratio, COP and cooling capacity by replacing different sized nozzles. Varga et al. [9] numerically investigated a variable area ratio ejector with a removable needle and found that the entrainment ratio improved 77% compared to a fixed area ratio ejector at a low enough back pressure. Chen et al. [10] developed a two-dimensional theoretical model to study a variable-geometry ejector (VGE) and evaluate its effect on cycle performance. They reported that the VGE is feasible for unstable heat-source utilization where it can be adjusted to its design point to obtain high efficiency. Sag et al. [11] designed an ejector to reduce the throttling losses of a refrigeration system. Their proposed system obtained an optimal performance that had a 5-13% higher COP than the traditional system. Li et al. [12] carried out an investigation of the variable area ratio ejector on a multi-evaporator refrigeration system. The experiments indicated that energy saved was raised to 112 % by the variable area ratio ejector compared to a conventional system. Other experimental results were introduced by Aphornratana et al. [13] who showed the benefit of using an ejector with a primary nozzle that was moved axially in the cylindrical mixing chamber. They reported that; for a given ejector geometry and fixed condenser and evaporating temperatures; there exists an optimum temperature of the primary vapor which maximizes the entrainment ratio and the COP. Fengelei et al. [14] carried out an experimental investigation to study the performance of an ejector refrigeration system with refrigerant R134a. The effects of operating parameters and area ratio on the ejector performance were investigated. They concluded that the ejector performance is immediately changed by varying the ejector operational mode which is determined by the relation between the actual condensing temperature and the critical condensing temperature.

However, in the previous studies, no literature was found concerning the application of control strategy on the ejector flow according to specific operating condition through the application of the multi-ejector system. The present paper appears to be the first step towards more

investigations in the application of control techniques on the cooling system which uses thermal compression ejectors, instead of conventional compressors.

3. Description of the cooling system with ejector

Figure 1 shows a schematic representation of the system under consideration, where the refrigerant is heated in the generator through solar energy (or low-grade energy source). The superheated vapor at state 3 is condensed by rejecting heat Q_{con} to a heat sink, which is normally ambient air or water. At 4, the exit from the condenser, the working fluid is assumed to be saturated liquid (quality $x_4 = 0$). Part of it (the secondary fluid \dot{m}_s) is throttled to low pressure at state 6 and evaporated by receiving heat from another fluid stream. The cooling of this stream represents the useful effect of the system (cooling capacity Q_{evp}). At state 2, the exit from the evaporator, the working fluid is assumed to be saturated vapor (quality $x_2 = 1$). The remaining part of the working refrigerant at state 5 (the primary fluid \dot{m}_p) is pumped to high pressure and superheated from 5 to 1 in the generator by receiving low-grade heat Q_{gen} . The high-pressure vapor at state 1 mixes with the secondary stream at state 2 in the ejector where the exit mixture pressure is the condenser pressure. The mixing process of the two streams is complicated since they mix irreversibly and are compressed through a series of shocks in a constant area chamber.

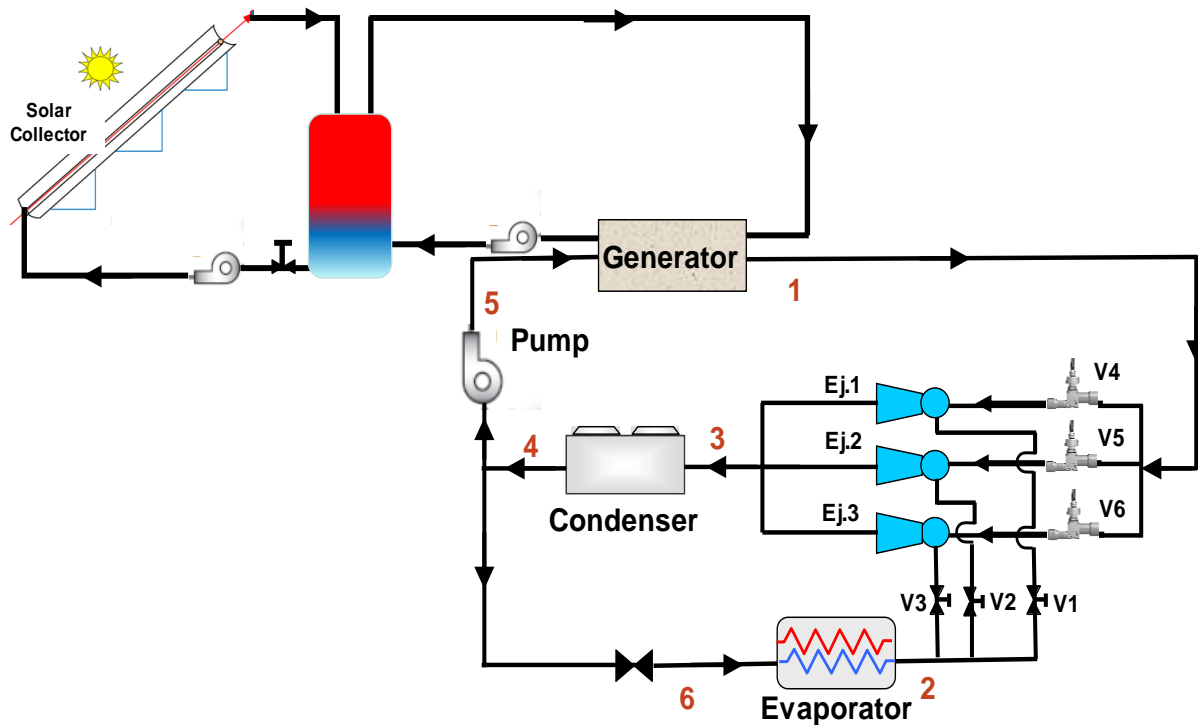


Figure 1: Schematic of the proposed cooling system with an ejector activated by solar energy

4. Mathematical Model of the cooling system with an ejector

The construction of well-designed mathematical models of the ejector has become the key subject of many studies. Many mathematical models, found in the literature, have been developed and employed to analyze, develop and design ejectors. These models include CFD simulations, global models, and numerical models. Although CFD simulations give detailed information concerning pressure, velocity, Mach number...etc, the mathematical analysis using 1-D numerical modelling with computer programs represents a simple method of the flow mixing investigation if the appropriate conditions and equations are considered.

Certainly, the mathematical description of the flow inside the ejector is complex. Besides the conservation equations of mass, energy and momentum, the gas dynamic equations, state equations, isentropic relations as well as some appropriate assumptions need to be used to assist in the description of the flow and mixing in the ejector. Accordingly, to simplify the modeling, without loss of generality, the following main assumptions are applied:

1. The flow inside the ejector is steady and one dimensional.
2. The kinetic energy at the inlets of the primary and secondary flows and at the exit of the diffuser are negligible.

3. Ejector inner wall is adiabatic.
4. Uniform pressure at the position of the mixing section under optimal operating conditions.
5. Primary and secondary streams preserve their identity over some distance following the exit from their respective nozzles, before mixing takes place.
6. The effects of frictional in the nozzles and the diffuser and mixing losses in the mixing chamber are taken into account by using constant coefficients introduced into the isentropic relations.

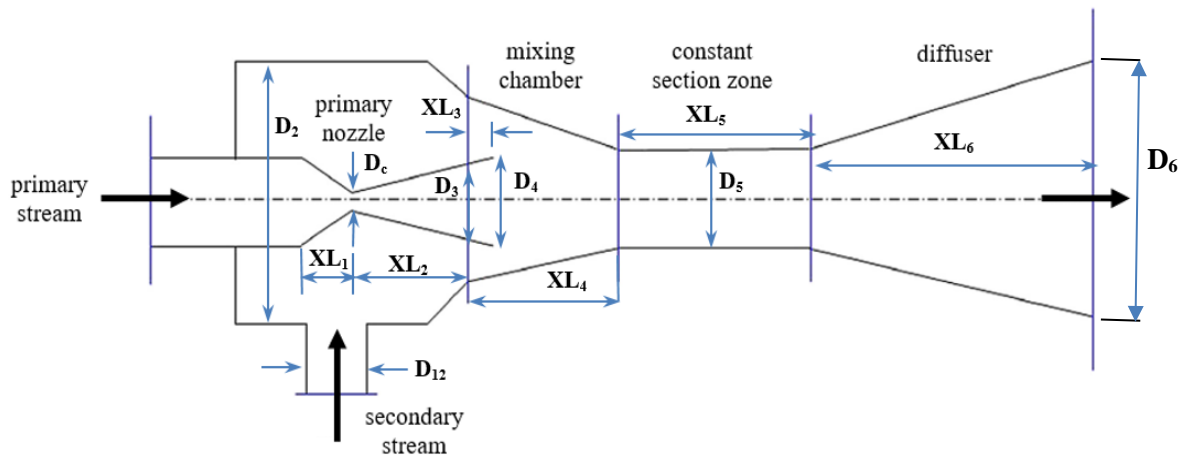


Figure 2 Schematic diagram of ejector geometry.

The fundamental conservation equations of momentum, energy, and mass are applied to elementary control volumes in the different zones of the ejector (primary and secondary nozzles, the mixing chamber, the constant section zone, and the diffuser), as shown in Fig. 2. In such case, for an elementary control volume, shown in Fig. 3, the following equations are applied:

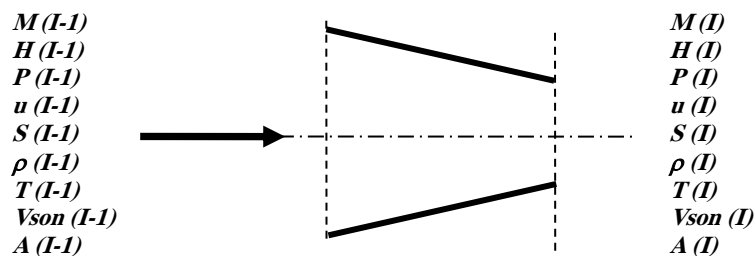


Figure 3 Elementary control volume.

Energy conservation:

$$h(I) + \frac{u(I)^2}{2} = h(I-1) + \frac{u(I-1)^2}{2} \quad (1)$$

Mass conservation:

$$\rho(I) * u(I) * A(I) = \rho(I - 1) * u(I - 1) * A(I - 1) \quad (2)$$

Isentropic compression and expansion:

$$s(I) = s(I - 1) \quad (3)$$

Momentum conservation:

$$\rho(I) * u^2(I) + p(I) = \rho(I - 1) * u^2(I - 1) + p(I - 1) \quad (4)$$

where (I-I) is the inflow section and (I) is the outlet flow section.

For the mixing process, the following equation is applied with the coefficient of friction due to mixing ϕ :

$$\phi[p_1 A_1 + p_2 A_2 + u_1 \dot{m}_1 + u_2 \dot{m}_2] = p A_m + u_m \dot{m}_t \quad (5)$$

where $p_1 = p_2$ and $\dot{m}_t = \dot{m}_1 + \dot{m}_2$

The momentum equation is needed when shock conditions are present, particularly in the constant section zone or during off-design operation. The calculation procedure varies somewhat, depending on the calculation being performed. For design, the optimization criterion is the critical flow in the nozzles (double shocking in the primary and secondary convergent sections, sonic conditions). The conservation equations stated above are applied along the same general lines for both the design and the simulation procedures.

Generally, the ejector performance and geometry are expressed in terms of the entrainment ratio (ω), the compression ratio (τ) and the area ratio (A_r) defined as:

$$\omega = \frac{\dot{m}_s}{\dot{m}_p} \quad (6)$$

$$\tau = \frac{p_3}{p_2} \quad (7)$$

$$A_r = \frac{A_m}{A_t} \quad (8)$$

where A_m is cross-section of the cylindrical mixing chamber and A_t is throat area of the primary nozzle.

The performance of the cooling system as a whole is determined through COP. For systems using an ejector activated by an external heat source, the COP is given by:

$$COP = \frac{\dot{Q}_{evap}}{\dot{W}_p + \dot{Q}_{gen}} \quad (9)$$

where:

$$\dot{Q}_{evap} = \dot{m}_s (h_2 - h_6) \quad (10)$$

$$\dot{Q}_{gen} = \dot{m}_p (h_1 - h_5) \quad (11)$$

$$\dot{W}_p = \dot{m}_s (h_5 - h_4) \quad (12)$$

Similarly, the condenser heat is given by:

$$\dot{Q}_{con} = (\dot{m}_s + \dot{m}_p)(h_3 - h_4) \quad (13)$$

In the case of not considering the generation heat rate when solar/waste energy is used as the heat source, the COP is estimated as:

$$COP = \frac{\dot{Q}_{evap}}{\dot{W}_p} \quad (14)$$

5. Solution Procedure

Simulation and design of ejectors are two requirements of our modelling which cannot be obtained by the same calculation procedure. Some steps are specific to design while others are applied for simulation. Based on these considerations, two program versions are developed: one for design and the other is for simulation.

Ejector design requires the following main input parameters: the cooling capacity (Q_{evap}), the entrainment ratio (ω), generator pressure (p_g), and the evaporator temperature and pressure (p_{evap}) and (T_{evap}). Then, the program then determines the ejector geometry and the dimensions such as the secondary stream inlet diameter (D_{12}), critical diameter (D_{1c}), constant section zone diameter (D_5) as well as ejector exit pressure (p_{exit}). This design corresponds to a unique set of conditions, which is the optimal design point. If outside conditions vary, the ejector will not operate optimally. This new condition will be off-design and cannot be handled correctly by this program version.

The simulation program is written to predict the behavior of a fixed geometry ejector, in response to imposed inlet conditions. The input parameters for this program are the ejector dimensions, generator temperature (T_{gen}) and evaporator temperature (T_{evap}). The program output data are the primary mass flow rate (\dot{m}_p), the secondary mass flow rate (\dot{m}_s), the entrainment ratio (ω), the pressure ratio (τ), ..etc. Modulation functions are embedded in this program such that refrigerant flow rates at an inlet are self-adjusting according to external operating constraints. In this way, ejector operation and performance can be analyzed under different conditions, including off-design situations.

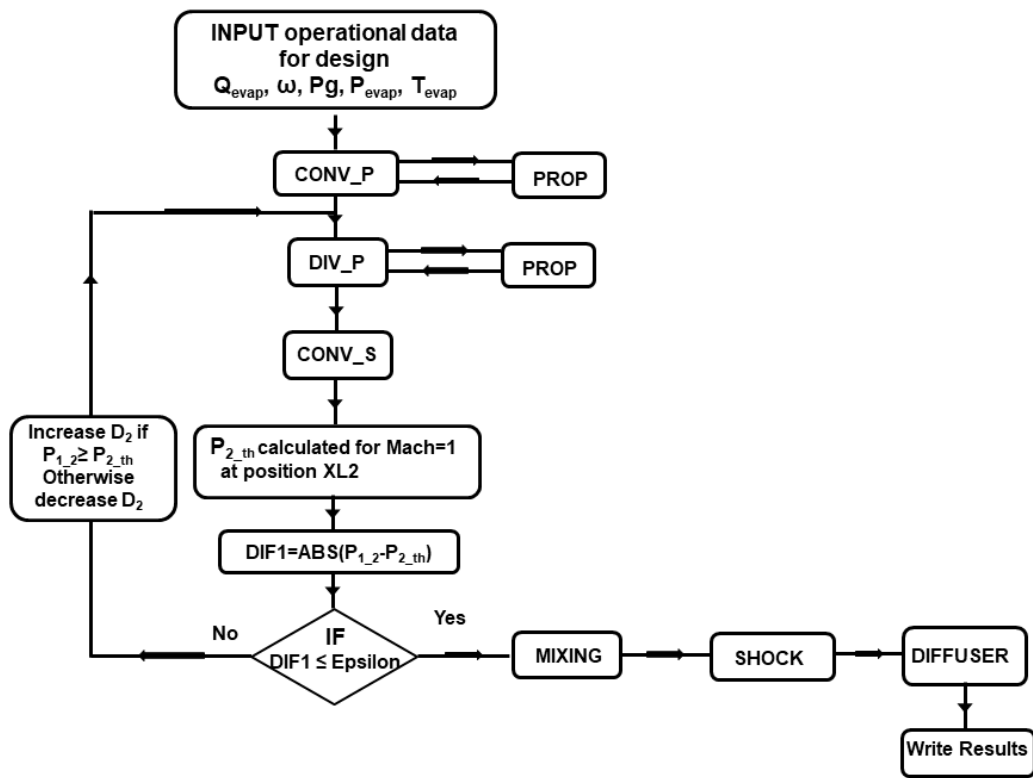
Based on the above system of equations, two different versions of FORTRAN programs are developed; Version A (for design) and Version B (for simulation). For ejector design, the computation progress and control is based on Mach number increments down the subsonic primary convergent until choking occurs (critical condition). At this point ($M = 1$), XL_1 and D_c showed in Fig. 2, are determined. Primary flow progresses through the divergent XL_2 and the fictive expansion cone XL_3 . The final position of the primary stream before mixing is $X = XL_1 + XL_2 + XL_3$, where the prevailing pressure is P_{C1} . Secondary flow starts at $X = XL_1$ and is accelerated to its critical conditions ($M_2 = 1$) at $X = XL_1 + XL_2 + XL_3$. Its pressure condition is P_{C2} . In order for mixing to proceed, critical pressures must match. For this purpose, a pressure test is performed such that:

If $P_{C2} > P_{C1}$, then D_2 is increased

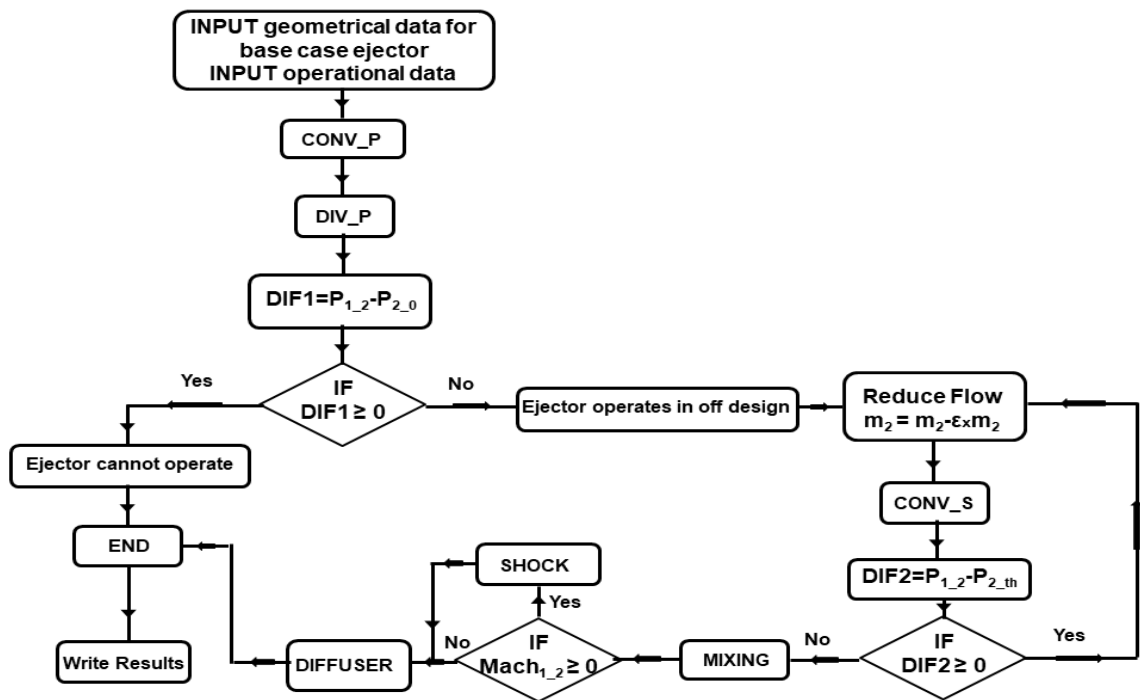
If $P_{C2} < P_{C1}$, then D_2 is decreased

The calculation is repeated until the pressures are close and $P_{C2} \geq P_{C1}$, in which case D_2 is determined. At this point, the flow is supersonic, as it enters the convergent mixing section, where it is slowed down to $M \cong 1$. Then, XL_4 and D_5 are determined. The length of the constant section zone, XL_5 is determined empirically. In this section, a shock wave is produced with a corresponding pressure (and temperature) increase resulting in subsonic flow at the diffuser entry. Additional isentropic compression of the flow takes place in the diffuser to velocity just high enough to flow to the condenser. Values of XL_6 and D_6 are thus determined. Figure 4a shows the solution procedure followed by the authors to design the ejector.

For simulation, the ejector geometry is known, and the physical parameters of operation and performance are to be determined. Since the constitutive equations being of coupled, non-linear type, an iterative procedure given by the flow-charts shown in Fig. 4b is applied to simulate the base case ejector in off-design conditions. For more details concerning the mathematical model and the solution technique, refer to the previous investigation carried by Ouzzane et al. [5].



(a)



(b)

Figure 4 Flowchart of the main iterative calculation steps; a) for design, and b) for simulation.

6. Results and Discussion

In this section, the theoretical model is validated against the published work at first. Then, the results of the mathematical model are introduced, where the parametric analysis, as well as, the performance of the cycle are investigated.

5.1 Validation of the proposed model

The theoretical model used in this study is based on the one developed previously by the co-author of this paper Ouzzane et al. [5] with a small adjustment of certain factors. At this time, the model has been validated using measurement data obtained by Huang et al. [15] for R141-b refrigerant. For comparison purposes, the experimental and theoretical data are presented in the same figure to show the variation of the entrainment factor versus the saturated temperature at the exit of the ejector. It has been found that the trends are similar and the agreement between experimental and calculated data is satisfactory since the discrepancies in the region of off-design don't exceed 13%. Recently, an experimental work carried out by Fenglei et al. [13] on an ejector operating under different modes using the same refrigerant (R134a) as our work has been published. Such paper provided an interesting result and enough information that can be used for validation. The ejector experimented consists of two interchangeable main parts; nozzle and ejector body including mixed chamber and diffuser. The authors combined two different nozzles (A and B) with three bodies (A, B and C) to test different ejectors with different section ratios (A-A, A-C, B-A, and B-B). Based on these data, the two ejector tools developed in the present work; design tool and simulation tool have been validated.

Table 1 presents the results related to the ejector design tool for two different ejectors having two different area ratios respectively: ejector 1 ($A_r = 2.96$) and ejector 2 ($A_r = 2.77$). for calculations, the input data, presented in the first column, are the cooling capacity (Q_{evap}) the entrainment ratio (ω), the temperature of the generator (T_g) and the saturation temperature in the evaporator (T_{evap}). The different geometrical parameters compared are diameters of the throat, divergent, mixing chamber and the exit of the diffuser. The saturation temperature at the exit of the ejector, presented in the last column of the table is also an output parameter used for comparison.

Table1. Comparison of ejector design data against published experimental results [13]

Ejector	D _{1c}		D ₅		D ₁₂		D ₃		T _{cond} (°C)	
	Exp.	Cal.	Exp.	Cal.	Exp.	Cal.	Exp.	Cal.	Exp.	Cal.
<u>Ejector 1</u>										
$A_r = 3.96$										
$Q_{evap} = 2.0 \text{ kW}$										
$\omega = 0.45$										
$T_g = 75 \text{ °C}$										
$T_{evap} = 15 \text{ °C}$										
	2.09	1.97	4.16	3.98	2.70	3.07	12.90	12.73	32.0	35.3
<u>Ejector 2</u>										
$A_r = 2.77$										
$Q_{evap} = 0.55 \text{ kW}$										
$\omega = 0.08$										
$T_g = 75 \text{ °C}$										
$T_{evap} = 10 \text{ °C}$										
	2.50	2.44	4.16	4.37	3.30	4.04	12.90	13.12	34.1	36.8

From the table, it can be seen that; the agreement between the actual ejector sizes and the calculations is very satisfactory. However, the difference in the diameter of the divergent D₁₂ is a little bigger. At this location (exit of the nozzle), the mixing of the two streams starts. This process is the most complicated part of the modeling because of the complexity of multiple physical phenomena including sound waves and high intensity of frictions. On the other hand, the mixing process doesn't happen immediately after the nozzle exit at a constant section, but it occupies a certain length which depends on many parameters and it is very difficult to estimate its value. For the saturation temperature at the exit of the ejector presented in the last column of the table, it's clearly shown that the theoretical model overestimates this parameter due to the assumptions applied in this study.

The simulation ejector tool has also been validated by the experimental data presented by Fenglei et al. [13]. The comparison concerned the variation of the entrainment ratio versus the saturation temperature at the exit of the ejector for ejector 1 operating under the following conditions: $T_g = 75 \text{ °C}$ and $T_{evap} = 15 \text{ °C}$. Figure 5 below shows that the trends of the entrainment ratio ω versus the condenser pressure for both simulation and measurements are similar. In the region of the off-design conditions, a right shift of around 2 kPa is observed in the calculated data due to the same reason as for the ejector design tool. In general, it can be concluded that; we developed two strong tools able to reflect with good accuracy the behavior of the ejectors.

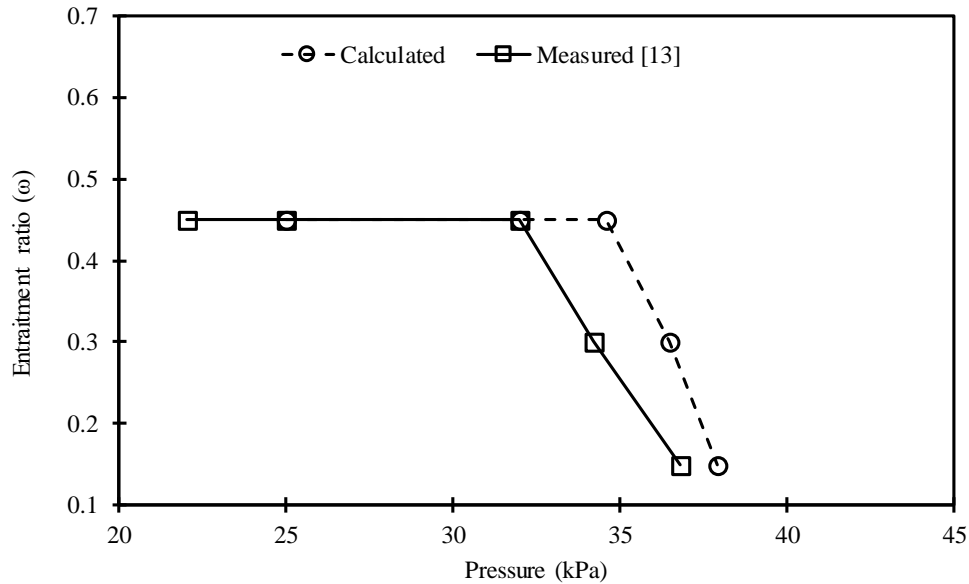


Figure 5 Comparison of entrainment ratio ω versus pressure from calculated and measured data.

5.2 Generator pressure effect

For this study, a base-case is considered, where the input parameters are shown in Table 2.

Table 2. Input parameters and operational conditions for the base-case of ejector 1 design (Ej-1)

Q_{evap} (kW)	ω	$T_{gen(sat)}$ (°C)	p_{gen} (kPa)	\dot{m}_1 (kg/s)	$T_{evap(sat)}$ (°C)	p_{evap} (kPa)	\dot{m}_2 (kg/s)
20.0	0.4	90.0	2116.8	0.268	15.0	488.0	0.107

The design program used these input data to determine the corresponding ejector dimension as presented in Table 3.

Table 3. Dimensions of ejector 1 (Ej-1).

Convergent (primary)	Divergent (primary)	Convergent (mixture)	Constant section	Diffuser
$D_1 = 18.00$	$D_c = 6.4$	$D_2 = 12.63$	$D_5 = 11.90$	$D_5 = 11.90$
$D_c = 6.40$	$D_3 = 9.64$	$D_5 = 11.90$	-	$D_6 = 32.5$
$XL_1 = 26.8$	$XL_2 = 28.0$	$XL_3 = 14$	$XL_5 = 71.00$	$XL_6 = 150.0$
Angle = 14°	Angle = 3°	Angle = 1.5°	-	Angle = 4°

The effect of generator pressure (p_g) on the cooling capacity (Q_{evap}), coefficient of performance of the system, the generator heat load (Q_{gen}) and the condenser saturation temperature (T_{sat}) are

presented in Fig. 6 through Fig. 9. In these figures, there are two curves, the dashed curve, which represents the design results, and the continuous curve which represents the simulation results of the ejector base-case (Ej-1). In such analysis, two different zones are considered; Zone I, for the case when $(p_g)_{\text{system}} \leq (p_g)_{\text{optimal-design}}$, and Zone II, for the case, when $(p_g)_{\text{system}} > (p_g)_{\text{optimal-design}}$.

Figure 6 shows the variation of the evaporator cooling load with the generator pressure. Two important observations can be made: firstly, the cooling load decreases when the generator pressure increases, and secondly, almost identical values of Q_{evap} are obtained for both design and simulation in Zone I. The cooling system, in that case, operates very well. This is mainly due to the low condensing temperature (cold weather).

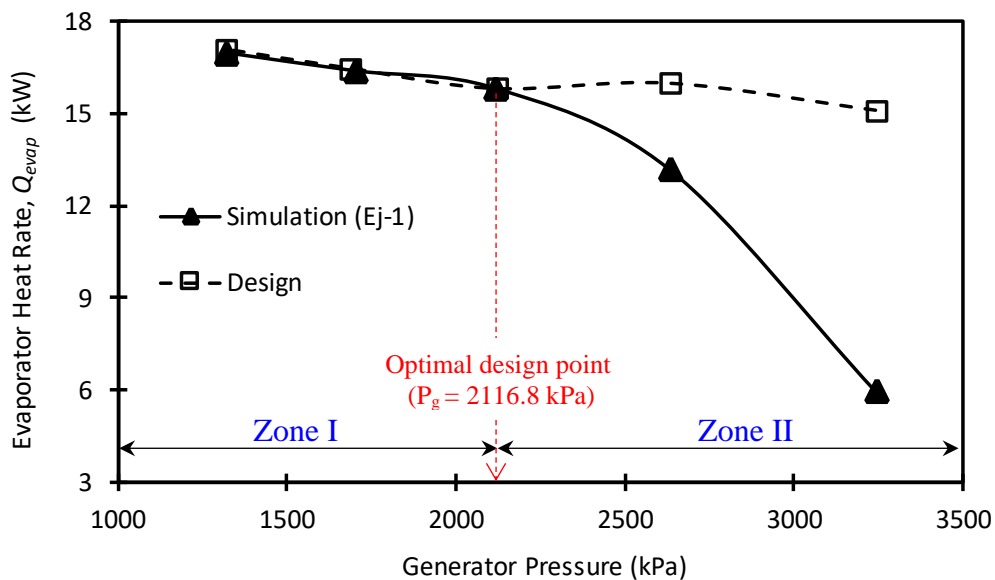


Figure 6. Cooling capacity versus the generator pressure.

On the other hand, increasing p_g beyond the optimal point leads to a considerable decrease in the evaporator cooling capacity. Accordingly, the cooling system cannot satisfy the required evaporator load with acceptable performance. In such a case, increasing the generator pressure increases the mixing pressure at the exit of the primary and secondary nozzles. Thus, the system is not able to deliver the required cooling capacity, since the mass flow rate of the system is lower than that of the optimal design case. Accordingly, a control valve is needed in such a situation to switch the refrigerant to either Ej-2 or Ej-3 depending on the required cooling capacity of the system.

The effect of generator pressure on the generator heat rate is presented in Fig. 7. The design values of Q_{gen} are almost constant with an average value of 51.5 kW, while the simulation heat rate increases sharply as p_g increases. In Zone I, the cooling system operates very well, where

the Q_{gen} is lower than the required value to activate the generator. When p_g exceeds the optimal design value (Zone II), the difference between the design and simulation values becomes positive. In such a case, Q_{gen} is considerably higher than the value required by the system, which is expected to decrease the COP of the cooling system, since the evaporator heat rate decreases with increasing p_g .

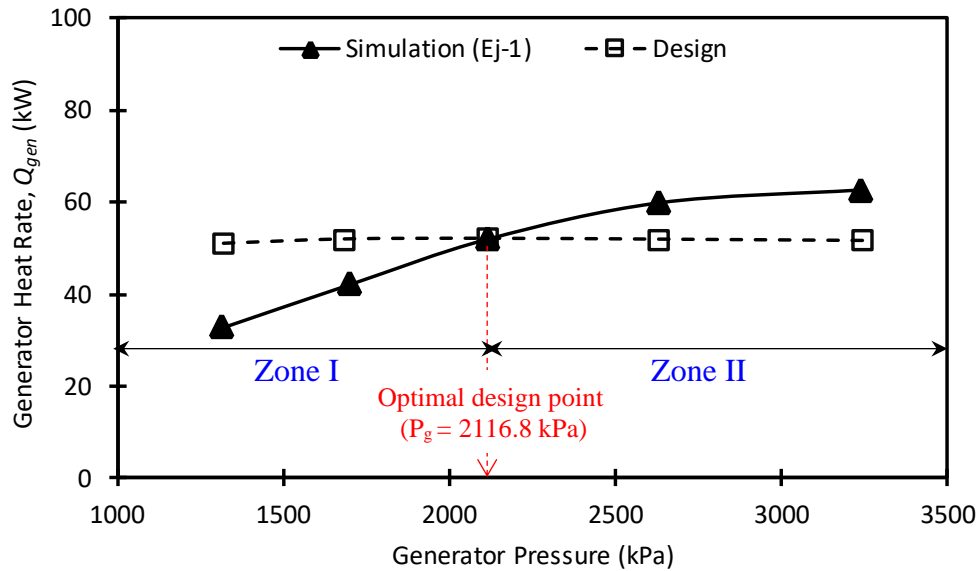


Figure 7. Variation of generator heat rate with the generator exit pressure

At the same time, the cycle COP variation with the generator pressure is illustrated in Fig. 8. The design COP is almost constant at a value of 0.3, while the simulation COP decreases as p_g increases. Such a trend is expected to occur since Q_{evap} decreases and Q_{gen} increases considerably with the increase of p_g , while the pump power does not vary much. Generally, the COP behavior reflects the trends of Q_{evap} and Q_{gen} given in Figs. 6 and 7, respectively.

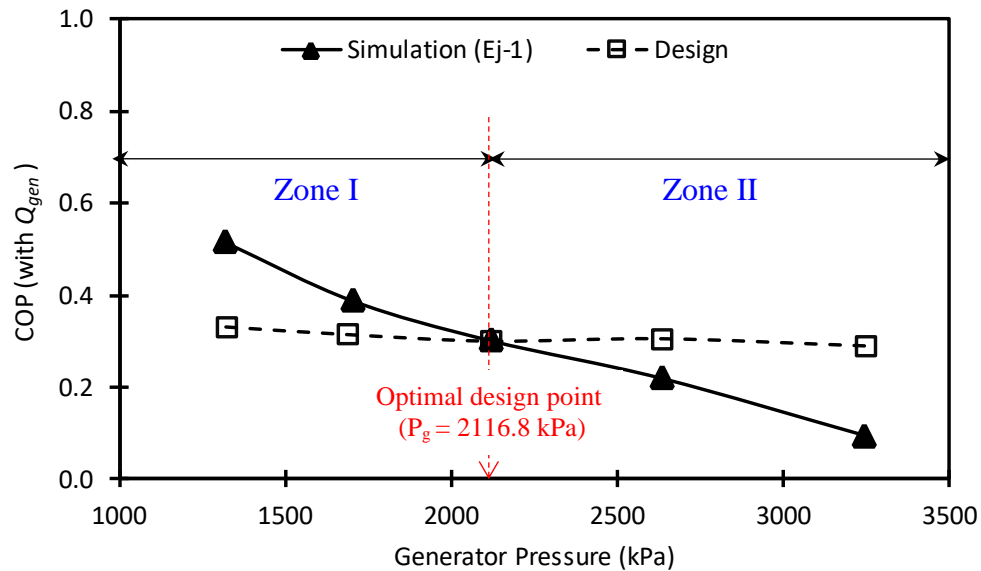


Figure 8. Variation of the cycle COP with the generator pressure.

Figure 9 shows the effect of generator pressure on the condenser saturation temperature. The trends of both design and simulation curves are similar, where they increase as the generator pressure increases.

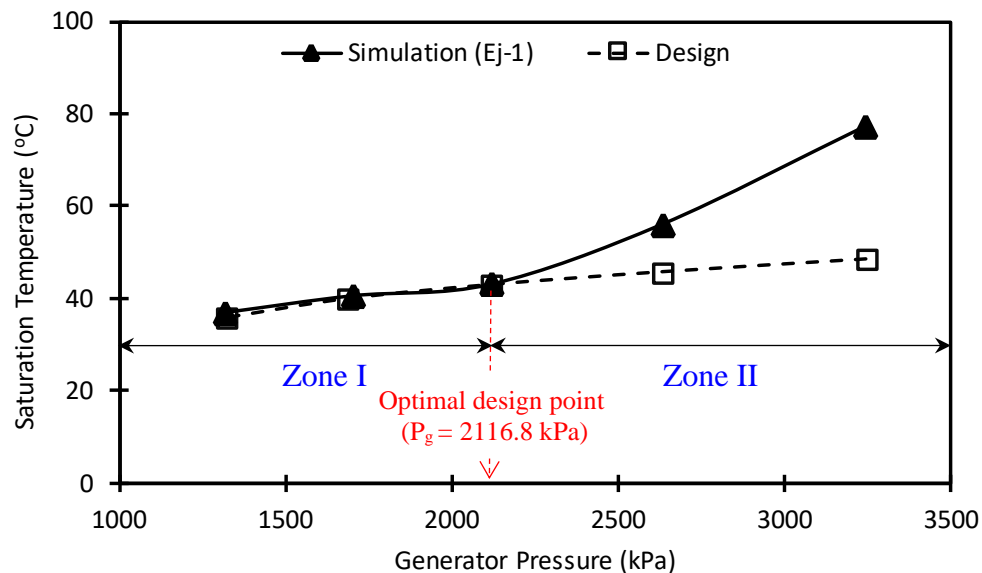


Figure 9. Saturation temperature of the generator pressure versus the generator pressure.

The trend of condenser saturation temperature reflects two important observations. First, the design and simulation values of the saturation temperatures are almost identical when p_g is lower than the optimal design pressure of 2116.8 kPa (Zone I). In this case, the cooling system performs very well, where no extra heat is required to be removed by the condenser. Second, the saturation temperature increases when the generator pressure increases. The required heat

removal rate by the condenser, in this case, is higher than the design values. Such a result, confirms the need for switching the refrigerant flow to either Ej-2 or Ej-3.

One important observation from the above analysis is that; the system can operate very well with a generator pressure lower than the design pressure (Zone I). However, to complete the analysis, the system is not independent of the ambient conditions. Table 4 shows the condenser saturation temperature against the system cooling load at various generator pressures. Clearly, the greater the condenser saturation temperature, the lower the cooling capacity the system can deliver. For the air conditioning application, the condenser is located outside the building and interacts with the external ambient temperature. The ambient temperature must be lower than the condenser saturation temperature to be able to reject heat to the surroundings and then condenses the refrigerant. Such a condition is not easy to be attained since it depends on the weather conditions. Accordingly, the operating generator pressure of the cooling system is affected by the weather conditions (ambient temperature) and not independent of it.

Table 4. Condenser saturation temperature versus the cooling load (Ej-1).

p_g (kPa)	Saturation temperature (°C)	Q_{evap} (kW)
3244.2	77.2	5.97
2633.2	56.0	13.20
2116.8	43.0	15.84
1700.0	40.5	16.41
1317.9	36.9	17.00

From the above discussion, it is clear that a control strategy is required to attain the stable performance of the cooling system for any variation that may occur in the operating conditions. This can be done by adapting the ejector performance according to the operation conditions of the cooling system.

5.3 Control Strategy and Ejector Switching

The above results are obtained when ejector 1 (Ej-1) is the working ejector in the cooling system. For control purpose, some criteria should be followed to attain the required cooling capacity at the same evaporator temperature if the operating conditions for any reason are varied. In this regard, the authors suggest that the operating range of Ej-1 is when the required cooling capacity of the system does not exceed 10 % of the optimal design value. Thus;

$$\text{If } (Q_{evap})_{\text{system}} \leq 1.1 (Q_{evap})_{\text{optimal-design}} \longrightarrow \text{Ej-1 is applied}$$

If such condition is not attained, ejector 2 (Ej-2) is applied, as:

If $(Q_{evap})_{system} > 1.1 (Q_{evap})_{optimal-design}$ \longrightarrow Switch the flow to Ej-2

Similarly, in the case when the required cooling capacity becomes more than 20 % of the optimal design capacity, the flow is switched to ejector 3.

If $(Q_{evap})_{system} > 1.2 (Q_{evap})_{optimal-design}$ \longrightarrow Switch the flow to Ej-3

Following these criteria, multiple ejectors can be added to the system to satisfy the required cooling capacity with any variation in the operating parameters. This control guarantees the stability of the system with any required cooling load.

6. Conclusions

In this paper, a mathematical model was developed to investigate the ejector-based cooling system performance and hence, enabled setting a control strategy that can satisfy the required cooling load with a stable performance. Two FORTRAN programs were developed to carry out the investigation; one for the ejector design and the other was for the simulation purpose. The generator pressure was considered as the main variable in the analysis. The simulation results have been functioned to propose a control strategy to select the appropriate ejector for a given operating condition, where multiple parallel ejectors can be used by the system. From the simulation results, the following conclusions arise:

1. The operating generator pressure of the cooling system is affected by the weather conditions (ambient temperature) and not independent of it. So, the selection of the operating p_g depends basically on the weather condition.
2. For pressures lower than the optimal design pressure, Ej-1 is working very well, where the cycle performance parameters equal to or lower than the required values by the system design.
3. The range of operation of Ej-1 is when the required cooling capacity of the system does not exceed 10 % of the optimal design value. When $(Q_{evap})_{system}$ is in the range from 11 - 20 % of the design cooling load, the flow is switched to Ej-2. For $(Q_{evap})_{system}$ greater than 20% of the optimal design cooling load, Ej-3 will be the operating ejector. More ejectors can be added in the same way to the system, according to the desired cooling load by the system.

7. References

- [1] S. He, Y. Li, R.Z. Wang, Progress of mathematical modelling on ejectors, Renew. and Sust. Ener. Rev. 13 (2009) 1760–1780.

- [2] L. Wang, J. Liu, Tao Zou, J. Du, F. Jia, Auto-tuning ejector for refrigeration system, *Energy* 15 (2018), 536-543.
- [3] M. Ridha, M. Ouzzane, Z. Aidoun, Numerical evaluation of ejector-assisted mechanical compression systems for refrigeration applications, *Inter. J. of Ref.* 43 (2014), 36-49.
- [4] A. Dahmani, Z. Aidoun, N. Galanis, Optimum design of ejector refrigeration systems with environmentally benign fluids, *Inter. J. of Therm. Sci.* 50 (2011) 1562-1572.
- [5] M. Ouzzane, Z. Aidoun, Model development and numerical procedure for detailed ejector analysis and design, *App. Therm. Eng.* 23 (2003), 2337–2351.
- [6] J. Munday, D. Bagster, A new theory applied to steam jet refrigeration, *Indus. & Eng. Chem. Process Design and Development* 16 (1977); 442–449.
- [7] J. Cardemil, S. Colle, A general model for evaluation of vapor ejectors performance for application in refrigeration, *Energy Convers Manag* 64(2012), 79-86.
- [8] Y. Jia, C. Wenjian, Area ratio effects to the performance of air-cooled ejector refrigeration cycle with R134a refrigerant. *Energy Convers Manag* 53(2012), 240-246.
- [9] S. Varga, P. Lebre, A. Oliveira, CFD study of a variable area ratio ejector using R600a and R152a refrigerants, *Int. J. Refrig.* 36(2013), 36(1):157-165.
- [10] Z. Chen, X. Jin, C. Dang, E. Hihara, Ejector performance analysis under overall operating conditions considering adjustable nozzle structure, *Int. J. Refrigeration* 84 (2017), 274-286.
- [11] N. Sag, H. Ersoy, Experimental investigation on motive nozzle throat diameter for an ejector expansion refrigeration system. *Energy Convers Manag* 124 (2016), 1-12.
- [12] C. Li, J. Yan, Y. Li, et al. Experimental study on a multi-evaporator refrigeration system with variable area ratio ejector. *Appl. Therm. Eng.* 102 (2016), 196-203.
- [13] S. Aphornratana, I. Eames, A small capacity steam-ejector refrigerator: experimental investigation of a system using ejector with movable primary nozzle, *Int. J. Refrigeration* 20 (1997), 352-358.
- [14] L. Fenglei, R. Li, X. Li, Q. Tian, Experimental investigation on a R134a ejector refrigeration system under overall modes. *Appl. Therm. Eng.* 137 (2018), 784-791.
- [15] M. Huang, J. M. Chang, C. P. Wang, V. A. Petrenko, A 1-D analysis of ejector performance, *Int. J. Refrigeration* 22, (1999), 354-364.

Freundlich Isotherm Model of Adsorption of Fe^{2+} , Co^{2+} and Cr^{3+} Ions from Aqueous Solution Using Activated Carbon Prepared from Corn Maize (*Zea mays L.ssp*) Waste.

Nazar Abdualaziz Elnasri

Faculty of Science, Department of Chemistry

Islamic University of Madinah, Saudi Arabia.

nazarelnasri@gmail.com

and

Ahmed Ahmed Alomary

Faculty of Science, Department of Chemistry

Islamic University of Madinah, Saudi Arabia.

ahmedalomary1000@hotmail.com

Abstract

Chemical and physical properties of Activated Carbon (AC-C) prepared from Corn Maize (*Zea mays L.ssp*) waste were determined and the adsorption characterization of Fe^{2+} , Co^{2+} and Cr^{3+} from aqueous solution with respect to Freundlich isotherm and adsorption kinetics were investigated. AC-C was prepared using chemical activation with Potassium Hydroxide (3M at 600 °C for 1 hr). The characterization of (AC-C) revealed that it has 49.42% carbon, 4.2% ash, bulk density of (0.75 g/ml); porosity (57.08%) and methylene blue of 190.6 mg/g. Kinetic adsorption of metal ions (Fe^{2+} , Cr^{3+} and Co^{2+}) has also been investigated at isotherm container at 30°C. The effect of dose of (AC-C) on the percentage removal of metals indicates that the maximum dose of adsorbent was at concentration of 0.8 g/L in which 10% Fe^{2+} was removed. For Fe^{2+} and Cr^{3+} metal ions, the adsorption decreases as the pH increases. The optimum pH for the adsorption was 6 for both Cr^{3+} and Co^{2+} and 7 for Fe^{2+} . The experimental isotherm data was analyzed using Freundlich equations. The adsorption process follows the Freundlich order kinetic, with a correlation coefficient (R^2) of

0.97 for both Fe^{2+} and Co^{2+} and 0.96 for Cr^{3+} . Adsorption capacity (K) and the adsorption intensity (1/n) were the highest for Fe^{2+} , with the values of 1.83 and 1.41, respectively.

Other adsorption factors such as detection of inorganic elements and functional groups on the (AC-C) sample were examined by XRF, XRD and FT-IR spectroscopy. The major elements in the sample were: Potassium (0.047%) and Calcium (3.66%). The FT-IR spectra indicate the presence of five functional groups; 2511 cm^{-1} corresponds to a carboxylic O-H stretching, 1794 cm^{-1} corresponds to an acid anhydride C=O stretching, 1454 cm^{-1} corresponds to aromatic C-H stretching, 874 cm^{-1} is associated with the out of plane C-H wagging and 704 cm^{-1} is in plane C=C bending.

Keywords

Activated Carbon, Corn Maize (*Zea mays L.ssp*) waste, adsorption, Freundlich isotherm, FT-IR and XRD.

نموذج فروندليش الحراري لامتماز ايونات الحديد، الكوبالت والكروم من محاليلها المائية باستخدام الكربون المنشط المحضر من مخلفات الذرة الشامية

تم تقدير الخواص الكيميائية والفيزيائية للكربون المنشط المحضر من مخلفات نبات الذرة الشامية كما تمت دراسة حركية الامتماز لتقييم ملائمة الكربون المنتج في امتماز ايونات الفلزات (الحديد و الكوبالت و الكروم) من محاليلها المائية. أظهرت نتائج عملية الامتماز ملائمة نموذج معادلة فروندليش للعينات المنشطة كيميائياً. تم القيام بعملية التنشيط الكيميائي باستخدام محلول هيدروكسيد البوتاسيوم بتركيز (3 مولار) في درجة حرارة 600 درجة مئوية لمدة ساعة.

أظهرت نتائج التحليل الكيميائي أن نسبة الكربون تبلغ (49.42%) ومحتوى الرماد (4.2%) والكثافة الظاهرية (0.75غم/مل). يعتبر تحديد ونوع المسامات الموجودة بالكربون المنشط عامل اساسي لتقييم كفاءة الكربون المنتج كمادة امتماز، نتائج تحديد نسبة المسامات الكلية اظهرت احتواءه على (57.08%). واختبار ازرق الميثيل (190.6 ملغم/غم) تم دراسة حركيات الامتماز لمحاليل ايونات فلزات الحديد والكوبالت والكروم عند درجة حرارة 30 درجة مئوية، كما تم دراسة تأثير جرعة الكربون المنشط اللازمة لازالة ألوان محاليل الفلزات وكانت الجرعة المناسبة عند تركيز (0.8 غم/لتر).

وجد ان الرقم الهيدروجيني (6) هو المناسب لعملية الامتماز لايوني Co^{+2} و Cr^{+3} والرقم الهيدروجيني (7) لعنصر Fe^{2+} . تم تحليل البيانات المتحصل عليها من التجارب و التي اظهرت ملائمتها معادلة فروندليش ، معامل الارتباط (R^2) يساوي 0.97 و 0.96، سعة الامتماز (K) وكثافة الامتماز (1/n) لعنصر Fe^{2+} كانت 1.83 و 1.41 على التوالي .

تم دراسة بعض العوامل الاخرى المؤثرة على عملية الامتماز باستخدام الاشعة السينية والتي بينت احتواء العينات على انواع وكميات مختلفة من العناصر الغير عضوية وغالبية العناصر المتوفرة هي البوتاسيوم (0.047%) و الكالسيوم (3.66%). التحليل الطيفي للكربون المنشط باستخدام الاشعة تحت الحمراء اظهر احتوائه على خمسة زمر وظيفية:هيدروكسيل عند 2511cm^{-1} زمرة وظيفية لحمض احميدريد $C=O$ عند 1794cm^{-1} . وتشير الاطياف الى وجودزمر وظيفية عطرية لكربون- هيدروجين $C-H$ عند 1454cm^{-1} ، وفي الطيف بين ($704 - 874\text{cm}^{-1}$) تم التعرف على مجموعة $C-H$ خارج المستوى و اخرى $C=C$ داخل المستوى .

1. Introduction

Conversion of agricultural wastes into carbonaceous adsorbents that can be used in many applications such as sugar refining, wastewater treatments and pharmaceuticals industry would add a value to these agricultural commodities, helps reduce the cost of waste disposal, and provide a potentially cheap alternative to existing commercial carbonaceous adsorbents. Activated Carbon as a porous carbon material, usually chars had been subjected to reaction with gases during or after carbonization in order to increase porosity [1]. Activated Carbon is produced from different precursors such as wood, peat, lignite and various types of hard coal and petrochemical products and polymers [2].

The world production of activated carbon in 1990 was estimated to be 375,000 tons, excluding what is produced by Eastern Europe and China. In 2002, the demand for activated carbon reached 200,000 ton per year in the United States. The demands of activated carbon increased over the years and market growth was estimated at 4.6% per year [3]. The strong market position held by Activated Carbon relates to their unique properties and low cost compared with that of possible competitive inorganic adsorbents like zeolites. Heavy metals are produced in large amounts during industrial activities and contaminate the environment. Metal ions are non-biodegradable and many of them are soluble in aqueous media and easily available for living organisms. Heavy metals account for a number of disorders in plants and animals and their removal from aqueous media is an important and challenging task [4]. Various processes for color removal include physical, chemical and biological schemes such as ion exchange, advanced oxidation, filtration, and adsorption [5]. Adsorption has been found to be more efficient process from other techniques for water reuse in terms of initial cost [6], the simplicity of design, use of operation and insensitivity to toxic substances [7].

2. Experimental

2.1. Preparation of Activated Carbon

The general process to produce AC-C is based on carbonizing and activating the carbonaceous precursor material. The method of activation used is described previously [8].

2.2. Chemical Activation

The carbonization of the AC-C was done at 350°C for three hours and allowed to cool at room temperature according to a previously described method [9]. After sample preparation for the activation, 150 grams was mixed with 1000 ml of Potassium Hydroxide (3M). The samples were impregnated in muffle furnace at 600°C for one hour. Washing of the prepared sample was

carried out to clean the base content of the prepared AC-C. The washing process was continued until pH7 was attained. The samples were then dried in an oven at 105 °C to remove any moisture content.

2.3. Estimation of Physical and Chemical Properties for AC-C

The pH was measured using a pH meter (HACH 103), for Moisture Content; 0.5g from the AC-C was placed, weighed to the nearest 0.5g and then placed in a preheated oven at 105 °C. After cooling in desiccators to ambient temperature the weight was measured again, according to a previously published work[9].

2.3.1. Iodine Number

The Iodine number of AC-C was determined according to a standard method which is a titrimetric method. 0.5-2.0 g dried carbon was weighed and transferred to a dry, glass Stoppard 250 ml Erlenmeyer flask. Pipette 10ml of 5% HCl acid in the flask, and swirl until the activated carbon is wetted. Place the flask on a hot-plate in a fume hood, bring the constant to the boil, and allow boiling for exactly 30 seconds. Allow the flask and constant to cool to room temperature, and then add by pipette 100ml of 0.10N iodine solutions. Stopper the flask immediately and shake it vigorously for 30sec. Filter by gravity through a filter paper immediately after shaking period. Discard the initial 20-30ml of filtrate and collect the remainder in a clean beaker. Stir the filtrate in the beaker with a glass rod and pipette 50ml into 250ml Erlenmeyer flask. Titer the 50ml of sample with 0.10N sodium thiosulphate solution until the yellow color has most disappeared. Add 1ml of starch solution and continue titration until the blue indicator color just disappeared. Record the volume of sodium thiosulphate solution used.

[10].

2.3.2. Determination of Porosity/ Bulk Density and Carbon Content

Carbon content, Bulk density and Porosity were determined according to the method described earlier [9], [11] For Bulk density and porosity, a cylinder and an aluminum plate were each weighed; a sample of AC-C was placed into the cylinder and weighed again. The sample was transferred into the aluminum plate and put into an oven so as to dry it to a constant weight at a temperature of 105°C for one hour. The weight of the dried samples was taken again after drying. A clean dry well corked density bottle was weighed. The bottle was filled with water, corked and reweighed. A small quantity of activated carbons was taken and ground to powder, sieved using 106µm in diameter and gradually put into the bottles with little amount of water and weighed again. The bulk density and porosity were calculated using the following expressions [9]

$$\text{Bulk density} = \text{Weight of dry sample (g)}/\text{Volume of tube packed dry AC-C (cm}^3\text{)} \quad (1)$$

$$\text{Porosity} = V_v/V_t \text{ (2)}$$

Where V_v = volume of sample, V_t = total volume.

2.3.3.1 Calculation of Decoloring Efficiency DE (%)

The decoloring efficiency DE (%) was used to determine the decoloring capacity of AC-C. The following equation was employed to quantify the DE (%). The absorbance of original liquor was taken as A_0 and that of filtrate was taken as A [12].

$$\text{DE (\%)} = (A_0 - A)/A_0 \times 100 \text{ \% (3)}$$

2.3.3.2 Calibration curve

For the determination of metals (Fe^{2+} , Cr^{3+} , and Co^{2+}), a calibration standard curve was constructed. A 1% stock solution of (Co^{+2}), Cobalt nitrate ($\text{Co}(\text{NO}_3)_2 \cdot 6\text{H}_2\text{O}$), (Fe^{+2}), Ferrous sulphate hydrous ($\text{FeSO}_4 \cdot 7\text{H}_2\text{O}$) and (Cr^{+3}), Chromium chloride (CrCl_3) was prepared. Then a serial dilution of various concentrations ranging from 0.2-1.0 % was done. The absorbance of the different solution was read using UV spectrophotometer (Model no: C07500E) with the appropriate wavelength (for Cr^{3+} , wave length 600 ± 20 nm, Fe^{2+} wave length 490 ± 20 nm, and Co^{2+} wave length 500 ± 20 nm). the device was operated according to manufacturer instructions.

2.4. Effect of Variable Parameters on the Adsorption Properties

2.4.1.1 Effect of Adsorption Conditions

All equilibrium and kinetic studies of adsorption were carried out according to methods mentioned previously [13, 14].

2.4.2 Doses of the Adsorbent

Different doses of the adsorbent ranging from 0.1-1.0 g were mixed with the metal ion and the mixture was agitated in a water bath with a mechanical shaker. The percentage of different adsorption doses was determined by keeping all other factors constant [14].

2.4.3 Contact Time

The effect of period of contact linking the adsorbent and adsorbate on the removal of the metal ion in a single cycle was determined, where 0.1-1.0 g of AC-C was shaken with 1% of each metal ion (Fe^{2+} , Cr^{3+} and Co^{2+}) at intervals of 20,30,40,50,60,80 and 100 min, respectively. All samples were filtered through a $0.45 \mu\text{m}$ filter paper to remove the carbon fines and then the concentration of

each metal was measured using a UV-VIS spectrophotometer at different wavelengths. Initial concentrations of metals were employed for the study of the effect of initial concentration on adsorption process.

The amount of adsorption (qt) at time (t), was calculated using formula[14]:

$$qt = (C_0 - C_t)V/W(4)$$

Where $C_0 - C_t$ (mg/l) are the liquid phase concentration of metals at initially and at equilibrium, respectively. V is volume of solution (Liter) and W is mass of AC-C used (g). The experiments were carried out at a range of pH 1.0-10.0. The adsorption experiments were carried out at constant temperatures of (30 °C) in a water bath mechanical shaker machine.

2.4.4 pH

Adsorption experiments were carried out at a range of pH 1-10. The acidic and alkaline pH of the medium has been maintained by adding the necessary amounts of hydrochloric acid and sodium hydroxide solutions.

2.4.5 Temperature

The adsorption experiments were carried out at constant temperatures, 30 °C in a water bath mechanical shaker machine (Remi, India). The constancy of the temperature was maintained with an accuracy of $\pm 0.5^\circ \text{C}$.

2.5. XRF Analysis: The prepared AC-C was analyzed using X-ray fluorescence (XRF). AC-C first was crushed into fine powder and then pressed into a pellet form using a 15-ton pressing machine. The diameter of each pellet was about 2.5 cm and a mass about 1.0g. The pellets were subjected to the XRF spectrometer system where each of them was measured for 2000 sec. The spectra obtained as a result of X-ray excitation using Cd-109 X-ray source were transferred to a computer. The absorption spectra were then analyzed and concentration of the elements present in the samples was obtained using AX1L –XRF software.

2.6. FTIR analysis: The samples were grinded and milled with 100 mg KBr to form a fine powder. This powder was then compressed into a thin pellet under 7 tons weight for 5 minutes. The sample was then analyzed using Fourier Transform Infrared spectrometer (Shimadzu 8300) and the spectrum was recorded in a spectral range of 400-4000 cm^{-1} . For Software Operation method of FTIR-8400S analyzer was open firstly then a computer software, where a double click IR solution on the program then press insert background holder, wait for few minutes till spectrum appears in the two windows program, click manipulation and select peak table and then choose calculation measurement on the function tabs.

2.7 XRD analysis: The sample was prepared using bulk mineralogy method given in Fauziguide on XRD diffraction mineralogy of sedimentary rock. The water was chilled at a temperature of 20°C and a pressure of 400 PSI. The XRD diffractometer was switched on at initialization power 15 kV and 5mA. The sample was then analyzed using the xpert -pro system.

2.8 Data Analysis: The results were analyzed using Statistical Packages for Social Sciences (SPSS) program. Comparison between adsorbents and other parameters was completed by one and two-factor ANOVA. Percent relative standard deviations were computed for all replicate samples. All graphs were analyzed using graph PASW statistic software version 18.

3. Result and Discussion

3.1. Proximate Analysis of AC-C:

AC-C sample had carbon content of (49.42%). The results indicated that the bulk density of AC-C was (0.75g/m), while the porosity of the sample was found to be (57.08%). Pore sizes affect the capacity for molecules of different shapes and sizes, and this is one of the criteria by which carbons are selected for a specific application. [3,15]. To gain further knowledge of the porous structure of activated carbon, the adsorption of aqueous I₂ is considered a simple and quick test for evaluating the surface area of activated carbons. The iodine value, defined as the amount of iodine adsorbed per gram of activated carbon at an equilibrium concentration of 0.02N, was measured according to the procedure established by the American Society for Testing and Materials [10]. Amount of carbon content is related to the raw materials [13]. Material consists of plant and extractives are known to vary in chemical structure and initial carbon content. The cellulose is a linear polymer of glucose with a theoretical carbon content of 44.4 %. Lignin is a three-dimensional polymer of aromatic alcohols with a carbon content of 60 – 63%. As a result, the carbon content of a lignocellulosic material is dependent on the relative abundance of its constituents. Thus, the yield of carbon from each component is directly related to the carbon content of the respective components [13]. The power of activated carbon to remove the color as measured in terms of Decoloring Efficiency and expressed as percentage. AC-C has a bulk density of 0.75 g/ml measuring bulk density (BD) give useful data for the estimation of storage and packing volume. Many principles explain the concept of measuring (BD)[16]. Powdered carbons used for decolorization usually have a bulk density in the range 0.25-0.75 g/cm²[7]. A moisture content of AC-C was 2.80% there is a relationship between moisture content and other parameter of activated carbon, presence of carbon-oxygen groups on the surface of carbon and the presence of even small amounts of water vapor increase moisture of activated carbon [5]. Other adsorption factors are listed in Table (1). Decoloring efficiency (DE %) of AC-C was 95.7 % for Fe²⁺ (Table 2) ion.

Table 1. Proximate analysis of the activated carbon prepared from Corn maize waste materials (AC-C) compared to standard activated Carbon.

Parameters	AC-C*	AC**
pH	7.60	7.37-8.30
Bulk Density g/ml	0.75	0.50-0.60
Moisture%	2.80	2.0-10.0
Ash%	4.20	4.0-9.00
Iodine Number	13.00	12.8-18.0
Porosity %	57.08	
Volatile Matter %	23.80	
Carbon Content%	49.42	

*An average of triplicate sample , ** Standard Activated Carbon(parameter of porosity, volatile matter and Carbon content are depends on nature of the raw material used)

3.2 Calibration Curves for metal ions Fe²⁺, Cr³⁺ and Co²⁺

In order to study the adsorption process of activated carbon prepared from the Corn maize (ACC1) the determination of metals concentration a standard curve was constructed for three metals Fe²⁺, Cr³⁺ and Co²⁺. For plotting the calibration curve different concentrations were used for the UV spectrophotometer measurements. The plot of concentration versus absorbance is shown in Figures (1, 2 and 3). Straight line was obtained. The result indicates that higher absorbance attends at higher concentration of the metals.

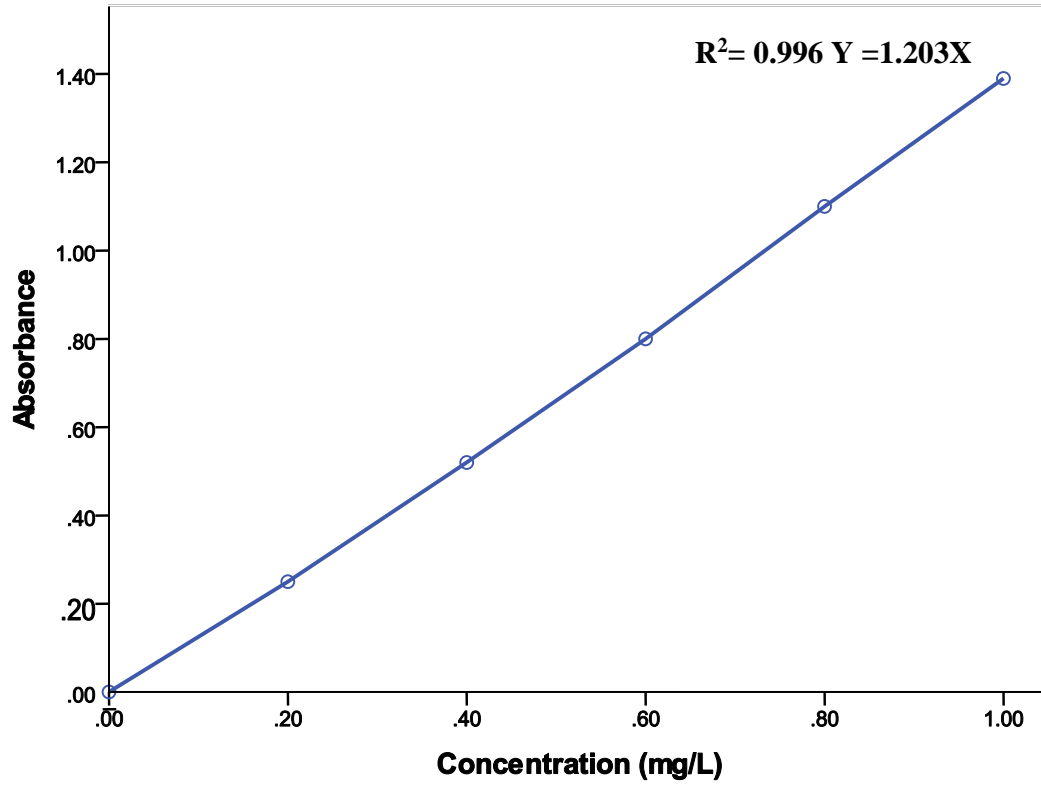


Figure 1. Calibration curve of Fe^{2+}

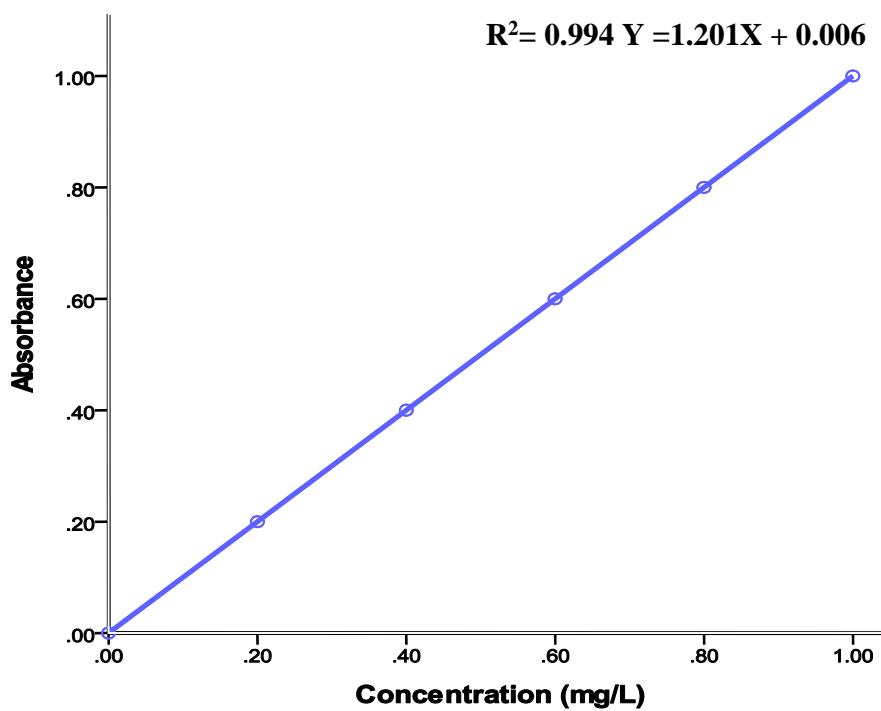


Figure 2. Calibration curve of Cr³⁺

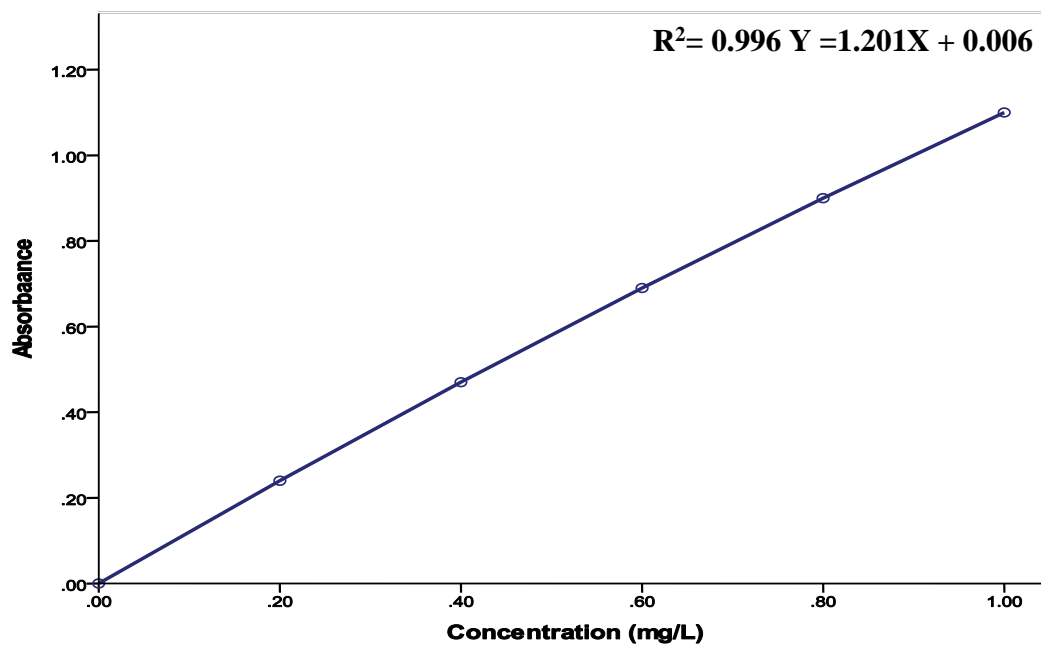


Figure 3. Calibration curve of Co²⁺

Table 2. Decoloring Efficiency% DE of AC-C:

Metals ion	Fe ²⁺	Cr ³⁺	Co ²⁺
Decoloring Efficiency (% DE)	95.7	90.2	88.9

The effect of pH on adsorption of metal ions was investigated and the results are presented in Figure (4). The optimum pH for the maximum uptake of all metals ions was found to be 6 for Cr³⁺ and Co²⁺. The electrostatic attraction between the adsorbent and ions very high at lower pH, but it decreases at higher pH; our result is similar to that mention by [17] but different to that mention by[4]. Thus, the adsorption of metal ions mainly involves electrostatic attractive and repulsive interactions between metal ionic species in the solution and the negative sites on the carbon surface produced by the ionization of acidic groups.

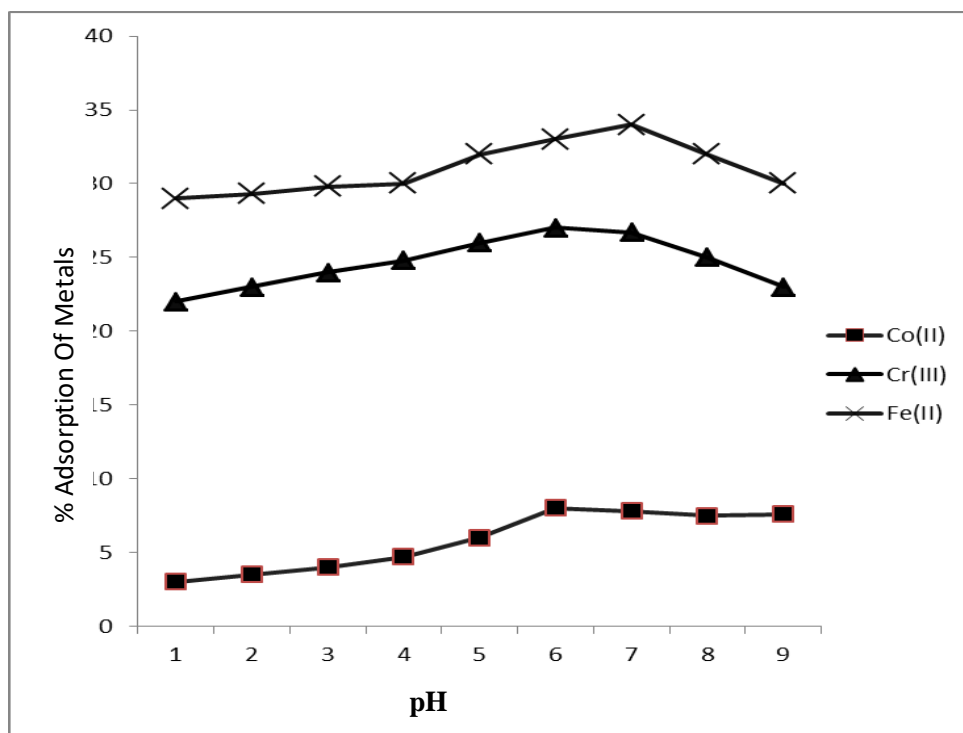


Figure 4. pH Adsorption of metal ions Fe²⁺,Cr³⁺and Co²⁺versus the % of Adsorption on the AC-C.

The effect of the adsorbent dose (Figure.5) was studied at a temperature of 30°Cby varying the sorbent amounts from 0.20 to 1.20 g/L. For all these runs, initial concentration of Fe²⁺,Cr³⁺and Co²⁺was fixed as 1.0 %w/v. Figure(5) shows that the adsorption of Fe²⁺,Cr³⁺ and Co²⁺increases rapidly with the increase in the amount of AC due to greater availability of the surface area at

higher concentration of the adsorbent. For AC-C the significant increase in uptake was observed when the dose was increased from 0.2 to 0.8 g/L. Any further addition of the adsorbent beyond this did not cause any significant change in the adsorption. This may be due to overlapping of adsorption sites as a result of overcrowding of adsorbent particles [12]. One of the Factors affecting the adsorption of metals on to activated carbon is contact time, which is the time required for the liquid or vapor to pass through a carbon column, the contact time results are in Figure 6. The time of the adsorbent-adsorbate is of great importance in adsorption, because it depends on the nature of the system used. The effects of time for the adsorption of Fe^{2+} , Cr^{3+} and Co^{2+} ions were studied between 20 and 100 minutes. it's clear that as the time increase from 20 -100 min the amount of adsorption increase maximum adsorption of 10.7 mg/L was reported at 80 min for Fe(II).

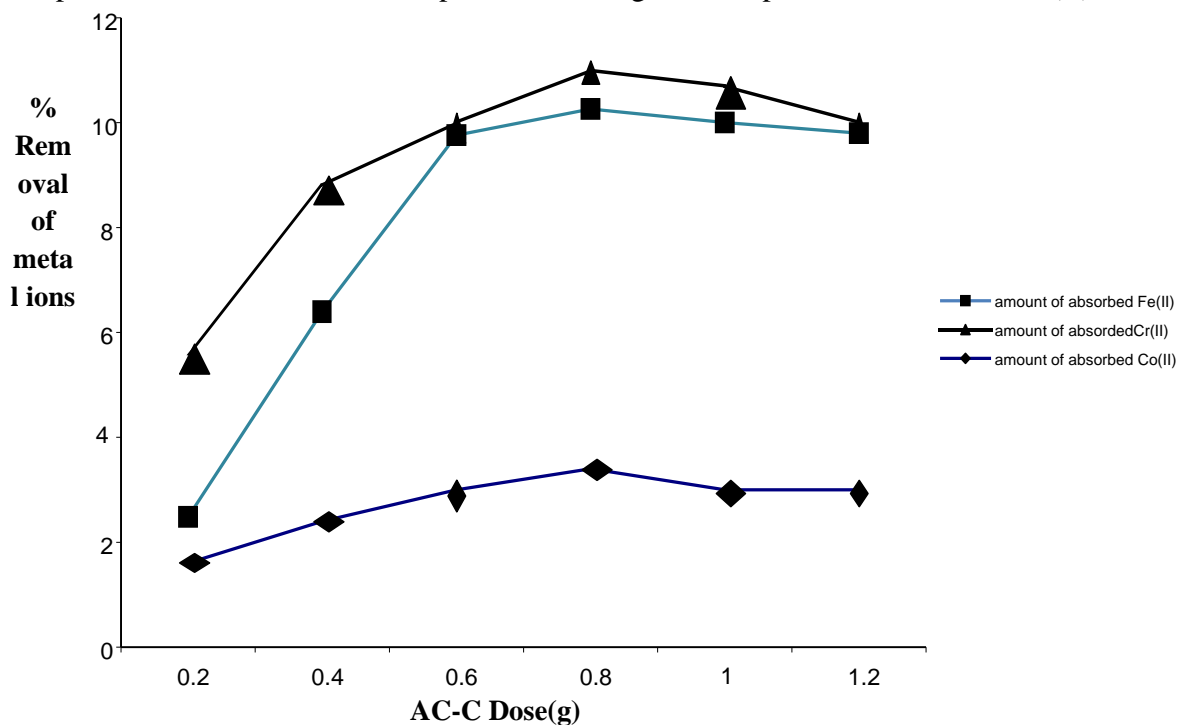


Figure 5. Effect of Adsorbent (AC-C) Dose on Removal of Fe^{2+} , Cr^{+2} and Co^{+3} .

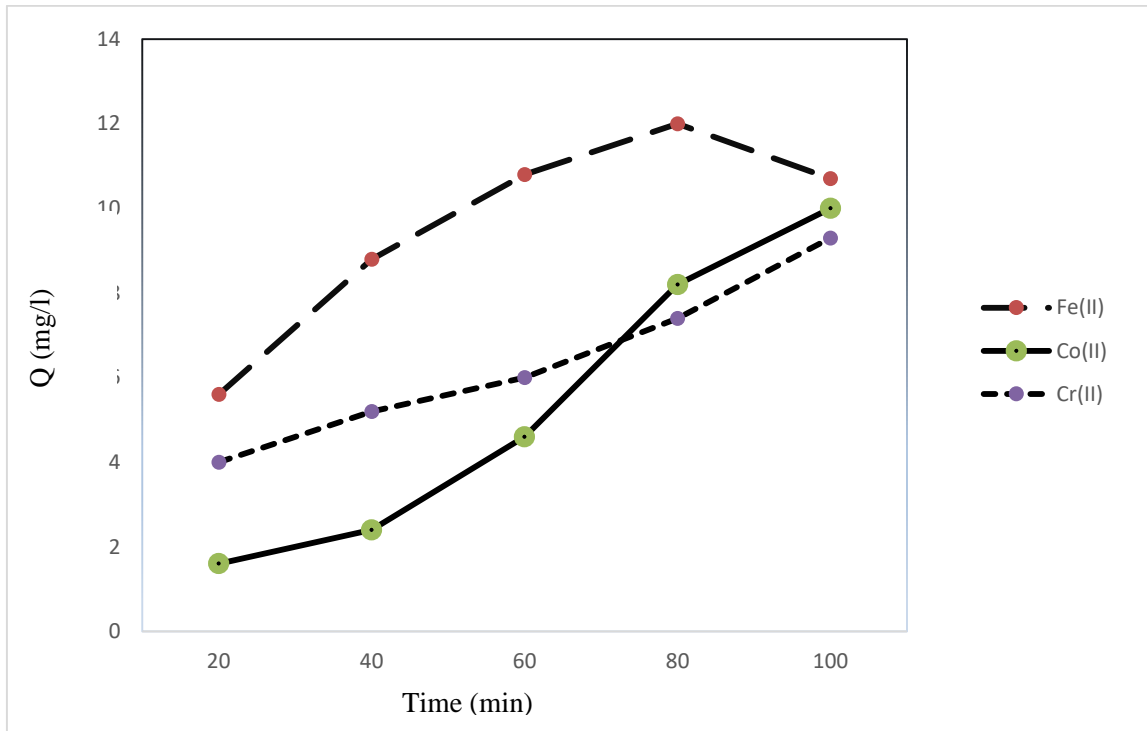


Figure 6. Effect of Contact Time For AC-C.

3.2 Freundlich Isotherm Study for AC-C

Freundlich isotherm is obtained using the empirical equation:

$$q_e = K_F \times C_e^{1/n} \quad (5)$$

Where q_e is amount of metals adsorbed per unit mass of adsorbent at equilibrium, (mg/g), C_e Equilibrium concentration of Fe^{2+} , Cr^{+2} and Co^{+3} mg/L solution. K and $1/n$ is Freundlich constants, K is an indicator of adsorption capacity. The higher the maximum capacity, the higher the K value. The value of $1/n$ is a measure of intensity of adsorption. The higher the $1/n$ value, the more favorable is the adsorption. Figures (7,8, and9), show the data obtained from this study and was used to plot a curve of $\log q$ and $\log C_f$ for Fe^{2+} , Cr^{+2} and Co^{+3} , respectively. The values of K and $1/n$ were calculated from the curves are listed in Table 3.

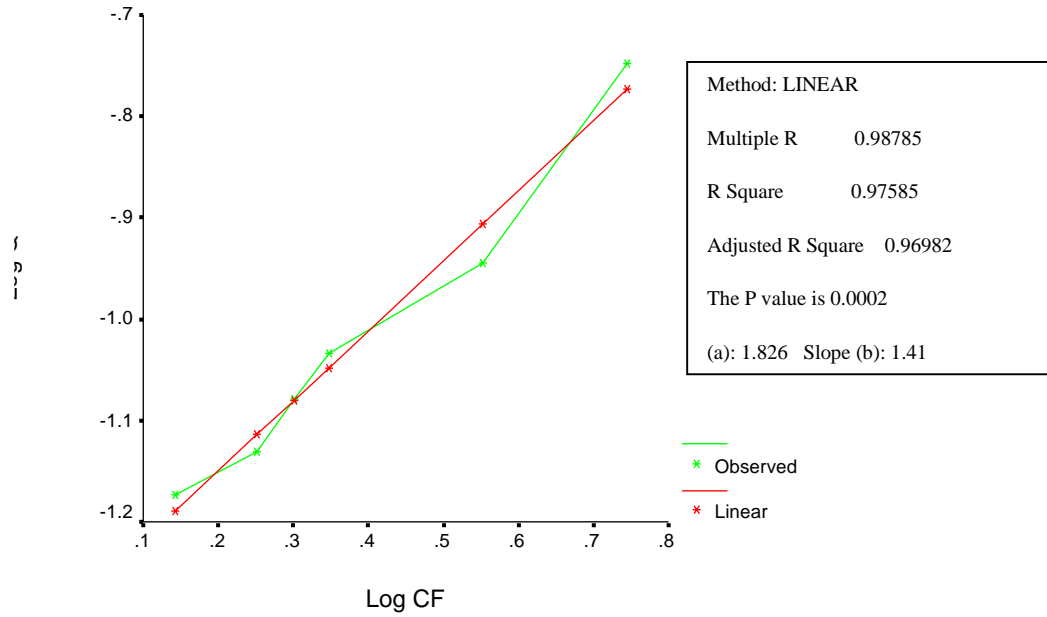


Figure 7 Freundlich Isotherm for the Adsorption of Metal Ion Fe^{2+} onto AC-C.

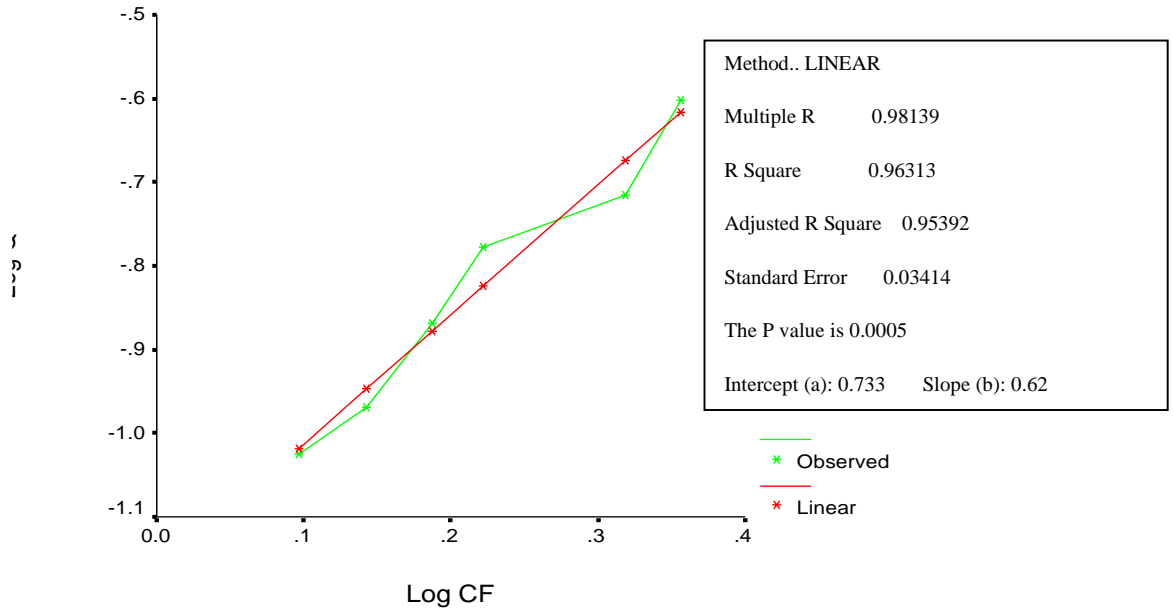


Figure 8. Freundlich Isotherm for the Adsorption of Metal Ion Cr^{3+} onto AC-C.

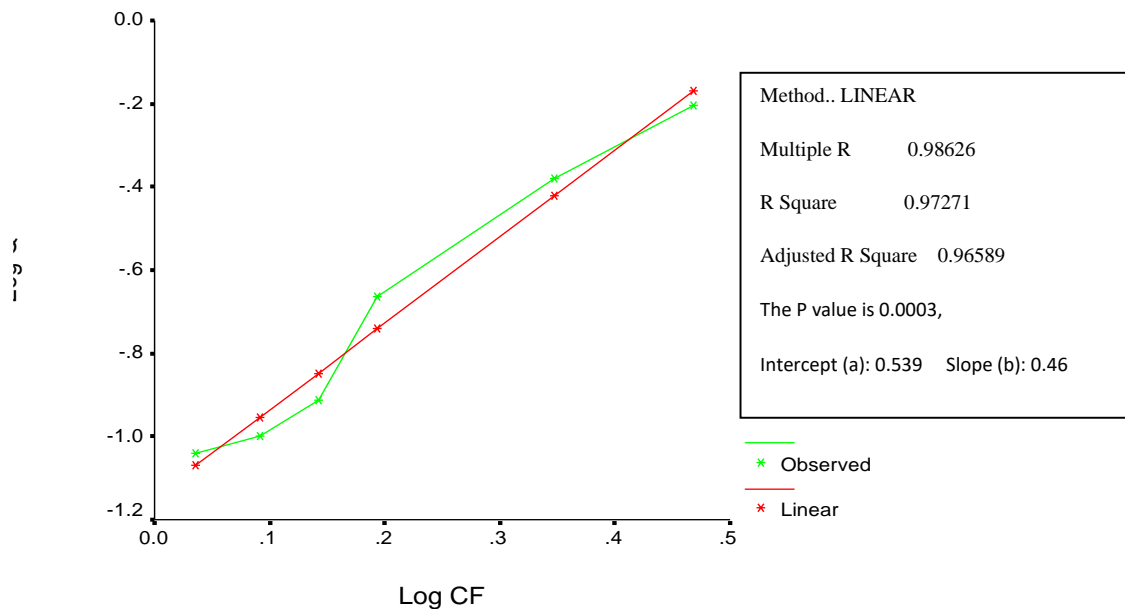


Figure 9. Freundlich Isotherm for the Adsorption of Metal Ion Co^{2+} onto AC-C

The data in Table (3) showed higher value of K for Fe^{2+} which indicate a good adsorption capacity to form a monolayer while moderate adsorption capacities were obtained in the sample that have K value range from 0.54-0.73. Likewise, $1/n$ value of Fe^{2+} indicates good adsorption intensity. Value of R^2 is very important since it gives information about the goodness of fit of a model, (Table 3). In general, the data conform well to the Freundlich equation. The essential models could be described fitting the adsorption phenomena with R^2 value between 0-1. The level of fitness indicate as follows; When $R^2 = 1$ Perfect fit, $R^2 = (0.5-0.9)$ good fit, and $R^2 = (0-0.4)$ poor fit [18]. Our results are similar to that mentioned previously [19].

Table (3). Freundlich isotherm constants for AC-C sample.

Metals Ion	K	$1/n$	R^2
Fe^{2+}	1.83	1.41	0.97
Cr^{3+}	0.73	0.62	0.96
Co^{2+}	0.54	0.64	0.97

3.3. XRF, FT-IR and XRD Analysis:

3.3.1 XRF analysis

XRF of AC-C analysis is shown in in Figure 10. XRF analysis indicated that the percentage of Calcium was 4.24%; other elements that were found in the sample are Iron, copper and strontium. The presence of the inorganic elements in all samples play an important role in adsorption process. Variation in elemental concentrations in AC-C may be attributed to the nature of raw materials used and adsorption study. These elements play an important role in the field of catalysis by transition metals and their compounds, due to their ability to change the oxidation states and to adsorb other substances on their surface as catalyst.

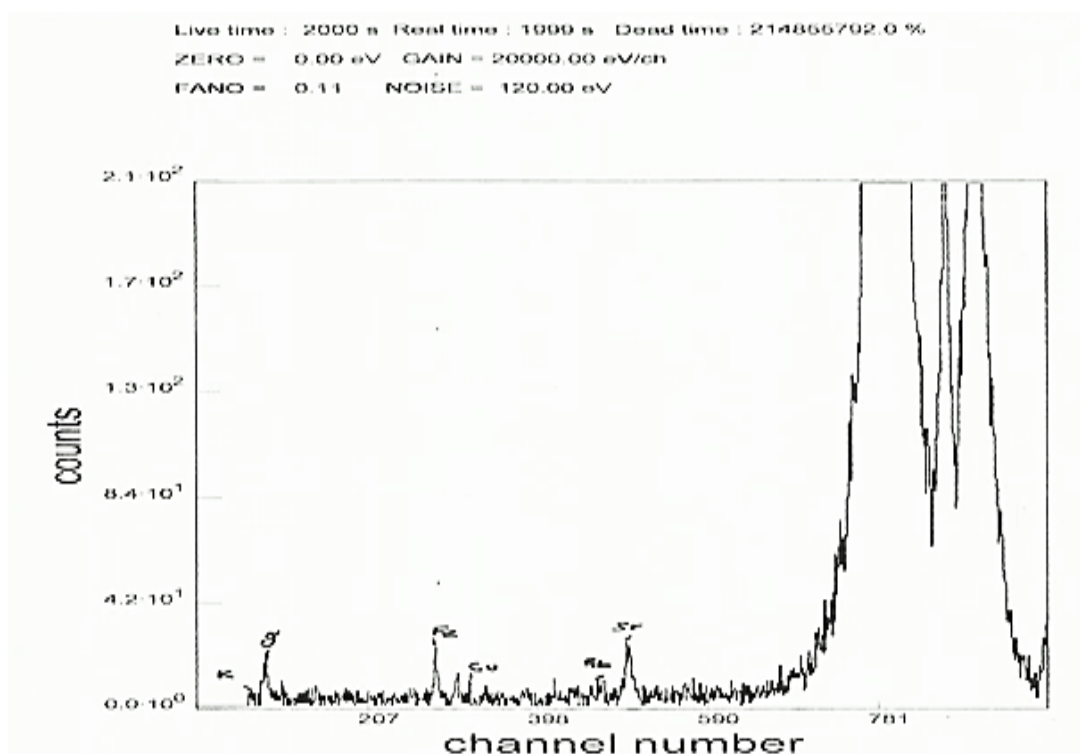


Figure 10. XRF for AC-Csample.

3.3.2FT-IR analysis:

FT-IR is used to identify the functional group on AC-C sample since these functional groups play a significant role in adsorption system. The FT-IR spectra of AC-C are shown in Figure (11).

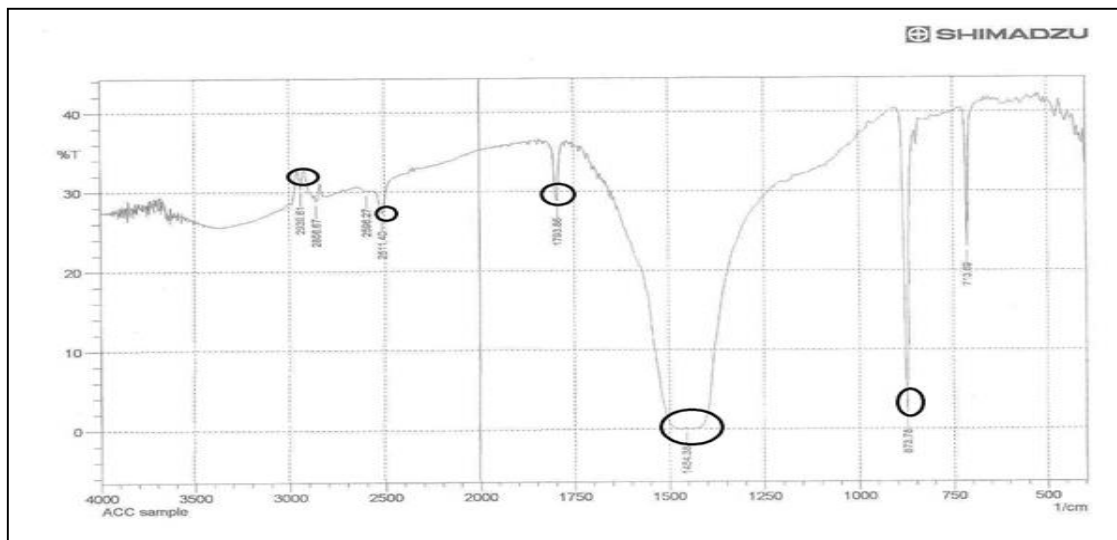


Figure 11. FT-IR spectrum for AC-C

The FT-IR spectra indicate the presence of five functional groups; at frequency of 2511 cm^{-1} a carboxylic O-H stretching which is in agreement with the vibration stretching range ($3300\text{--}2500\text{ cm}^{-1}$) reported previously [20], this could be due to the absorption of water molecules during the process of treatment as result of an O-H stretching mode of hydroxyl groups and adsorbed water [21]. 1794 cm^{-1} corresponds to an acid anhydride C=O stretching which is in agreement with the vibration stretching range ($1800\text{--}1775\text{ cm}^{-1}$) reported previously [20]. 1454 cm^{-1} corresponds to an aromatic C-H stretching which is in agreement with the vibration stretching range ($1400\text{--}1500\text{ cm}^{-1}$), 874 cm^{-1} , 874 cm^{-1} is associated with the out of plane C-H wagging and 704 cm^{-1} is in plane C=C bending reported previously [21]. The chemical structure of activated carbon reported previously [22] explains the functional groups shown in Figure 11.

Functional groups are indicated to more important parameters that influence and determine the adsorption of metal ions from aqueous solutions are the carbon-oxygen functional groups present on the carbon surface. Although all of these surface groups influence the adsorption of inorganics from aqueous phase, the carbon oxygen surface groups are the most influencing and important [20, 21].

3.3.3 XRD analysis

XRD analysis was used to identify the crystallographic structure of the samples using ICDD standard. The results obtained in this study showed that the sample AC-C contain one crystal system of potassium carbonate and chlorine oxide figure (12).

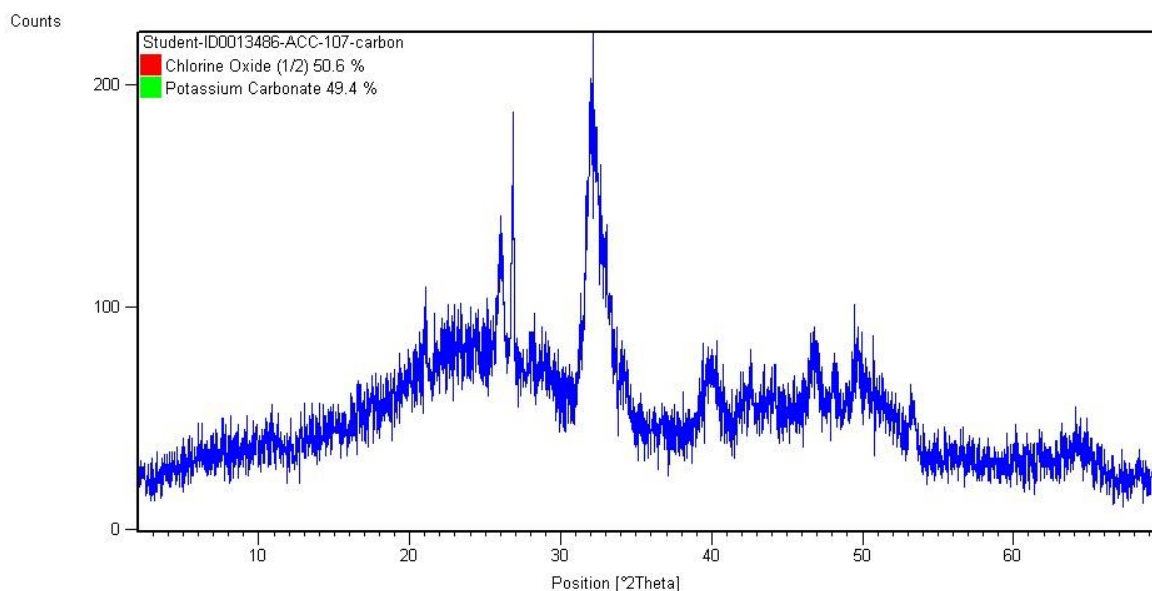


Figure 12.XRD Analysis for AC-C Sample.

The presence of minerals in the prepared activated carbon (AC-C) were further tested by XRD studies. The activated carbon shows two peaks at around $2\theta = 27^\circ$ and 33° which contribute to chlorine oxide and potassium carbonate.[22]

XRD was used to determine the mineralogical and crystal composition of the raw material components as well as qualitative and quantitative phase analysis of multiphase mixtures. The occurrences of minerals in samples were identified by comparing 'D' values (peak intensity and position). It could be supposed that during the KOH activation process, various reactions can be considered with such products as H_2 , K^+ , K_2CO_3 , K_2O and $K(HCO_3)$. At higher temperature, the formation of K_2O is thermodynamically the most stable. The increase of KOH ratios on samples containing a large amount of potassium suggests that the high ratio of KOH may give more K_2CO_3 and K_2O during pyrolysis [7], [22] different minerals were occurred at 002 which indicating different crystalline structure. In this study XRD analysis is associated with ash content since ash content is the starting point for analysis of minerals, thus lower ash content yield low minerals.

4. Conclusion

The present study shows that Corn maize waste is an effective adsorbent for the removal of metal ions Fe^{2+} , Cr^{3+} and Co^{2+} from aqueous solutions. From the kinetic studies, it is observed that adsorption of metal ions increases as the dose of the prepared activated carbon increases. The various properties of the studied material indicate the applicability of corn maize waste as an effective low cost

adsorbent The adsorption process was highly dependent on solution pH and adsorbent dose, also the results showed that the adsorption capacity and intensity are metal dependent; the higher capacity and intensity were for Fe²⁺ ions.

5. References

- [1] H. Marsh, N. Murdie, I. S. Edwards, and H.P Boehm. Interactions of carbons cokes, and graphite with potassium and sodium. In: Chemistry and Physics of Carbon. P.A, Thrower., 20(1987)213-272.
- [2] B. Bronislaw. Preparation of active Carbon by additional activation with potassium hydroxide and characterization of their properties, J.Advances in Materials Science and Engineering 2016.<http://dx.doi.org/10.1155/2016/5819208>
- [3] L.H Wartelle, and W.E Marshall. Granular activated carbons: Physical,Chemical and Adsorptive Properties of Chemical Technology and Biotechnology.76 (2001) 451-455.
- [4] A. Ashraf, S. Khalid and M. Fazal. Removal of chromium (VI) from aqueous medium using chemically modified banana peels as efficient low-cost adsorbent Alexandria Engineering Journal. 55 (2016) 2933-2942.
- [5] M. Joana, C. M, Dias F.Maria,Alvim-FerrazManuel, Almeida JoséRivera-Utrilla. Waste materials for activated carbon preparation and its use in aqueous-phase treatment: A review. <https://doi.org/10.1016/j.jenvman.2007>.
- [6] L. Hung,C.P Chiang ,P.C.Huang, J.H. You Chiang. Effect of metal additives on the physico-chemical characteristics of activated carbon exemplified by benzene and acetic acid adsorption. J of Carbon Elsevier Science. 37(1999) 19-28.
- [7] L.S. Butterworth and J.D.Sember.Wastewateremphasis shifting to toxicity reduction; Granular activated carbon is one treatment technology used to reduce toxicity in wastewater. 25 (1993), 70-72.
- [8] B.Viswanathan, T.K Varadarajan, P .Indra Neel, A process for the preparation of activated carbon from botanical sources, J Indian Pat. (2008) 107-189.
- [9] A.OEktepe, and M.N.R Horsfall. Preparation and Characterization of Activated Carbon derived from Fluted PumpkinStemWaste(*TelfairiaoccidentalisHookF*). Research Journal of Chemical Sciences1(2011) 10-15.
- [10] American Society for Testing and Materials (ASTM) Designation: Standardtest method for determination of iodine number of activated carbon. Method number D4 607-94 (2011)
- [11] CEFIC.Test methods for activated carbon. European council of chemical manufacturers federation.1st version. France (1986).
- [12] M.Ahmedna,,W.E Marshall,. AndR.M Rao, Production of granular activated carbons from selects agricultural by-products and evaluation of their physical, chemical and adsorption properties. J. Bioresource Technology, 7(2001) 113–123.
- [13] S.Jeremias ,L.Macedo, O,Otubo, Iara de Fatima ; Italo Odone M, andB, Silva, Microporous and Mesoporous Materials, J. of surface materials 10(2007) 276-320

- [14] P. Senthil , and K.Kirthika ,. Equilibrium and Kinetic study of adsorption of Nickel from aqueous solution on to Bael tree leaf powder J. of Engineering Science and Technology, Vol. 4 (2009) 351 – 363.
- [15] Y.Gou,S.Yang,K.Yu,J.Zhao, Z.Wang. andH,Xu.The preparation and mechanism studies of rice husk based porous carbon. Materials Chemistry and Physics, 74(2003) 320-223
- [16] H.Halil. Adsorption of Nickel(II) from aqueous solution onto activated carbon prepared from almond husk(2003).[https://doi.org/10.1016/S0304-3894\(02\)00237-6](https://doi.org/10.1016/S0304-3894(02)00237-6)
- [17] P, Subhashree. Production and characterization of Activated Carbon produced from a suitable Industrial sludge. J. of national institute of technology (2011)12-33.
- [18] A.U Itodo and H.U Itodo. Activation chemistry and kinetics of shueanutBiosorbents for Textile waste water treatment. Academia Arena. 2 (2010) 1-4.
- [19] Y.Zhu,D .Wang ,; Zhang XueHong; Qin Hong Dong.Adsorption removal of methylene blue from aqueous solution by using bamboo charcoal. J.Fresenius Environmental Bulletin 3:(2009)369-376
- [20] R.M.Silverstein , F.X.Webster and D.J.Kiemle , Spectrometric Identification of Organic Compounds , 7th ED. John Wiley and Sons (2005)
- [21] G.Socrates , Infrared and Raman Group Frequencies .Tables and Charts John Wiley and Sons (2007)
- [22]Z. Al-Qodah1 and R. Shawabkah. Production and Characterization of Granules Activated Carbon from activated Sludge. Brazilian Journal of Chemical Engineering Vol. 26, No. 01, (2009) 127 – 136

Fundamentals to Detect Tensor Product Bézier Patches in Euclidean 3-Space

M. Khalifa Saad

Math. Dept., Faculty of Science, Islamic University of Madinah, Madinah, KSA
Math. Dept., Faculty of Science, Sohag University, Sohag, Egypt
mohamed_khalifa77@science.sohag.edu.eg, mohammed.khalifa@iu.edu.sa

Abstract

The aim of this paper is to deliver the fundamentals to detect Bézier patches of scanned objects based on their normal congruence. In five-dimensional real projective space (P^5), we introduce a new approach for tensor product (TP) Bézier patch representation. For this reason, we use Plücker coordinates which are a way to assign six homogeneous coordinates to each line in three-dimensional projective space (P^3). Derivatives, normal vectors of Bézier patches and some of geometric properties of these patches are discussed. Further, the special case, biquadratic Bézier patch is introduced. The Plücker coordinates of the normal congruence of the patch are functions of order 14 in general, because of that high degree, it seems not to be of practical use to calculate the focal points of the normal vectors of the patch in general. We try these calculations for the biquadratic patches ($m=n=2$). Finally, we present a computational example to compute the two focal points of a normal of this patch.

Keywords

TP-surfaces, Curvature lines, Normal congruence, Focal surfaces of congruence, Plücker coordinates.

أساسيات تحديد قطع سطوح بيزيه في الفراغ الإقليدي ثلاثي البعد

الهدف من هذا البحث هو تقديم الأساسيات لتحديد قطع سطوح بيزيه من المجسمات المسوحة ضوئياً بناءً على أعمدتها المتوافقة. في الفضاء الإسقاطي ثلاثي الأبعاد (P5)، نقدم طريقة جديدة لتمثيل Tensor (TP) Bézier patch. لهذا الغرض، نستخدم إحداثيات *Plücker* التي تعد وسيلة لتعيين ست إحداثيات متجانسة لكل خط مستقيم في الفضاء الإسقاطي ثلاثي الأبعاد (P3). وتم مناقشة المشتقات والمتجهات العمودية على هذا النوع من السطوح وبعض الخصائص الهندسية لهذه القطع السطحية. علاوة على ذلك، تم تقديم الحالة الخاصة *biquadratic Bézier patch* وبسبب الدرجة العالية للدوال المستخدمة، ستبدو الحسابات بدون فائدة بشكل عام لذلك نحن نحاول عمل هذه الحسابات للقطع السطحية الخاصة ذات البعد الثنائي للدوال المستخدمة *biquadratic (m=n=2)*. أخيراً، قمنا بتقديم مثالاً حسابياً لحساب نقطتين بؤريتين للأعمدة عند النقاط الحدية للسطح ورسمنا هذه النقاط والسطوح باستخدام أحد حزم البرامج الرياضية الجاهزة.

1. Introduction

Space curves and their frames is important in differential geometry, Mechanics and Physics. They have many applications in Computer Aided Design (CAD), Computer Aided Geometric Design (CAGD) (for more details, see [1-6]).

In reverse engineering the detection of special classes of CAGD generated surfaces is often based on the line congruence of normals and the GAUSS-image of such a surface. For surfaces with a “kinematic generation”, as example helical surfaces or surfaces of revolution, the congruence of normals belong to a linear complex and this fact allows the detection via a line geometric treatment [7, 10]. Patch detection in case of general spline surfaces is not yet solved successfully. While the patch generation is at most invariant with respect to affine transformation, the normal congruence of the patch is a Euclidean concept. Therefore, we can expect that connections between the patch and its congruence turn to be rather complicated already for (algebraic) Bézier surfaces.

The analysis of the patch’s normal congruence is only the first step of the far more difficult investigation of a reflection or refraction congruence with respect to a given patch. This problem belongs to geometric optics which would have explicit industrial applications but is not the topic of this paper. We restrict ourselves to an analysis of the normal congruence of a TP- Bézier patch [4, 7, 10].

A Bézier curve was named after Pierre Bézier, an engineer and mathematician who developed this method of computer drawing in late 1960s while working for the car manufacturer Règie Renault [3].

Derivatives and normal vectors of these curves are important issues in geometric modeling and computer graphics [10]. The first derivative of a degree n polynomial Bézier curve can be expressed as a degree $n-1$ polynomial Bézier curve. For a tensor-product Bézier patch of degree m in r -parameter and n in s -parameter, the partial derivatives with respect to each parameter r or s are also tensor-product Bézier patches of degree $m-1$ in r and n in s or m in r and $n-1$ in s . The normal direction can be obtained as the cross product of the partial derivative respect to r and the partial derivative respect to s , its degree is $(2m-1) \times (2n-1)$.

2. Differential geometry of TP- Bézier patches

A tensor product Bézier patch Φ of degree (m, n) and $P_{i,j}$ control points can be defined as follows:

$$X^{m,n}(u,v) = \sum_{i=0}^m \sum_{j=0}^n B_i^m(u) B_j^n(v) P_{i,j} ; u,v \in [0,1] \times [0,1], \quad (1)$$

whereby $B_i^m(u)$ and $B_j^n(v)$ denote the Bernstein polynomials of degree m and n in u and v parameters respectively. We will assume that the set of control points is chosen such that

$$X_u \times X_v \neq 0 \quad \forall (u,v) \in [0,1] \times [0,1]. \quad (2)$$

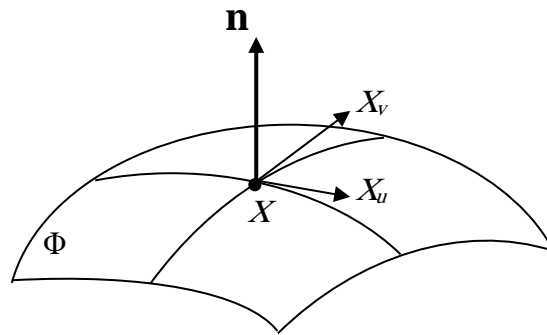


Figure 1. A Parametric surface patch.

We want to calculate the first fundamental form:

$$ds^2 = E du^2 + 2F du dv + G dv^2, \quad (3)$$

of that patch, that means we have to calculate

$$E = X_u X_u, \quad F = X_u X_v, \quad G = X_v X_v, \quad (4)$$

where

$$X_u = \frac{\partial}{\partial u} X^{m,n}(u,v) = m \sum_{j=0}^n \sum_{i=0}^{m-1} B_i^{m-1}(u) B_j^n(v) \Delta^{1,0} P_{i,j},$$

$$X_v = \frac{\partial}{\partial v} X^{m,n}(u,v) = n \sum_{i=0}^m \sum_{j=0}^{n-1} B_j^{n-1}(v) B_i^m(u) \Delta^{0,1} P_{i,j}. \quad (5)$$

The partials X_u and X_v at a point X span the tangent plane to the patch at X .

Let Y be any point on this plane. Then

$$\det[Y - X, X_u, X_v] = 0, \quad (6)$$

is the implicit equation of the tangent plane. The parametric equation is

$$Y(u,v) = X + \lambda X_u + \mu X_v ; \lambda, \mu \in \mathfrak{R}. \quad (7)$$

The normalized normal

$$\mathbf{n} = \frac{\mathbf{X}_u \times \mathbf{X}_v}{\|\mathbf{X}_u \times \mathbf{X}_v\|}, \quad (8)$$

together with the unnormalized vectors X_u and X_v form a local coordinate system, a frame, at the point $X \in \Phi$ (see Fig. 2).

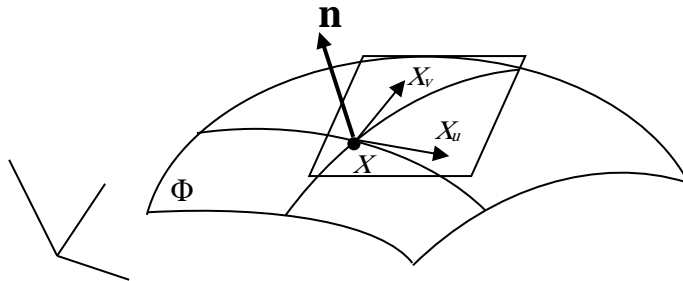


Figure 2. The local frame and the tangent plane.

From curve theory [7, 8], we know that its curvature κ is defined by $t' = \kappa \mathbf{m}$.

We now calculate the second fundamental form of Φ ,

$$\kappa \cos \phi ds^2 = L du^2 + 2M du dv + N dv^2, \quad (9)$$

whereby ϕ is the angle between the main normal m of the curve $c \subset \Phi$ and the surface normal n and κ its curvature at the point X under consideration, as illustrated in Fig. 3.

Here, L , M and N are defined as follows:

$$\begin{aligned} L &= \mathbf{n} X_{uu}, \\ M &= \mathbf{n} X_{uv}, \\ N &= \mathbf{n} X_{vv}. \end{aligned} \quad (10)$$

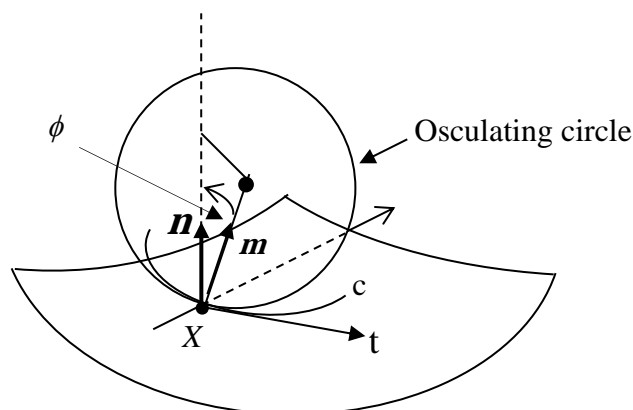


Figure 3. Osculating circle.

The 2nd derivatives are the expressions, since

$$\begin{aligned} \frac{\partial^r}{\partial u^r} X^{m,n}(u,v) &= \frac{m!}{(m-r)!} \sum_{j=0}^n \sum_{i=0}^{m-r} B_i^{m-r}(u) B_j^n(v) \Delta^{r,0} P_{i,j}, \\ \frac{\partial^s}{\partial v^s} X^{m,n}(u,v) &= \frac{n!}{(n-s)!} \sum_{i=0}^m \sum_{j=0}^{n-s} B_j^{n-s}(v) B_i^m(u) \Delta^{0,s} P_{i,j}, \\ \frac{\partial^{r+s}}{\partial u^r \partial v^s} X^{m,n}(u,v) &= \frac{m!n!}{(m-r)!(n-s)!} \sum_{i=0}^{m-r} \sum_{j=0}^{n-s} B_i^{m-r}(u) B_j^{n-s}(v) \Delta^{r,s} P_{i,j}, \end{aligned} \quad (11)$$

where

$$\begin{aligned} \Delta^{r,0} P_{i,j} &= \Delta^{r-1,0} P_{i+1,j} - \Delta^{r-1,0} P_{i,j}, \\ \Delta^{0,s} P_{i,j} &= \Delta^{0,s-1} P_{i,j+1} - \Delta^{0,s-1} P_{i,j}. \end{aligned} \quad (12)$$

Now, we get

$$\begin{aligned} X_{uu} &= \frac{\partial^2}{\partial u^2} X^{m,n}(u,v) = \frac{m!}{(m-2)!} \sum_{j=0}^n \sum_{i=0}^{m-2} B_i^{m-2}(u) B_j^n(v) \Delta^{2,0} P_{i,j}, \\ X_{uv} &= \frac{\partial^2}{\partial u \partial v} X^{m,n}(u,v) = \frac{m!n!}{(m-1)!(n-1)!} \sum_{i=0}^{m-1} \sum_{j=0}^{n-1} B_i^{m-1}(u) B_j^{n-1}(v) \Delta^{1,1} P_{i,j}, \\ X_{vv} &= \frac{\partial^2}{\partial v^2} X^{m,n}(u,v) = \frac{n!}{(n-2)!} \sum_{i=0}^m \sum_{j=0}^{n-2} B_j^{n-2}(v) B_i^m(u) \Delta^{0,2} P_{i,j}, \end{aligned} \quad (13)$$

whereby

$$\begin{aligned} \Delta^{1,1} P_{i,j} &= (P_{i+1,j+1} - P_{i+1,j}) - (P_{i,j+1} - P_{i,j}), \\ \Delta^{2,0} P_{i,j} &= \Delta^{1,0} P_{i+1,j} - \Delta^{1,0} P_{i,j}, \quad \Delta^{1,0} P_{i,j} = P_{i+1,j} - P_{i,j}, \\ \Delta^{0,2} P_{i,j} &= \Delta^{0,1} P_{i,j+1} - \Delta^{0,1} P_{i,j}, \quad \Delta^{0,1} P_{i,j} = P_{i,j+1} - P_{i,j}. \end{aligned} \quad (14)$$

So, for $\phi=0$, the osculating plane of the curve is perpendicular to the patch tangent plane at the point X . The curvature of such a curve is called the normal curvature of the surface patch at X and given by

$$\kappa_0 = \frac{2^{nd} \text{ fundamentd form}}{1^{st} \text{ fundamentd form}}. \quad (15)$$

Now, we can calculate principal curvature lines through a fixed point $X \in \Phi$, which belong to directions du/dv , where κ_0 is extremal. Setting $\lambda = dv/du$, we can write Eq. (15) as

$$\kappa_0(\lambda) = \frac{L + 2M\lambda + N\lambda^2}{E + 2F\lambda + G\lambda^2}, \quad (16)$$

such that $\kappa = \kappa_0(\lambda)$ is a rational quadratic function in λ . The extreme values κ_1 and κ_2 of $\kappa(\lambda)$ occur at the roots λ_1 and λ_2 of

$$\det \begin{bmatrix} \lambda^2 & -\lambda & 1 \\ E & F & G \\ L & M & N \end{bmatrix} = 0 \quad (17)$$

$$\begin{aligned} \Rightarrow \lambda^2 (FN - MG) + \lambda (EN - LG) + (EM - LF) &= 0 \\ \Rightarrow \lambda_1, \lambda_2 &= \frac{1}{2(FN - MG)} \left\{ (LG - EN) \pm \sqrt{(EN - LG)^2 - 4(FN - MG)(EM - LF)} \right\}. \end{aligned} \quad (18)$$

Also, we can calculate the Gaussian and mean curvatures of the patch as follows:

$$\begin{aligned} \kappa_1 \kappa_2 &= \frac{LN - M^2}{EG - F^2}, \\ \kappa_1 + \kappa_2 &= \frac{NE - 2MF + LG}{EG - F^2}. \end{aligned} \quad (19)$$

Where, the term $K = \kappa_1 \kappa_2$ is called Gaussian curvature, while $H = \frac{1}{2}(\kappa_1 + \kappa_2)$ is called mean curvature. Note that, both κ_1 and κ_2 change sign if the normal n is reversed, but K is not affected by such a reversal.

3. Motivation and results

In case of bicubic patch ($m=n=3$), we receive for $X_u, X_v, X_{uu}, X_{uv}, X_{vv}$, where

$$X_u = 3 \sum_{j=0}^3 \sum_{i=0}^2 B_i^2(u) B_j^3(v) \Delta^{1,0} P_{i,j} = 3 \sum_{j=0}^3 \sum_{i=0}^2 B_i^2(u) B_j^3(v) (P_{i+1,j} - P_{i,j}),$$

$$X_v = 3 \sum_{i=0}^3 \sum_{j=0}^2 B_j^2(v) B_i^3(u) \Delta^{0,1} P_{i,j} = 3 \sum_{i=0}^3 \sum_{j=0}^2 B_j^2(v) B_i^3(u) (P_{i,j+1} - P_{i,j}),$$

$$X_{uu} = 6 \sum_{j=0}^3 \sum_{i=0}^1 B_i^1(u) B_j^3(v) \Delta^{2,0} P_{i,j} = 6 \sum_{j=0}^3 \sum_{i=0}^1 B_i^1(u) B_j^2(v) (P_{2,j} - 2P_{1,j} + P_{0,j}),$$

$$X_{vv} = 6 \sum_{i=0}^3 \sum_{j=0}^1 B_j^1(v) B_i^3(u) \Delta^{0,2} P_{i,j} = 6 \sum_{i=0}^3 \sum_{j=0}^1 B_j^1(v) B_i^3(u) (P_{i,2} - 2P_{i,1} + P_{i,0}),$$

$$X_{uv} = 9 \sum_{i=0}^2 \sum_{j=0}^2 B_i^2(u) B_j^2(v) \Delta^{1,1} P_{i,j} = 9 \sum_{i=0}^2 \sum_{j=0}^2 B_i^2(u) B_j^2(v) [(P_{i+1,j+1} - P_{i+1,j}) - (P_{i,j+1} - P_{i,j})].$$

That means: the Plücker coordinates $(X_u \times X_v; X \times (X_u \times X_v))$ of the normal congruence of the patch are functions of order 14 because of that high degree, it seems not to be of practical use to calculate the focal points of the normal vectors of the patch in general. We apply these calculations to a biquadratic patch Φ :

Specializing $m = n = 2$ we receive

$$X_u = 2 \sum_{j=0}^2 \sum_{i=0}^1 B_i^1(u) B_j^2(v) \Delta^{1,0} P_{i,j} = 2 \sum_{j=0}^2 \sum_{i=0}^1 B_i^1(u) B_j^2(v) (P_{i+1,j} - P_{i,j}),$$

$$X_v = 2 \sum_{i=0}^2 \sum_{j=0}^1 B_j^1(v) B_i^2(u) \Delta^{0,1} P_{i,j} = 2 \sum_{i=0}^2 \sum_{j=0}^1 B_j^1(v) B_i^2(u) (P_{i,j+1} - P_{i,j}),$$

$$X_{uu} = 2 \sum_{j=0}^2 B_j^2(v) \Delta^{2,0} P_{i,j} = 2 \sum_{j=0}^2 B_j^2(v) (P_{2,j} - 2P_{1,j} + P_{0,j}); i = 0,$$

$$X_{vv} = 2 \sum_{i=0}^2 B_i^2(u) \Delta^{0,2} P_{i,j} = 2 \sum_{i=0}^2 B_i^2(u) (P_{i,2} - 2P_{i,1} + P_{i,0}); j = 0,$$

$$X_{uv} = 4 \sum_{i=0}^1 \sum_{j=0}^1 B_i^1(u) B_j^1(v) \Delta^{1,1} P_{i,j} = 4 \sum_{i=0}^1 \sum_{j=0}^1 B_i^1(u) B_j^1(v) [(P_{i+1,j+1} - P_{i+1,j}) - (P_{i,j+1} - P_{i,j})], \quad (20)$$

and the normal vector is

$$\mathbf{n}(u, v) = 4 \sum_{j=0}^2 \sum_{i=0}^1 \sum_{k=0}^2 \sum_{l=0}^1 B_i^1(u) B_k^2(u) B_l^1(v) B_j^2(v) \nabla(P_{i,j} \times P_{k,l}), \quad (21)$$

whereby, we abbreviated $\Delta^{1,0} P_{i,j} \times \Delta^{0,1} P_{i,j}$ by $\nabla(P_{i,j} \times P_{k,l})$.

Now, we are able to calculate the first and the second fundamental forms and then, by applying Eq. (18) we get the lines of curvature of this patch.

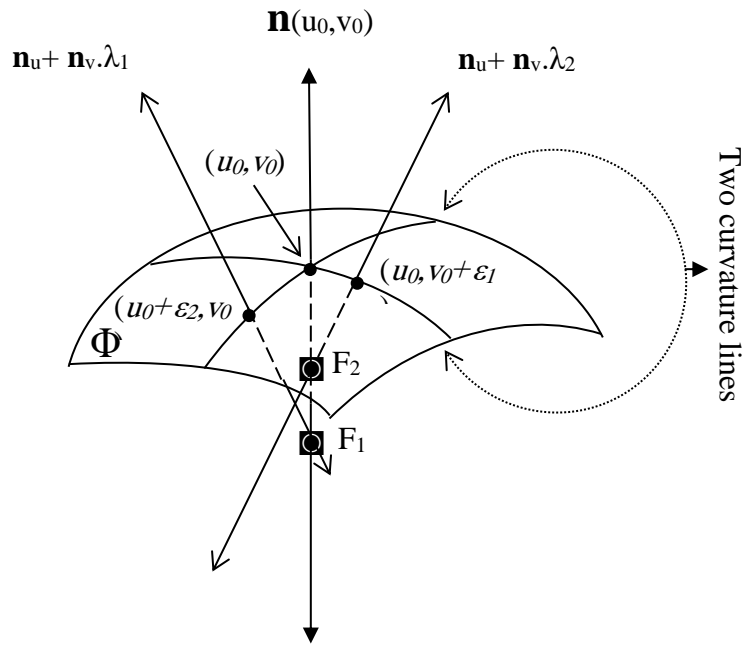


Figure 4. Curvature lines of the patch and two focal points, F_1 and F_2 .

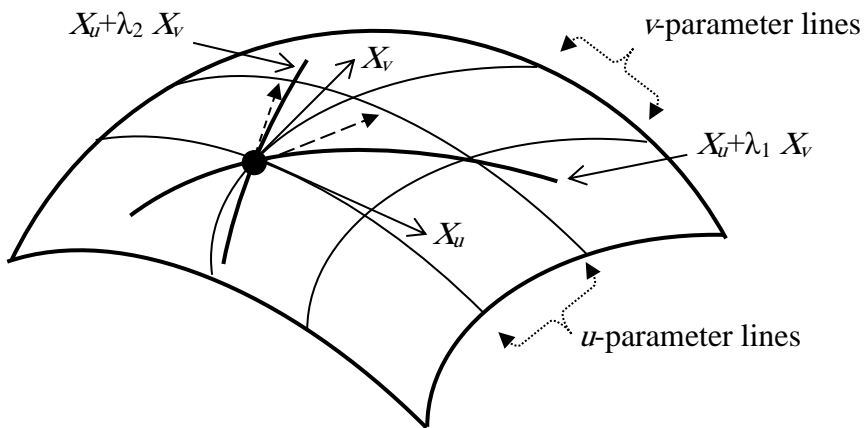


Figure 5. Parameter lines on the patch.

Note that, along the principal curvature lines, the normals fulfill developable surfaces, therefore, \mathbf{n} intersects \mathbf{n}_1 (in focal point F_1) and \mathbf{n}_2 (in focal point F_2), whereby

$$\mathbf{n}_1 := \mathbf{n}_u + \lambda_1 \mathbf{n}_v, \quad \mathbf{n}_2 := \mathbf{n}_u + \lambda_2 \mathbf{n}_v, \quad (22)$$

and

$$\{\mathbf{n}(u, v), \mathbf{n}_u(u, v), \mathbf{n}_v(u, v)\}, \quad (23)$$

span a plane which is tangent to Klein model M_4^2 and the intersection between M_4^2 and focal plane leads to join of lines, and we have

$$(\mathbf{n}(u, v) + \eta \mathbf{n}_u(u, v) + \beta \mathbf{n}_v(u, v)) \in M_4^2,$$

so, we get

$$\begin{aligned} & \langle \mathbf{n} + \eta \mathbf{n}_u + \beta \mathbf{n}_v, \mathbf{n} + \eta \mathbf{n}_u + \beta \mathbf{n}_v \rangle = 0 \\ \Rightarrow & \langle \mathbf{n}, \mathbf{n} \rangle + 2\eta \langle \mathbf{n}, \mathbf{n}_u \rangle + 2\beta \langle \mathbf{n}, \mathbf{n}_v \rangle + 2\eta\beta \langle \mathbf{n}_u, \mathbf{n}_v \rangle + \eta^2 \langle \mathbf{n}_u, \mathbf{n}_u \rangle + \beta^2 \langle \mathbf{n}_v, \mathbf{n}_v \rangle = 0, \end{aligned} \quad (24)$$

because $\langle \mathbf{n}, \mathbf{n} \rangle = 0$ for all u, v we get

$$\begin{aligned} & 2\eta\beta \langle \mathbf{n}_u, \mathbf{n}_v \rangle + \eta^2 \langle \mathbf{n}_u, \mathbf{n}_u \rangle + \beta^2 \langle \mathbf{n}_v, \mathbf{n}_v \rangle = 0 \\ \Rightarrow & \frac{\beta^2}{\eta^2} \langle \mathbf{n}_v, \mathbf{n}_v \rangle + 2 \frac{\beta}{\eta} \langle \mathbf{n}_u, \mathbf{n}_v \rangle + \langle \mathbf{n}_u, \mathbf{n}_u \rangle = 0. \end{aligned} \quad (25)$$

Setting $\frac{\beta}{\eta} = \frac{dv}{du} = \lambda$, we can get the two direction coefficients (λ_1, λ_2) which are known as

torsal directions.

Using Eqs. (4), we get E, F and G , that follows:

$$\begin{aligned} E &= \left(2 \sum_{j=0}^2 \sum_{i=0}^1 B_i^1(u) B_j^2(v) (P_{i+1,j} - P_{i,j}) \right)^2 \\ &= 4 \left((1-u)(1-v)^2 (P_{10} - P_{00}) + 2v(1-u)(1-v)(P_{11} - P_{01}) \right. \\ &\quad \left. + v^2(1-u)(P_{12} - P_{02}) + u(1-v)^2 (P_{20} - P_{10}) \right. \\ &\quad \left. + 2uv(1-v)(P_{21} - P_{11}) + uv^2 (P_{22} - P_{12}) \right)^2, \\ F &= 4 \left(\sum_{j=0}^2 \sum_{i=0}^1 B_i^1(u) B_j^2(v) (P_{i+1,j} - P_{i,j}) \right) \left(\sum_{i=0}^2 \sum_{j=0}^1 B_j^1(v) B_i^2(u) (P_{i,j+1} - P_{i,j}) \right) \\ &= 4 \left((1-u)(1-v)^2 (P_{10} - P_{00}) + 2v(1-u)(1-v)(P_{11} - P_{01}) \right. \\ &\quad \left. + v^2(1-u)(P_{12} - P_{02}) + u(1-v)^2 (P_{20} - P_{10}) \right. \\ &\quad \left. + 2uv(1-v)(P_{21} - P_{11}) + uv^2 (P_{22} - P_{12}) \right) \\ &\quad \cdot \left((1-v)(1-u)^2 (P_{01} - P_{00}) + 2u(1-u)(1-v)(P_{11} - P_{10}) \right. \\ &\quad \left. + u^2(1-v)(P_{21} - P_{20}) + v(1-u)^2 (P_{02} - P_{01}) \right. \\ &\quad \left. + 2uv(1-u)(P_{12} - P_{11}) + u^2v (P_{22} - P_{21}) \right), \end{aligned}$$

and

$$\begin{aligned}
G &= \left(2 \sum_{i=0}^2 \sum_{j=0}^1 B_j^1(v) B_i^2(u) (P_{i,j+1} - P_{i,j}) \right)^2 \\
&= 4 \left((1-v)(1-u)^2 (P_{01} - P_{00}) + 2u(1-u)(1-v)(P_{11} - P_{10}) \right. \\
&\quad \left. + u^2(1-v)(P_{21} - P_{20}) + v(1-u)^2 (P_{02} - P_{01}) \right. \\
&\quad \left. + 2uv(1-u)(P_{12} - P_{11}) + u^2v (P_{22} - P_{21}) \right)^2 .
\end{aligned}$$

Also, from Eqs. (10), we get L , M and N that follows:

$$\begin{aligned}
L &= \mathbf{n} \left(2 \sum_{j=0}^2 B_j^2(v) (P_{2,j} - 2P_{1,j} + P_{0,j}) \right) \\
&= 2\mathbf{n} \left((1-v)^2 (P_{00} - 2P_{10} + P_{20}) + 2v(1-v)(P_{01} - 2P_{11} + P_{21}) + v^2 (P_{02} - 2P_{12} + P_{22}) \right),
\end{aligned}$$

$$\begin{aligned}
M &= \mathbf{n} \left(4 \sum_{i=0}^1 \sum_{j=0}^1 B_i^1(u) B_j^1(v) (P_{i+1,j+1} - P_{i+1,j} - P_{i,j+1} + P_{i,j}) \right) \\
&= 4\mathbf{n} \left((1-u)(1-v)(P_{00} - P_{01} - P_{10} - P_{11}) + v(1-u)(P_{01} - P_{02} - P_{11} + P_{12}) \right. \\
&\quad \left. + u(1-v)(P_{10} - P_{11} - P_{20} + P_{21}) + uv(P_{11} - P_{12} - P_{21} + P_{22}) \right),
\end{aligned}$$

and

$$\begin{aligned}
N &= \mathbf{n} \left(2 \sum_{i=0}^2 B_i^2(u) (P_{i,2} - 2P_{i,1} + P_{i,0}) \right) \\
&= 2\mathbf{n} \left((1-u)^2 (P_{00} - 2P_{01} + P_{02}) + 2u(1-u)(P_{10} - 2P_{11} + P_{12}) + u^2 (P_{20} - 2P_{21} + P_{22}) \right).
\end{aligned}$$

After using Eq. (18) we can calculate the two direction coefficients λ_1, λ_2 .

Now, we calculate the two direction coefficients λ_1, λ_2 at the four corner points of the patch, P_{00}, P_{02}, P_{20} and P_{22} , where at these points the parameters u and v are $(0,0), (0,1), (1,0)$ and $(1,1)$, respectively.

At the first, let us calculate E, F, G, L, M and N at these points as follows:

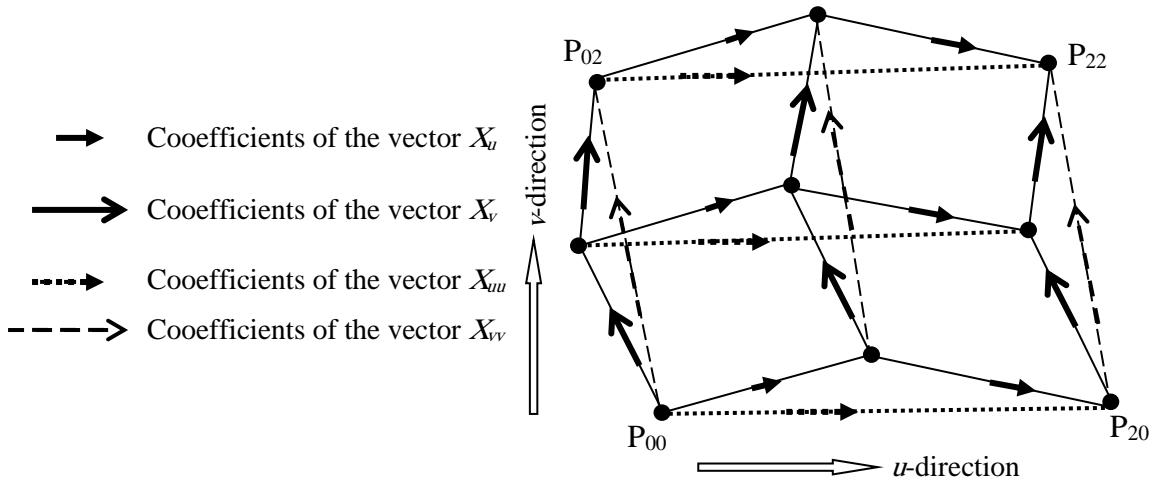


Figure 6. The coefficients of the partial derivatives.

Setting, $\Delta P_{ijkl} = (P_{ij} - P_{kl})$, to simplify our calculations.

- At the point P_{00} where $(u, v) = (0,0)$:

$$\begin{aligned}
 E &= 4(\Delta P_{1000})^2, \quad F = 4(\Delta P_{0100})(\Delta P_{1000}) \text{ and } G = 4(\Delta P_{0100})^2, \\
 \mathbf{n} &= 4(\Delta P_{1000} \times \Delta P_{0100}), \\
 L &= 8 \det(\Delta P_{1000}, \Delta P_{0100}, \Delta P_{2010}), \\
 M &= 16 \det(\Delta P_{1000}, \Delta P_{0100}, \Delta P_{1101}) \text{ or } M = 16 \det(\Delta P_{1000}, \Delta P_{0100}, \Delta P_{1110}), \\
 N &= 8 \det(\Delta P_{1000}, \Delta P_{0100}, \Delta P_{0201}).
 \end{aligned}$$

- At the point P_{02} where $(u, v) = (0,1)$:

$$\begin{aligned}
 E &= 4(\Delta P_{1202})^2, \quad F = 4(\Delta P_{0201})(\Delta P_{1202}) \text{ and } G = 4(\Delta P_{0201})^2. \\
 \mathbf{n} &= 4(\Delta P_{1202} \times \Delta P_{0201}), \\
 L &= 8 \det(\Delta P_{1202}, \Delta P_{0201}, \Delta P_{2212}), \\
 M &= 16 \det(\Delta P_{1202}, \Delta P_{0201}, \Delta P_{0111}) \text{ or } M = 16 \det(\Delta P_{1202}, \Delta P_{0201}, \Delta P_{1211}), \\
 N &= 8 \det(\Delta P_{1202}, \Delta P_{0201}, \Delta P_{0001}).
 \end{aligned}$$

- At the point P_{20} where $(u, v) = (1,0)$:

$$\begin{aligned}
 E &= 4(\Delta P_{2010})^2, \quad F = 4(\Delta P_{2010})(\Delta P_{2120}) \text{ and } G = 4(\Delta P_{2120})^2. \\
 \mathbf{n} &= 4(\Delta P_{2010} \times \Delta P_{2120}), \\
 L &= 8 \det(\Delta P_{2010}, \Delta P_{2120}, \Delta P_{0010}), \\
 M &= 16 \det(\Delta P_{2010}, \Delta P_{2120}, \Delta P_{1011}) \text{ or } M = 16 \det(\Delta P_{2010}, \Delta P_{2120}, \Delta P_{2111}), \\
 N &= 8 \det(\Delta P_{2010}, \Delta P_{2120}, \Delta P_{2221}).
 \end{aligned}$$

- At the point P_{22} where $(u, v) = (1, 1)$:

$$\begin{aligned}
 E &= 4(\Delta P_{2212})^2, \quad F = 4(\Delta P_{2212})(\Delta P_{2221}) \text{ and } G = 4(\Delta P_{2221})^2. \\
 \mathbf{n} &= 4(\Delta P_{2212} \times \Delta P_{2221}), \\
 L &= 8 \det(\Delta P_{2212}, \Delta P_{2221}, \Delta P_{0212}), \\
 M &= 16 \det(\Delta P_{2212}, \Delta P_{2221}, \Delta P_{1121}) \text{ or } M = 16 \det(\Delta P_{2212}, \Delta P_{2221}, \Delta P_{1112}), \\
 N &= 8 \det(\Delta P_{2212}, \Delta P_{2221}, \Delta P_{2021}).
 \end{aligned}$$

If we use the following symbol, we can get simple equations:

$${}^{efgh} \sum_{mnop} {}^{ijkl} \Delta P = \det(\Delta P_{efgh}, \Delta P_{ijkl}, \Delta P_{mnop}).$$

Now, we are in a position to calculate the quantities λ_1 and λ_2 which are define directions in u,v-plane at each control corner point as follows:

At the point P_{00} :

$$\begin{aligned}
 \lambda_1, \lambda_2 &= \\
 &\left\{ 32 \left[(\Delta P_{0100})^2 \sum_{2010}^{0100} \Delta P - (\Delta P_{1000})^2 \sum_{0201}^{0100} \Delta P \right] \pm \left[32 \left((\Delta P_{1000})^2 \sum_{0201}^{0100} \Delta P \right. \right. \right. \\
 &\left. \left. - (\Delta P_{0100})^2 \sum_{2010}^{0100} \Delta P \right) \right]^2 - 4 \left((32)^2 \left((\Delta P_{0100})(\Delta P_{1000}) \sum_{0201}^{0100} \Delta P - 2 (\Delta P_{0100})^2 \sum_{1101}^{0100} \Delta P \right) \right. \\
 &\left. \left. \left(2 (\Delta P_{1000})^2 \sum_{1101}^{0100} \Delta P - (\Delta P_{1000})(\Delta P_{0100}) \sum_{2010}^{0100} \Delta P \right) \right] \right\}^{1/2} \\
 &/ 64 \left[(\Delta P_{0100})(\Delta P_{1000}) \sum_{0201}^{0100} \Delta P - 2 (\Delta P_{0100})^2 \sum_{1101}^{0100} \Delta P \right].
 \end{aligned}$$

At the point P_{02} :

$$\begin{aligned}
 \lambda_1, \lambda_2 &= \\
 &\left\{ 32 \left[(\Delta P_{0201})^2 \sum_{2212}^{0201} \Delta P - (\Delta P_{1202})^2 \sum_{0001}^{0201} \Delta P \right] \pm \left[32 \left((\Delta P_{1202})^2 \sum_{0001}^{0201} \Delta P \right. \right. \right. \\
 &\left. \left. - (\Delta P_{0201})^2 \sum_{2212}^{0201} \Delta P \right) \right]^2 - 4 \left((32)^2 \left((\Delta P_{0201})(\Delta P_{1202}) \sum_{0001}^{0201} \Delta P - 2 (\Delta P_{0201})^2 \sum_{0111}^{0201} \Delta P \right) \right. \\
 &\left. \left. \left(2 (\Delta P_{1202})^2 \sum_{0111}^{0201} \Delta P - (\Delta P_{0201})(\Delta P_{1202}) \sum_{2212}^{0201} \Delta P \right) \right] \right\}^{1/2} \\
 &/ 64 \left[(\Delta P_{0201})(\Delta P_{1202}) \sum_{0001}^{0201} \Delta P - 2 (\Delta P_{0201})^2 \sum_{0111}^{0201} \Delta P \right].
 \end{aligned}$$

At the point P_{20} :

$$\lambda_1, \lambda_2 = \left\{ 32 \left[(\Delta P_{2120})^2 \sum_{0010}^{2120} \Delta P - (\Delta P_{2010})^2 \sum_{1011}^{2120} \Delta P \right] \pm \left[32 \left((\Delta P_{2010})^2 \sum_{1011}^{2120} \Delta P - (\Delta P_{2120})^2 \sum_{0010}^{2120} \Delta P \right)^2 - 4 \left((32)^2 \left((\Delta P_{2010})(\Delta P_{2120}) \sum_{2221}^{2120} \Delta P - 2(\Delta P_{2120})^2 \sum_{1011}^{2120} \Delta P \right) \right) \right]^{1/2} \right\} / 64 \left[(\Delta P_{2010})(\Delta P_{2120}) \sum_{2221}^{2120} \Delta P - 2(\Delta P_{2120})^2 \sum_{1011}^{2120} \Delta P \right]$$

At the point P_{22} :

$$\lambda_1, \lambda_2 = \left\{ 32 \left[(\Delta P_{2221})^2 \sum_{0212}^{2221} \Delta P - (\Delta P_{2212})^2 \sum_{1121}^{2221} \Delta P \right] \pm \left[32 \left((\Delta P_{2212})^2 \sum_{1121}^{2221} \Delta P - (\Delta P_{2221})^2 \sum_{0212}^{2221} \Delta P \right)^2 - 4 \left((32)^2 \left((\Delta P_{2212})(\Delta P_{2221}) \sum_{2021}^{2221} \Delta P - 2(\Delta P_{2221})^2 \sum_{1121}^{2221} \Delta P \right) \right) \right]^{1/2} \right\} / 64 \left[(\Delta P_{2212})(\Delta P_{2221}) \sum_{2021}^{2221} \Delta P - 2(\Delta P_{2221})^2 \sum_{1121}^{2221} \Delta P \right]$$

Also, from Eq. (16) we can calculate the two principal curvatures at each corner control point and then, we get two radii of curvature at these points.

The following figures illustrate the coefficient vectors of two direction formulas at the four corner control points of the bi-quadratic TP Bézier patch.

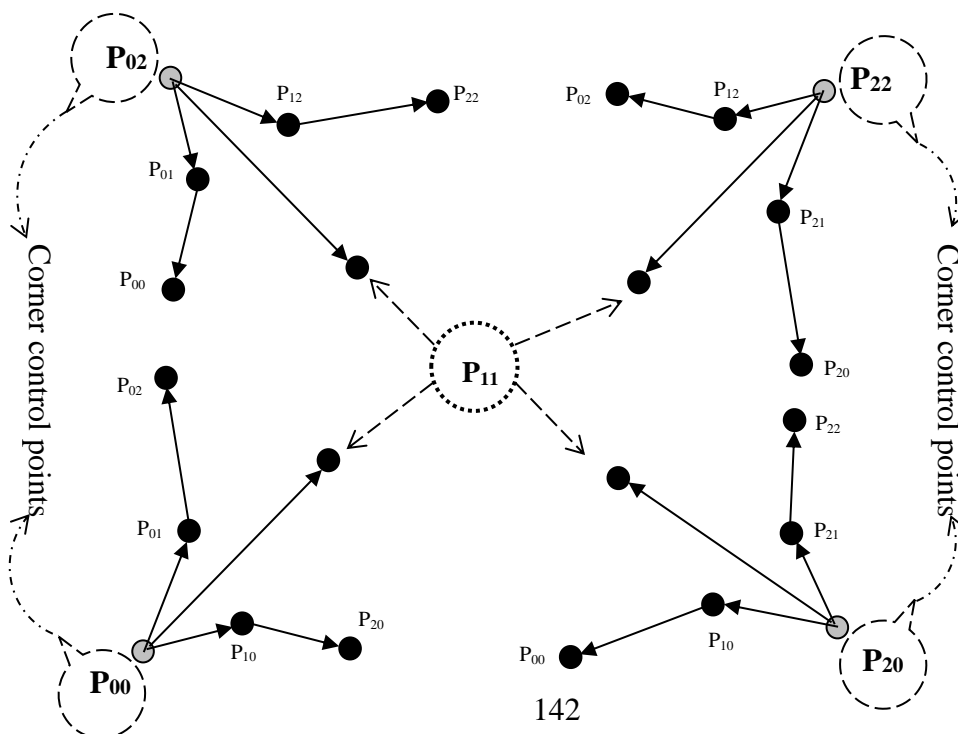


Figure 7. Coefficient vectors of the first and second fundamental quantities.

The normal vector to the TP Bèzier Patch is denoted by

$$N = mn \sum_{j=0}^n \sum_{i=0}^{m-1} \sum_{k=0}^m \sum_{l=0}^{n-1} B_i^{m-1}(u) B_k^m(u) B_j^{n-1}(v) B_l^n(v) (\Delta^{1,0} P_{i,j} \times \Delta^{0,1} P_{k,l}).$$

For the biquadratic Patch; $m=n=2$, the normal vector becomes

$$N = 4 \sum_{j=0}^2 \sum_{i=0}^1 \sum_{k=0}^2 \sum_{l=0}^1 B_i^1(u) B_k^2(u) B_j^1(v) B_l^2(v) (\Delta^{1,0} P_{i,j} \times \Delta^{0,1} P_{k,l}).$$

Taking derivatives, we get

$$N_u = \frac{\partial N}{\partial u} = 4 \sum_{j=0}^2 \sum_{l=0}^1 \left[\frac{\partial}{\partial u} \sum_{i=0}^1 \sum_{k=0}^2 B_i^1(u) B_k^2(u) (\Delta^{1,0} P_{i,j} \times \Delta^{0,1} P_{k,l}) \right] B_j^2(v) B_l^1(v).$$

The bracketed term depends only on u, and we can apply the formula for the derivative of a Bèzier curve:

$$N_u = 8 \sum_{j=0}^2 \sum_{l=0}^1 \sum_{k=0}^1 B_k^1(u) B_l^1(v) B_j^2(v) \left[(\Delta^{2,0} P_{0,j} \times \Delta^{0,1} P_{k,l}) + (\Delta^{1,0} P_{0,j} \times \Delta^{1,1} P_{k,l}) \right]$$

by the same way, we have

$$N_v = 8 \sum_{i=0}^1 \sum_{k=0}^2 \sum_{j=0}^1 B_k^2(u) B_i^1(u) B_j^1(v) \left[(\Delta^{1,1} P_{i,j} \times \Delta^{0,1} P_{k,0}) + (\Delta^{1,0} P_{i,j} \times \Delta^{0,2} P_{k,0}) \right]$$

where

$$\begin{aligned} \Delta^{1,0} P_{i,j} &= P_{i+1,j} - P_{i,j} \quad , \quad \Delta^{0,1} P_{i,j} = P_{i,j+1} - P_{i,j} \quad , \\ \Delta^{0,2} P_{i,j} &= \Delta^{0,1} P_{i,j+1} - \Delta^{0,1} P_{i,j} \quad , \quad \Delta^{2,0} P_{i,j} = \Delta^{1,0} P_{i+1,j} - \Delta^{1,0} P_{i,j} \quad , \\ \Delta^{1,1} P_{i,j} &= (P_{i+1,j+1} - P_{i+1,j}) - (P_{i,j+1} - P_{i,j}). \end{aligned}$$

Let us calculate N_u and N_v at the four corner points, we get

At the point P_{00} where $(u, v) = (0,0)$:

$$N_u = 8 \{ [(P_{10} - P_{00}) \times (P_{11} - P_{10})] + [(P_{20} - P_{10}) \times (P_{01} - P_{00})] - 2[(P_{10} - P_{00}) \times (P_{01} - P_{00})] \},$$

$$N_v = 8\{[(P_{11} - P_{10}) \times (P_{01} - P_{00})] - [(P_{10} - P_{00}) \times (P_{01} - P_{00})] - [(P_{02} - P_{01}) \times (P_{10} - P_{00})]\}.$$

At the point P_{02} where $(u, v) = (0, 1)$:

$$N_u = 8\{[(P_{22} - P_{12}) \times (P_{02} - P_{01})] + [(P_{12} - P_{02}) \times (P_{12} - P_{11})] - 2[(P_{12} - P_{02}) \times (P_{02} - P_{01})]\},$$

$$N_v = 8\{[(P_{12} - P_{11}) \times (P_{01} - P_{00})] + [(P_{11} - P_{01}) \times (P_{02} - P_{01})] - [(P_{02} - P_{01}) \times (P_{01} - P_{00})] - [(P_{11} - P_{01}) \times (P_{01} - P_{00})]\}.$$

At the point P_{20} where $(u, v) = (1, 0)$:

$$N_u = 8\{[(P_{20} - P_{10}) \times (P_{11} - P_{10})] + [(P_{10} - P_{00}) \times (P_{21} - P_{20})] - 2[(P_{10} - P_{00}) \times (P_{11} - P_{10})]\},$$

$$N_v = 8\{[(P_{20} - P_{10}) \times (P_{22} - P_{21})] - [(P_{11} - P_{10}) \times (P_{21} - P_{20})] - [(P_{20} - P_{10}) \times (P_{21} - P_{20})]\}.$$

At the point P_{22} where $(u, v) = (1, 1)$:

$$N_u = 8\{[(P_{22} - P_{12}) \times (P_{12} - P_{11})] + [(P_{12} - P_{02}) \times (P_{22} - P_{21})] - 2[(P_{12} - P_{02}) \times (P_{12} - P_{11})]\},$$

$$N_v = 8\{[(P_{22} - P_{21}) \times (P_{21} - P_{20})] + [(P_{21} - P_{11}) \times (P_{22} - P_{21})] - [(P_{12} - P_{11}) \times (P_{21} - P_{20})] - [(P_{21} - P_{11}) \times (P_{21} - P_{20})]\}.$$

In the above equations, using $\Delta^{1,0} P_{i,j} = P_{i+1,j} - P_{i,j}$, $\Delta^{0,1} P_{i,j} = P_{i,j+1} - P_{i,j}$.

We have the normal vectors N_u and N_v in simple forms as follows:

At the point P_{00} where $(u, v) = (0, 0)$:

$$N_u = 8\{(\Delta^{1,0} P_{00} \times \Delta^{0,1} P_{10}) + (\Delta^{1,0} P_{10} \times \Delta^{0,1} P_{00}) - 2(\Delta^{1,0} P_{00} \times \Delta^{0,1} P_{00})\},$$

$$N_v = 8\{(\Delta^{0,1} P_{10} \times \Delta^{0,1} P_{00}) - (\Delta^{1,0} P_{00} \times \Delta^{0,1} P_{00}) - (\Delta^{0,1} P_{01} \times \Delta^{1,0} P_{00})\}.$$

At the point P_{02} where $(u, v) = (0, 1)$:

$$N_u = 8\{(\Delta^{1,0} P_{12} \times \Delta^{0,1} P_{01}) + (\Delta^{1,0} P_{02} \times \Delta^{0,1} P_{11}) - 2(\Delta^{1,0} P_{02} \times \Delta^{0,1} P_{01})\},$$

$$N_v = 8\{(\Delta^{0,1} P_{11} \times \Delta^{0,1} P_{00}) + (\Delta^{1,0} P_{01} \times \Delta^{0,1} P_{01}) - (\Delta^{0,1} P_{01} \times \Delta^{0,1} P_{00}) - (\Delta^{1,0} P_{01} \times \Delta^{0,1} P_{00})\}.$$

At the point P_{20} where $(u, v) = (1, 0)$:

$$N_u = 8 \left\{ \left(\Delta^{1,0} P_{10} \times \Delta^{0,1} P_{10} \right) + \left(\Delta^{1,0} P_{00} \times \Delta^{0,1} P_{20} \right) - 2 \left(\Delta^{1,0} P_{00} \times \Delta^{0,1} P_{10} \right) \right\},$$

$$N_v = 8 \left\{ \left(\Delta^{1,0} P_{10} \times \Delta^{0,1} P_{21} \right) - \left(\Delta^{0,1} P_{10} \times \Delta^{0,1} P_{20} \right) - \left(\Delta^{1,0} P_{10} \times \Delta^{0,1} P_{20} \right) \right\}.$$

At the point P_{22} where $(u, v) = (1, 1)$:

$$N_u = 8 \left\{ \left(\Delta^{1,0} P_{12} \times \Delta^{0,1} P_{11} \right) + \left(\Delta^{1,0} P_{02} \times \Delta^{0,1} P_{21} \right) - 2 \left(\Delta^{1,0} P_{02} \times \Delta^{0,1} P_{11} \right) \right\},$$

$$N_v = 8 \left\{ \left(\Delta^{0,1} P_{21} \times \Delta^{0,1} P_{20} \right) + \left(\Delta^{1,0} P_{11} \times \Delta^{0,1} P_{21} \right) - \left(\Delta^{0,1} P_{11} \times \Delta^{0,1} P_{20} \right) - \left(\Delta^{1,0} P_{11} \times \Delta^{0,1} P_{20} \right) \right\}.$$

Now, at each corner point on the patch, we can calculate the two focal points;

$$F_1 = N_u + \lambda_1 N_v \quad \text{and} \quad F_2 = N_u + \lambda_2 N_v.$$

Note that, λ_1 and λ_2 depend on the choice corner control point, so we have

At the point P_{00} where $(u, v) = (0, 0)$:

$$F_1 = 8 \left\{ \left[\left(\Delta^{1,0} P_{00} \times \Delta^{0,1} P_{10} \right) + \left(\Delta^{1,0} P_{10} \times \Delta^{0,1} P_{00} \right) - 2 \left(\Delta^{1,0} P_{00} \times \Delta^{0,1} P_{00} \right) \right] + \lambda_1 \left[\left(\Delta^{0,1} P_{10} \times \Delta^{0,1} P_{00} \right) - \left(\Delta^{1,0} P_{00} \times \Delta^{0,1} P_{00} \right) - \left(\Delta^{0,1} P_{01} \times \Delta^{1,0} P_{00} \right) \right] \right\},$$

$$F_2 = 8 \left\{ \left[\left(\Delta^{1,0} P_{00} \times \Delta^{0,1} P_{10} \right) + \left(\Delta^{1,0} P_{10} \times \Delta^{0,1} P_{00} \right) - 2 \left(\Delta^{1,0} P_{00} \times \Delta^{0,1} P_{00} \right) \right] + \lambda_2 \left[\left(\Delta^{0,1} P_{10} \times \Delta^{0,1} P_{00} \right) - \left(\Delta^{1,0} P_{00} \times \Delta^{0,1} P_{00} \right) - \left(\Delta^{0,1} P_{01} \times \Delta^{1,0} P_{00} \right) \right] \right\}.$$

At the point P_{02} where $(u, v) = (0, 1)$:

$$F_1 = 8 \left\{ \left[\left(\Delta^{1,0} P_{12} \times \Delta^{0,1} P_{01} \right) + \left(\Delta^{1,0} P_{02} \times \Delta^{0,1} P_{11} \right) - 2 \left(\Delta^{1,0} P_{02} \times \Delta^{0,1} P_{01} \right) \right] + \lambda_1 \left[\left(\Delta^{0,1} P_{11} \times \Delta^{0,1} P_{00} \right) + \left(\Delta^{1,0} P_{01} \times \Delta^{0,1} P_{01} \right) - \left(\Delta^{0,1} P_{01} \times \Delta^{0,1} P_{00} \right) - \left(\Delta^{1,0} P_{01} \times \Delta^{0,1} P_{00} \right) \right] \right\},$$

$$F_2 = 8 \left\{ \left[\left(\Delta^{1,0} P_{12} \times \Delta^{0,1} P_{01} \right) + \left(\Delta^{1,0} P_{02} \times \Delta^{0,1} P_{11} \right) - 2 \left(\Delta^{1,0} P_{02} \times \Delta^{0,1} P_{01} \right) \right] + \lambda_2 \left[\left(\Delta^{0,1} P_{11} \times \Delta^{0,1} P_{00} \right) + \left(\Delta^{1,0} P_{01} \times \Delta^{0,1} P_{01} \right) - \left(\Delta^{0,1} P_{01} \times \Delta^{0,1} P_{00} \right) - \left(\Delta^{1,0} P_{01} \times \Delta^{0,1} P_{00} \right) \right] \right\}.$$

At the point P_{20} where $(u, v) = (1, 0)$:

$$F_1 = 8 \left\{ \left[\left(\Delta^{1,0} P_{10} \times \Delta^{0,1} P_{10} \right) + \left(\Delta^{1,0} P_{00} \times \Delta^{0,1} P_{20} \right) - 2 \left(\Delta^{1,0} P_{00} \times \Delta^{0,1} P_{10} \right) \right] + \lambda_1 \left[\left(\Delta^{1,0} P_{10} \times \Delta^{0,1} P_{21} \right) - \left(\Delta^{0,1} P_{10} \times \Delta^{0,1} P_{20} \right) - \left(\Delta^{1,0} P_{10} \times \Delta^{0,1} P_{20} \right) \right] \right\},$$

$$F_2 = 8 \left\{ \left[\left(\Delta^{1,0} P_{10} \times \Delta^{0,1} P_{10} \right) + \left(\Delta^{1,0} P_{00} \times \Delta^{0,1} P_{20} \right) - 2 \left(\Delta^{1,0} P_{00} \times \Delta^{0,1} P_{10} \right) \right] + \lambda_2 \left[\left(\Delta^{1,0} P_{10} \times \Delta^{0,1} P_{21} \right) - \left(\Delta^{0,1} P_{10} \times \Delta^{0,1} P_{20} \right) - \left(\Delta^{1,0} P_{10} \times \Delta^{0,1} P_{20} \right) \right] \right\}.$$

At the point P_{22} where $(u, v) = (1, 1)$:

$$F_1 = 8 \left\{ \left[\left(\Delta^{1,0} P_{12} \times \Delta^{0,1} P_{11} \right) + \left(\Delta^{1,0} P_{02} \times \Delta^{0,1} P_{21} \right) - 2 \left(\Delta^{1,0} P_{02} \times \Delta^{0,1} P_{11} \right) \right] + \lambda_1 \right. \\ \left. \left[\left(\Delta^{0,1} P_{21} \times \Delta^{0,1} P_{20} \right) + \left(\Delta^{1,0} P_{11} \times \Delta^{0,1} P_{21} \right) - \left(\Delta^{0,1} P_{11} \times \Delta^{0,1} P_{20} \right) - \left(\Delta^{1,0} P_{11} \times \Delta^{0,1} P_{20} \right) \right] \right\},$$

$$F_2 = 8 \left\{ \left[\left(\Delta^{1,0} P_{12} \times \Delta^{0,1} P_{11} \right) + \left(\Delta^{1,0} P_{02} \times \Delta^{0,1} P_{21} \right) - 2 \left(\Delta^{1,0} P_{02} \times \Delta^{0,1} P_{11} \right) \right] + \lambda_2 \right. \\ \left. \left[\left(\Delta^{0,1} P_{21} \times \Delta^{0,1} P_{20} \right) + \left(\Delta^{1,0} P_{11} \times \Delta^{0,1} P_{21} \right) - \left(\Delta^{0,1} P_{11} \times \Delta^{0,1} P_{20} \right) - \left(\Delta^{1,0} P_{11} \times \Delta^{0,1} P_{20} \right) \right] \right\}.$$

4. Computational example

We have the control points for the biquadratic TP Bèzier patch, are denoted by the following matrix:

$$P_{i,j} = \begin{bmatrix} P_{00} & P_{01} & P_{02} \\ P_{10} & P_{11} & P_{12} \\ P_{20} & P_{21} & P_{22} \end{bmatrix} = \begin{bmatrix} (1,-1,0) & (2,-1,1) & (1,3,2) \\ (-3,2,1) & (0,2,1) & (1,0,3) \\ (-1,3,1) & (-2,2,1) & (3,-1,2) \end{bmatrix}; i, j=0,1,2.$$

The first and second fundamental quantities, two principal directions, two principal curvatures and two radii of curvature at the four corner points are:

At the point P_{00} :

$$E = 104, F = -12, G = 8, L = 88, M = 144 \text{ and } N = 112.$$

So, we get

$$\lambda_1 = 5.541, \lambda_2 = -1.158, \kappa(\lambda_1) = 23.646, \kappa(\lambda_2) = -0.669, \rho_1 = 0.042, \rho_2 = -1.495.$$

At the point P_{02} :

$$E = 40, F = -44, G = 72, L = -80, M = -176 \text{ and } N = 80.$$

So, we get

$$\lambda_1 = 0.691, \lambda_2 = -1.669, \kappa(\lambda_1) = -21.004, \kappa(\lambda_2) = 1.885, \rho_1 = -0.0428, \rho_2 = 0.530.$$

At the point P_{20} :

$$E = 20, F = -12, G = 8, L = 8, M = 0 \text{ and } N = -8.$$

So, we get

$$\lambda_1 = 1.761, \lambda_2 = 0.565, \kappa(\lambda_1) = -6.605, \kappa(\lambda_2) = 0.606, \rho_1 = -0.151, \rho_2 = 1.651.$$

At the point P_{22} :

$$E = 24, F = 48, G = 140, L = -160, M = -128 \text{ and } N = -88.$$

So, we get

$$\lambda_1 = -1.20, \lambda_2 = -0.280, \kappa(\lambda_1) = 0.186, \kappa(\lambda_2) = -11.761, \rho_1 = 5.391, \rho_2 = -0.085.$$

Also, we get the normal vectors in two directions u and v at the four corner control points as follows:

At the point P_{00} ; $N_u = (-40, -72, -32)$ and $N_v = (-32, -40, -80)$.

At the point P_{02} ; $N_u = (104, 16, 128)$ and $N_v = (-48, -8, 32)$.

At the point P_{20} ; $N_u = (8, -56, 176)$ and $N_v = (8, -16, -56)$.

At the point P_{22} ; $N_u = (32, -16, 48)$ and $N_v = (-8, 24, -8)$.

Finally, we are in a position to calculate the two focal points F_1 and F_2 at each corner control point as follows:

At the point P_{00} : $F_1 = (-217.312, -293.64, -475.28)$, $F_2 = (-2.944, -25.68, 60.64)$.

At the point P_{02} : $F_1 = (70.832, 10.472, 150.112)$, $F_2 = (184.112, 29.352, 74.592)$.

At the point P_{20} :
 $F_1 = (22.08, -84.16, 68.44)$, $F_2 = (12.52, -56.04, 135.36)$.

At the point P_{22} :
 $F_1 = (41.6, -44.8, 57.6)$, $F_2 = (34.24, -22.72, 50.24)$.

The following figure shows this patch

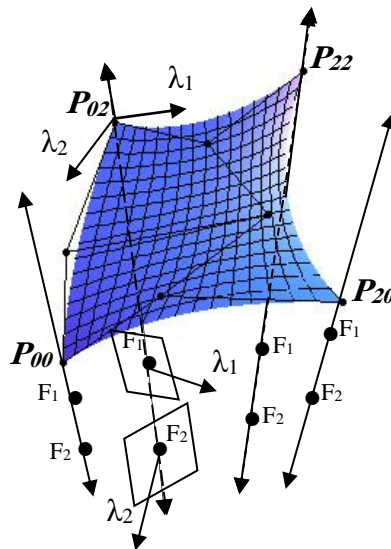


Figure 8. Bi-quadratic TP- Bézier patch with normals and their focal points at the four corner control points.

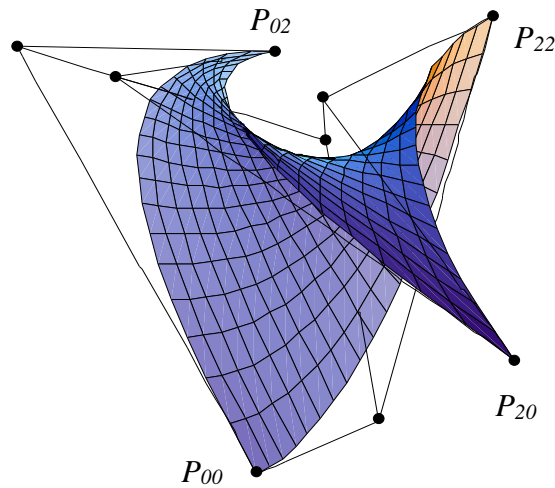


Figure 9. Bi-quadraticTP Bézier patch with four corner control points.

5. Conclusion

In five-dimensional real projective space (P^5), a new approach for tensor product (TP) Bézier patch representation has been introduced. Derivatives, normal vectors of Bézier patches and some of geometric properties of these patches have been discussed. Finally, a computational example of the two focal points of a normal of this patch is given and plotted.

Acknowledgment

The author is very grateful to Prof. Dr. Gunter Weiss at *Dresden University of Technology, Germany* for the useful suggestions and remarks on this work.

References

- [1] M. Khalifa Saad, Spacelike and timelike admissible Smarandache curves in pseudo-Galilean space, *Journal of the Egyptian Mathematical Society* 37 (2016) 416-423.
- [2] G. Aumann, Interpolation with developable Bézier patches, *Comp. Aided Geom. Des.* 8 (1991) 409-420.
- [3] G. Farin, *Curves and Surfaces for Computer Aided Geometric Design, A Practical Guide*, 5th edition. San Francisco, 2002.
- [4] I. Ginkel, J. Peters, G. Umlauf, Normals of subdivision surfaces and their control polyhedral, *Comp. Aided Geom. Des.* 24 (2007) 112-116.
- [5] I. Herman, *The Use of Projective Geometry in Computer Graphics*, Lecture Notes in Computer Science, Vol. 564, Springer, Berlin, 1991.
- [6] B. Juetter, M. Oberneder, A. Sinwel, On the existence of biharmonic tensor-product Bézier surface patches, *Comp. Aided Geom. Des.* 23 (2006) 612-615.
- [7] M. P. Do Carmo, *Differential Geometry of Curves and Surfaces*. Prentice Hall, Englewood Cliffs, NJ. 1976.
- [8] B. O'Neil, *Semi-Riemannian Geometry with Applications to Relativity*, Academic Press, London, 1983.
- [9] H. Pottmann, J. Wallner, *Computational Line Geometry*, Springer, Berlin, 2001.
- [10] G. Wang, T. W. Sederberg, T. Saito, Partial derivatives of rational Bézier surfaces, *Comp. Aided Geom. Des.* 14 (1997) 377-381.

هيئة التحرير

د. محمد عبد الرؤوف عابدين

رئيس هيئة التحرير

أستاذ مشارك، كلية الحاسب الآلي ونظم المعلومات، الجامعة الإسلامية بالمدينة المنورة، المملكة العربية السعودية.

أ.د. شمس الدين أحمد

مدير التحرير

الهندسة الصناعية، الجامعة الإسلامية بالمدينة المنورة، المملكة العربية السعودية.

أ.د. مصطفى يعقوب

الهندسة الكهربائية، جامعة أوتاوا،

أوتاوا، أونتاريو، كندا.

أ.د. فايز جبالي

الهندسة الكهربائية وهندسة الحاسبات، جامعة فيكتوريا،

فيكتوريا، بي سي، كندا.

أ.د. محمد قاري

كلية العلوم، جيولوجيا، الجامعة الإسلامية بالمدينة المنورة، المملكة العربية السعودية.

أ.د. أحمد العمري

كلية العلوم، الكيمياء، الجامعة الإسلامية بالمدينة المنورة، المملكة العربية السعودية.

أ.د. إبراهيم البديوي

كلية الحاسب الآلي ونظم المعلومات، جامعة الملك عبد العزيز جدة، المملكة العربية السعودية.

أ.د. محمد أوزان

الهندسة الميكانيكية، الجامعة الإسلامية بالمدينة المنورة المملكة العربية السعودية.

د. أحمد بدر الدين عبد الهادي الخضر

أستاذ مشارك، كلية الحاسب الآلي ونظم المعلومات، الجامعة الإسلامية بالمدينة المنورة، المملكة العربية السعودية.

سكرتير التحرير: عاصم محمود امين

قسم النشر: عمر بن حسن العبدلي

الهيئة الاستشارية

أ.د. حسين مفتاح

الهندسة الكهربائية وعلوم الكمبيوتر، جامعة أوتاوا، أوتاوا، أونتاريو، كندا، كرسي أبحاث في شبكات الاستشعار اللاسلكية أستاذ جامعي متميز، جامعة أوتاوا

أ.د. ضياء خليل

الهندسة الكهربائية ونائب عميد جامعة عين شمس، القاهرة، جمهورية مصر العربية.

أ.د. سلطان أبو عرابي

أمين عام رابطة الجامعات العربية

رئيس جامعة اليرموك (سابقاً)

الكيمياء العضوية، جامعة ميشيغان، الولايات المتحدة الأمريكية

أ.د. كلاوس ها يتنغر

أستاذ الرياضيات، جامعة وادي تاكاري، ريودي جانيرو

البرازيل.

أ.د. كمال منصور جمبي

كلية الحاسب الآلي ونظم المعلومات، جامعة الملك عبد العزيز، جدة، المملكة العربية السعودية.

أ.د. امين فاروق فهمي

أستاذ الكيمياء، جامعة عين شمس، القاهرة، جمهورية مصر العربية.

أ.د. عبد الغفور

الهندسة الميكانيكية، الجامعة الوطنية للعلوم والتكنولوجيا، باكستان

أ.د. محمود عبد العاطي

عميد البحث العلمي والدراسات العليا، جامعة العلوم التطبيقية، البحرين

نائب رئيس الأكاديمية الأفريقية للعلوم، كينيا

أستاذ الرياضيات التطبيقية – جمهورية مصر العربية.

قواعد النشر في المجلة (*)

- أن يكون البحث جديداً؛ لم يسبق نشره.
- أن يتسم بالأصالة والجدّة والابتكار والإضافة للمعرفة.
- أن لا يكون مستقلاً من بحوثٍ سبق نشرها للباحث/للباحثين.
- أن تراعى فيه قواعد البحث العلميّ الأصيل، ومنهجيتيه.
- أن يشتمل البحث على:
 - صفحة عنوان البحث باللغة الإنجليزية
 - مستخلص البحث باللغة الإنجليزية
 - صفحة عنون البحث باللغة العربية
 - مستخلص البحث باللغة العربية
 - مقدمة
 - صلب البحث
 - خاتمة تتضمن النتائج والتوصيات
 - ثبت المصادر والمراجع
 - الملاحق اللازمة (إن وجدت)
- في حال (نشر البحث ورقياً) يمنح الباحث نسخة مجانية واحدة من عدد المجلة الذي نشر بحثه، و (10) مستلّات من بحثه.
- في حال اعتماد نشر البحث تؤوّل حقوق نشره كافة للمجلة، ولها أن تعيد نشره ورقياً أو إلكترونياً، ويحقّ لها إدراجه في قواعد البيانات المحليّة والعالمية- بمقابل أو بدون مقابل- وذلك دون حاجة لإذن الباحث.
- لا يحق للباحث إعادة نشر بحثه المقبول للنشر في المجلة- في أي وعاء من أوعية النشر- إلا بعد إذن كتابي من رئيس هيئة تحرير المجلة.
- نمط التوثيق المعتمد في المجلة هو نمط (IEEE).

(*) يرجع في تفصيل هذه القواعد العامة إلى الموقع الإلكتروني للمجلة:

<https://journals.iu.edu.sa/JESC/index.html>

معلومات الإيداع

النسخة الورقية:

تم الإيداع في مكتبة الملك فهد الوطنية برقم 8742 / 1439 وتاريخ 17 / 09 / 1439 هـ
الرقم التسلسلي الدولي للدوريات (ردمد) -7936-1658

النسخة الإلكترونية:

تم الإيداع في مكتبة الملك فهد الوطنية برقم 8742 / 1439 وتاريخ 17 / 09 / 1439 هـ
الرقم التسلسلي الدولي للدوريات (ردمد) -7944-1658

الموقع الإلكتروني للمجلة

<https://journals.iu.edu.sa/JESC/index.html>

ترسل البحوث باسم رئيس تحرير المجلة إلى البريد الإلكتروني :
jesc@iu.edu.sa

(الآراء الواردة في البحوث المنشورة تعبر عن وجهة نظر الباحثين فقط، ولا تعبر بالضرورة عن رأي المجلة)

بِسْمِ اللَّهِ الرَّحْمَنِ الرَّحِيمِ



مجلة الجامعة الإسلامية

للعوم التطبيقية

مجلة علمية دورية محكمة

1441 هـ

السنة : الأولى

العدد : 2